AN ABSTRACT OF THE DISSERTATION OF

Dongjun Yuk for the degree of Doctor of Philosophy in Civil Engineering presented on November 1, 2004.

Title: Numerical Modeling of Full-Coupled Fluid-Structure Interaction

Abstract approved:

Redacted for Privacy Redacted for Privacy

A numerical model for the simulation of fully-coupled fluid-structure interaction is developed in this study. In modeling the fluid, the Reynolds Averaged Navier-Stokes equations are solved for an incompressible viscous fluid field and a k-ε model is employed for turbulence computations. Hydrodynamic forces obtained by the integration of the fluid pressure along the structural boundaries are applied as external excitation forces to the structural system and the dynamic response of the structural system is computed based on dynamic equilibrium. To determine the nonlinear dynamic

response of the structure in the flow field, iterative procedures are developed. The numerical model is verified and validated through comparisons with several different types of experiments.

The numerical model is then applied to examine the runup and rundown of the submarine landslide generated waves with various configurations. The functional relationships between the maximum runup/rundown and the geometric and material properties of landslides are obtained.

The numerical model is also applied to predict the experimental moored response of a structure subjected to periodic waves. The linear and nonlinear waves, as well as the structural response, are modeled accurately. The dynamic response of the moored structure, which is modeled with nonlinear restoring forces, shows the characteristic behaviors such as sub-harmonic/super-harmonic responses. General application procedures for the fluid-structure interaction model are presented. The subaerial and aerial drop of a rigid body and the influence of impact on the fluid body are examined.

Numerical Modeling of Full-Coupled Fluid-Structure Interaction

by

Dongjun Yuk

A DISSERTATION

submitted to

Oregon State University

in partial fulfillment of
the requirements for the
degree of

Doctor of Philosophy

Presented November 1, 2004
Commencement June 2005

Doctor of Philosophy dissertation of Dongjun Yuk presented on November 1, 2004.

APPROVED:

Redacted for Privacy

Co-Major Professor, representing Civil Engineering

Redacted for Privacy

Co-Major Professor, representing Civil Engineering

Redacted for Privacy

Head of the Department of Civil, Construction and Environmental Engineering

Redacted for Privacy

Dean of the Graduate School

I understand that my dissertation will become part of the permanent collection of Oregon State University libraries. My signature below authorizes release of my dissertation to any reader upon request.

Redacted for privacy

Dongjun Yuk, Author

ACKNOWLEDGEMENTS

I would like to expresses sincere appreciation to Dr. Solomon C. Yim for his continuous support and suggestions in performing researches. I also want to thank Dr. Philip L.F. Liu for providing me very useful information and insight in understanding wave mechanics. I would like to thank all the committee members: Dr. Robert L. Higdon, Dr. Jack F. Higginbotham, Dr. Michael H. Scott for their time and effort spent reviewing my Ph.D. thesis. Special appreciation goes to Dr. Lin for all his comments, suggestions and friendship.

I thank my parents, Changung Yuk and Youngja You, for their never-ending encouragement, support and belief in my pursuit of doctoral degree. I would like to thank my wife, Jayoung Seong, for her patience and love; and son, Kibeom Yuk, for the happiness that he brought in my family.

CONTRIBUTION OF AUTHORS

Drs. Solomon C. Yim and Philip L.F. Liu contributed to all chapters in this dissertation and were involved in the numerical modeling and interpretations of the results. Dr. Andrea Panizzo and Eng Marcello di Risio contributed to Chapter 5 in this dissertation by providing experimental data.

TABLE OF CONTENTS

Page

CHAPTER 1: General Introduction 1

Literature Review 2

Objective and Brief Summary 4

References 6

CHAPTER 2: Numerical Modeling of Submarine Mass-Movement Generated Waves Using RANS Model 9

Abstract 10

Introduction 10

Description of the Model 13

Numerical Results and Discussions 17

Concluding Remarks 30

Acknowledgements 31

References 31

CHAPTER 3: Analysis of Fluid-Structure Interaction Using RANS Equations, Part I: Model Development and Validation 35

TABLE OF CONTENTS (Continued)

Page

Abstract 36

Introduction 37

Numerical Model for Waves and Stationary Structures 38

Development of numerical model for Waves and Moving Structures 42

Development of Numerical Model for Dynamic Equilibrium 45

Special Treatment for Free Surface Piercing 49

Validation of Numerical Model 50

- Moving channel bottom and wave generation 50
- Submerged Sliding Block 54
- Aerial Landslide 59

Concluding Remarks 60

Acknowledgements 62

References 62

TABLE OF CONTENTS (Continued)

Page

CHAPTER 4: Analysis of Fluid-Structure Interaction Using RANS Equations, Part II: Application to Experimental Moored Structure 76

Abstract 77

Introduction 78

Description of Laboratory Tests 81

Development of Numerical Model 82

Development of Numerical Model based on Experimental Model 82
Modeling of Forces Associated with Structure and Fluid 83
Equation of Motion for the Structure System 84
Identification of Coefficients in EOM 85
Determination of Boundary Conditions and Grid Size 87

Iterative Procedure for Dynamic Equilibrium 88

Numerical Results and Discussions 90

Concluding Remarks 94

Acknowledgements 95

TABLE OF CONTENTS (Continued)

Page

References 95

CHAPTER 5: Numerical Modeling of Submerged and Aerial Drop of Rigid Body and Wave Generation 107

Abstract 108

Introduction 109

Model Description 110

Experimental Setup 114

Numerical Modeling 116

Concluding Remarks 120

Acknowledgements 121

References 121

CHAPTER 6: Concluding Remarks 136

Recommended Future Study 138

BIBLIOGRAPHY 140

APPENDICES 144

A. Numerical method for the RANS equations and structural dynamics 145

B. Numerical modeling of the box-drop and experimental data 158

LIST OF FIGURES

Figure Page

2.1 Free surface comparisons between simulation and experimental data at 0.5, 1.0, 1.5, 2.0, 2.5, and 3.0 s in wave generation region. First panel shows portion of triangular shape moving boundary 19

2.2 Free surface comparisons between simulation and experimental data at x = 4, 8, and 12 m in propagation region 20

2.3 Turbulence intensity around moving body at t = 0.5, 1.0, 1.5, 2.0, 2.5, and 3.0 seconds 22

2.4 Influence of sliding mass velocity on wave height: (a) Time series of free surface at x = 3.5 m, (b) Maximum wave height 22

2.5 Influence of mass movement velocity on runup and rundown: (a) Elevation of free surface level along solid fixed boundary, (b) Maximum and minimum free surface level 23

2.6 Free surface comparisons between simulation and experimental data at 0.5, 1.0, and 1.5 s in wave generation region. Solid rectangles shows upper right corner of triangular shape moving boundary 25

2.7 Computational domain and numerical experiment setup 26

2.8 Least square fit of rundown to numerical simulation data 29

2.9 Least square fit of runup to numerical simulation data 30

LIST OF FIGURES (Continued)

Figure Page

3.1 Fluid volume change within a computational cell due to the moving boundary 63

3.2 Partially blocked cell by solid boundary 63

3.3 Flow chart of iteration procedure for force and displacement computation 64

3.4 Theoretical bed deformation model 65

3.5 Time histories of exponential and half-sine bed movements 65

3.6 Comparisons of wave profiles between experimental data and numerical results using half-sine displacement time history for impulsive, transitional and creeping motions: (a) Exponential motion. (b) Transitional motion, (c) Creeping bed motion.
——— Numerical results. oooooooo Experimental data 66

3.7 Comparisons of wave profiles between experimental data and numerical results using exponential displacement time history for impulsive, transitional and creeping motions: (a) Exponential motion. (b) Transitional motion, (c) Creeping bed motion.
——— Numerical results. oooooooo Experimental data 67

3.8 Experimental setup for sliding block generated waves 68

3.9 Forces acting on sliding block and its component: (a) gravity force (b) wave force 68

LIST OF FIGURES (Continued)

Figure Page

3.10 Free surface comparisons between simulations and experimental data at 0.5, 1.0, 1.5, and 2.0 s in generation region 68

3.11 Free surface comparisons between simulations and experimental data at x=4, 8, and 12 m in propagation region 69

3.12 Displacement time history comparisons with experimental data and simulation results 70

3.13 VOF modification in free surface and moving-boundary interface cell 71

3.14 Free surface comparisons between simulation and experimental data at 0.6, 1.0, and 1.5 s in wave generation region. Solid rectangles shows upper right corner of triangular shape moving boundary 72

3.15. Snapshot of subaerial landslide at 0.5 sec with tangential force and normal force on moving boundaries 73

4.1 Profile view of the experimental model in a 2-D wave flume 97

4.2 Sphere of radius R with average disk of radius b 97

4.3 Schematic diagram of mass, spring and dash-pot system with external force 98

4.4 Restoring force from mooring lines 98

LIST OF FIGURES (Continued)

Figure Page

4.5 Flow chart of iteration procedure for dynamic equilibrium 99

4.6 Time series of free surface elevation and surge response of structure (Test D1) 99

4.7 Time series of free surface elevation and surge response of structure (Test D2) 100

4.8 Time series of free surface elevation and surge response of structure (Test D3) 100

4.9 Time series of free surface elevation and surge response of structure (Test D9) 101

4.10 Time series of free surface elevation and surge response of structure (Test D14) 101

4.11 Time series of free surface elevation, surge and heave responses of structure (Test E2) 102

4.12 Time series of free surface elevation, surge and heave responses of structure (Test E3) 102

4.13 Time series of free surface elevation, surge and heave responses of structure (Test E4) 103

4.14 Time series of free surface elevation, surge and heave responses of structure (Test E5) 103

LIST OF FIGURES (Continued)

Figure Page

4.15 Time series of free surface elevation, surge and heave responses of structure (Test E6) 104

4.16 Time series of free surface elevation, surge and heave responses of structure (Test E7) 104

4.17 Time series of free surface elevation, surge and heave responses of structure (Test E13) 105

4.18 Snapshot of velocity field, turbulence intensity and normal/shear force components on rigid body at t=18.4 sec (Test E3) 105

5.1 Locations of wave gauges and 2 dimensional flume 122

5.2 Definition of length, width, and height of rigid body 122

5.3 Snapshot of rigid body drop with free surface at t=+0.32 sec and displacement time history of moving rigid body (Test L10H10M3) 123

5.4 Time series of free surface elevation at x=0.4m and 0.85m (Test L10H10M3) 123

5.5 Contour plot of pressure field computed by numerical model at t=0.2, 0.4, 0.6, and 0.8 seconds (Test L10H10M3) 124

5.6 Vector plot of velocity field computed by numerical model at t=0.2, 0.4, 0.6, and 0.8 seconds (Test L10H10M3) 125

LIST OF FIGURES (Continued)

Figure Page

5.7 Turbulence intensity (m/s) computed by numerical model at t=0.2, 0.4, 0.6, and 0.8 seconds (Test L10H10M3) 126

5.8 Snapshot of rigid body drop with free surface at t=+0.32 sec and displacement time history of moving rigid body (Test L10H10P3) 127

5.9 Time series of free surface elevation at x=0.4m and 0.85m (Test L10H10P3) 127

5.10 Contour plot of pressure field computed by numerical model at t=0.2, 0.4, 0.6, and 0.8 seconds (Test L10H10P3) 128

5.11 Vector plot of velocity field computed by numerical model at t=0.2, 0.4, 0.6, and 0.8 seconds (Test L10H10P3) 129

5.12 Turbulence intensity (m/s) computed by numerical model at t=0.2, 0.4, 0.6, and 0.8 seconds (Test L10H10P3) 130

5.13 Snapshot of rigid body drop with free surface at t=+0.32 sec and displacement time history of moving rigid body (Test L10H18P3) 131

5.14 Time series of free surface elevation at x=0.4m and 0.85m (Test L10H18P3) 131

5.15 Contour plot of pressure field computed by numerical model at t=0.2, 0.4, 0.6, and 0.8 seconds (Test L10H18P3) 132

LIST OF FIGURES (Continued)

Figure Page

5.16 Vector plot of velocity field computed by numerical model at t=0.2, 0.4, 0.6, and 0.8 seconds (Test L10H18P3) 133

5.17 Turbulence intensity (m/s) computed by numerical model at t=0.2, 0.4, 0.6, and 0.8 seconds (Test L10H18P3) 134

5.18 Tangential and normal force on moving boundaries and pressure field at t=0.4 seconds (Test L10H18P3) 135

LIST OF TABLES

Table Page

2.1 Parameters used for runup and rundown simulations 28

3.1 Parameters of numerical model for various bed movements 53

4.1 Wave parameters used in experiments of SDOF system 91

4.2 Wave parameters used in experiments of MDOF system 91

4.3 Coefficients of EOM for SDOF and MDOF system 92

5.1 Experiments configurations 115

LIST OF APPENDICES

Appendix Page

A. Numerical method for the RANS equations and structural dynamics 145

B. Numerical modeling of the box-drop and experimental data 158

LIST OF APPENDIX FIGURES

Figure Page

A.1 Snapshots of rigid body drop and wave generation, Test L5H6M3 159

A.2 Snapshots of rigid body drop and wave generation, Test L10H6M3 160

A.3 Snapshots of rigid body drop and wave generation, Test L10H10M3 161

A.4 Snapshots of rigid body drop and wave generation, Test L10H18M3 162

A.5 Snapshots of rigid body drop and wave generation, Test L10H23M3 164

A.6 Snapshots of rigid body drop and wave generation, Test L15H6M3 166

A.7 Snapshots of rigid body drop and wave generation, Test L5H6PM0 167

A.8 Snapshots of rigid body drop and wave generation, Test L5H10PM0 169

A.9 Snapshots of rigid body drop and wave generation, Test L5H18PM0 171

A.10 Snapshots of rigid body drop and wave generation, Test L10H6PM0 173

LIST OF APPENDIX FIGURES (Continued)

Figure Page

A.11 Snapshots of rigid body drop and wave generation, Test L10H10PM0 174

A.12 Snapshots of rigid body drop and wave generation, Test L10H18PM0 176

A.13 Snapshots of rigid body drop and wave generation, Test L10H23PM0 178

A.14 Snapshots of rigid body drop and wave generation, Test L15H6PM0 180

A.15 Snapshots of rigid body drop and wave generation, Test L5H10P3..... 181

A.16 Snapshots of rigid body drop and wave generation, Test L10H6P3..... 183

A.17 Snapshots of rigid body drop and wave generation, Test L10H10P3 185

A.18 Snapshots of rigid body drop and wave generation, Test L10H18P3 187

A.19 Snapshots of rigid body drop and wave generation, Test L10H23P3 189

A.20 Snapshots of rigid body drop and wave generation, Test L15H6P3..... 191

CHAPTER 1

General Introduction

Interactions of structure with fluid have been a phenomenon of great interest to engineers and scientists due to the wide range of practical applications, including ocean and coastal engineering, biomechanics, aerodynamics, hydrodynamics, oceanography, etc. A great deal of theoretical and experimental research effort has been made by structure engineers, ocean engineers and hydro-dynamicists to investigate the wave forces on coastal and offshore structures. As a result, several methodologies for estimating wave forces on fixed structures have been developed and validated through laboratory tests (Hammack, 1973; Sarpkaya, 1986; Obasaju, 1988; Justesen, 1991; Heinrich, 1991). Depending on the point of view or the problem of interest, the influence of fixed body on fluid flow and vice verse can be considered as fluid-structure interaction. In this study, however, fluid-structure interaction refers to the fully coupled interaction between a moving body (or

bodies) in the fluid. Thus, in general, the physical phenomenon becomes more complex due to the strong coupling between the moving body and the fluid compared to the fluid interacting with a fixed body.

Literature Review

Several numerical models have been developed to describe the waves generated by submerged or aerial mass movements. With the common assumption that the geometry and the time history of the mass movement can be prescribed, these models adopt various additional approximations in hydrodynamics. For instance, Lynett & Liu (2002) presented a model based on the depth-integrated nonlinear wave equations, which include the frequency dispersion effects. Therefore, their model can simulate relatively short waves that might be generated by a submarine mass movement. Grilli & Watts (1999) adopted a Boundary Integral Equation Method (BIEM), based on the potential flow theory, and developed a fully nonlinear free-surface flow model for mass

movement-generated waves. The approach, however, does not take into account wave breaking, which could be important in the vicinity of the generation region as well as the runup region. The depth-integrated model suffers the same drawback as the BIEM model in terms of the inability to model breaking waves without further approximation. The depth-integrated model is much more computationally efficient than the BIEM because it reduces the 3D problem to a 2D problem in the horizontal space. Heinrich (1991) modified the NASA-VOF2D model, which is a 2D (vertical plane) nonlinear free surface model based on the Navier-Stokes equations, to study the generation, propagation and runup of tsunamis created by landslides. Breaking waves were modeled by the volume of fluid method proposed by Hirt and Nichols (1981). The effects of turbulence are not considered. Heinrich compared his numerical results for both submarine and aerial mass movements with his own experiments. The agreement is reasonable, except in the regions where wave-breaking induced turbulence is important.

In 1991, Kothe *et al.* developed a numerical model known as

"RIPPLE" for transient, two-dimensional, incompressible fluid flows with surface tension on free surfaces of general topology. In RIPPLE, the modeling of wave generation and turbulence was not incorporated. The RIPPLE code was modified to model the waves and fixed rigid structure interaction by Lin (1998) at Cornell University and the modified code was named COrnell BReAking wave and Structure (COBRAS), which includes the turbulence effects and has the capability of modeling breaking waves, interactions between waves and fixed coastal structures. In this study, modifications of COBRAS are made and additional algorithms are developed to predict and analyze the dynamic responses of structures interacting with exciting waves.

Objective and Brief Summary

The general objective of the study presented herein is to obtain a better understanding of the strong influence of rigid structure motion on fluid body for the preservation of human lives and coastal infrastructures, and for the

deployment and operation of special structural and mechanical systems in coastal areas. The specific objective of this study is to develop a numerical model for fluid-structure interaction and validate the accuracy and capability of the model in predicting structural dynamics behavior and associated flow fields.

A brief summary of this thesis is presented in this section. In Chapter 2, the strong influence of rigid structure motion on a fluid body is examined through landslide generated waves and associated runup/rundown. Relationships between maximum runup and maximum rundown as functions of the specific density, the initial submergence level, the angle of the moving mass as well as the slope angle are identified by using the numerical model developed in this study. The development of a model with iterative procedures based on dynamic equilibrium and validation through comparisons with experimental data is presented in Chapter 3. In Chapter 4, the numerical model for fluid-structure interaction is applied to analyze the motions of a moored structure. General application procedures of the fluid-structure interaction model for the moored structure analysis will be presented. Comparisons

between simulations and laboratory test results will be made to validate the capability and accuracy in prediction of the moored sphere responses under hydrodynamic excitation forces. Limitations and capabilities of the numerical model observed in the modeling of experimental moored structure response will be also discussed. In Chapter 5, the numerical model is utilized to analyze the impact of a rigid body dropping on an initially still fluid. The influence of subaerial and aerial drop on the flow field of the generation and propagation regions is examined. A summary of the results, concluding remarks and recommended future studies are provided in Chapter 6.

References

Enet, F., Grilli, S.T. and Watts, P. 2003. Laboratory experiments for tsunamis generated underwater landslides: Comparison with numerical modeling. *Proc. Thirteenth Int. Offshore and Polar Engr.* Conf., 372-379.

Grilli, S.T. and Watts, P. 1999 Modeling of waves generated by a moving submerged body. Applications to underwater landslides. *Eng. Anal. Boundary Elements*, 23, 645-656.

Hammack, J.L. 1973. A note on tsunamis: their generation and propagation in an ocean of uniform depth. *J. Fluid Mech.*, 60, 769-799.

Heinrich, P. 1991. Nonlinear numerical model of landslide-generated water waves. *Int.J. Engr. Fluid Mech.*, 4(4), 403-416.

Heinrich, P. 1992. Nonlinear water waves generated by submarine and aerial landslides. *J. Waterway, Port, Coastal and Ocean Engr.*, ASCE, 118, 249-266.

Hirt, C.W. and Nichols, B.D. 1981. Volume of fluid (VOF) method for the dynamics of free boundaries. *J. Comp. Phys.*, 39, 201-225.

Justesen, P. 1991. A numerical study of oscillating flow around a circular cylinder. *J.Fluid Mech., 222*, 157-196.

Kothe, D.B., Mjolsness, R.C. and Torrey, M.D. 1991. Ripple: A computer program for incompressible flows with free surfaces. Rep. LA-12007-MS. Los Alamos National Laboratory.

Lin, P. 1998. Numerical modeling of breaking waves. Ph.D. Thesis. Cornell University.

Lin, P. and Liu, P.L.-F. 1998a A numerical study of breaking waves in the surf zone. *J. Fluid Mech.*, 359, 239-264.

Lynett, P.J. and Liu, P.L.-F. 2002 A numerical study of submerged landslide generated waves and runup. *Proc. Royal Soc.*, A. 458, 2885-2910.

Mei, C.C. 1989. The applied dynamics of ocean surface waves. World Scientific.

Obasaju, E.D., Bearman, P.W. and Graham, J.M.R., 1988. A study of force, circulation and vortex patterns around a circular cylinder in oscillating flow. *J. Fluid Mech.*, 196, 467-494.

Sarpkaya, T. 1986. Force on a cylinder in viscous oscillatory flow at low Keulegan-Carpenter numbers. *J. Fluid Mech.*, 165, 61-71.

Watts, P. and Grilli, S.T. 2003. Underwater landslide shape, motion, deformation and tsunami generation. *Proc. Thirteenth Int. Offshore and Polar Engr. Conf.*, 364-371.

CHAPTER 2

Numerical Modeling of Submarine Mass-Movement Generated Waves Using RANS Model

Yuk, D., Yim, S.C. and Liu, P. L.-F.

Computers and Geosciences, Elsevier

Abstract

In this paper a numerical model for predicting waves generated by nearshore submarine mass-movements is described. The model is based on the Reynolds Averaged Navier-Stokes (RANS) equations with the $k-\varepsilon$ turbulence model. The volume of fluid (VOF) method is employed to track the free surface. Numerical results obtained from the present model are validated with laboratory experiments and analytical solutions. Very good agreements are observed for both submarine and aerial mass movements. Numerical experiments are performed to obtain the empirical formula for the maximum runup and rundown as functions of slide properties.

Keyword: Submarine mass movement, numerical model, turbulence, breaking waves

Introduction

Motivated by the needs for preservation of human lives and coastal infrastructure, and for the deployment and operation of special structural and mechanical systems in coastal areas, the study of nearshore wave motions and

wave-structure interaction has been of interest to coastal scientists and engineers for many years.

Coastal wave generation due to submarine mass movement is a complex process. While the length-scale of a submarine mass movement is usually smaller than that of a seafloor displacement created by a fault rupture, the time-scale is usually longer. Therefore, the concept of "initial free surface displacement" in the wave generation region becomes a critical issue. Hence the evolution of the free surface displacement in the source region of mass movement needs to be modeled entirely. Furthermore, the characteristics of a submarine mass movement, including the soil properties, volume and area of the mass movement, also require a post-event bathymetry survey.

Several numerical models have been developed to describe the waves generated by submerged or aerial mass movements. With the common assumption that the geometry and the time history of the mass movement can be prescribed, these models adopt various additional approximations in hydrodynamics. For instance, Lynett & Liu (2002) presented a model based on the depth-integrated nonlinear wave equations, which include the frequency dispersion effects. Therefore, their model can simulate relatively short waves that might be generated by a submarine mass movement. Grilli & Watts (1999) adopted a Boundary Integral Equation Method (BIEM), based on the potential flow theory, and developed a fully nonlinear model for mass movement-

generated waves. However, the approach does not take into account wave breaking, which could be important in the vicinity of the generation region as well as the runup region. The depth-averaged model suffers the same drawback as the BIEM model in terms of the inability to model breaking waves. However, it is much more computationally efficient for it has reduced the 3D problem to a 2D problem in the horizontal space. Heinrich (1992) modified the NASA-VOF2D model, which is a 2D (vertical plane) nonlinear free surface model based on the Navier-Stokes equations, to study the generation, propagation and runup of tsunamis created by landslides. The effects of turbulence are not considered. Heinrich compared his numerical results for both submarine and aerial mass movements with his own experiments. The agreement is reasonable, except in the regions where wave-breaking induced turbulence is important.

In recent years, significant advancement in modeling wave-breaking processes and interactions between breaking waves and coastal structures has been made. For example, COBRAS (Cornell Breaking waves and Structures model) is based on the Reynolds Averaged Navier-Stokes (RANS) equations with a $k-\varepsilon$ turbulence closure model. While a nonlinear Reynolds stress model is employed to allow anisotropic turbulence, the Volume of Fluid (VOF) method is used to track the free surface movements. COBRAS has been verified and validated by comparing numerical results with experimental data

for runup and rundown of breaking waves on a uniform beach (Lin & Liu 1998 a, b, Lin *et al.* 1999). It also has the ability to simulate wave-structure interactions, where the structures are rigid, stationary, fully submerged or surface piercing (Hsu *et al.* 2002).

The primary goal of the research surmarized in this chapter is to modify COBRAS to allow time-dependent moving solid boundaries such that mass movement-created waves can be simulated. Since COBRAS is capable of calculating turbulence, the modified model will be able to simulate breaking waves, runup and rundown. Here, we shall first present briefly the theoretical background of COBRAS and discuss the necessary modification to simulate the mass movement. 2D numerical results are then compared with experimental data. Some discussions on the future extensions are given at the end of the paper.

Description of the Model

In this section the mathematical formulation and the associated numerical algorithm of COBRAS are discussed briefly. More detailed discussions can be found in Lin and Liu (1998 a, b). The model is based on the Reynolds Averaged Navier-Stokes (RANS) equations. For a turbulent flow, the velocity field and pressure field can be decomposed into two parts: the mean

(ensemble average) velocity and pressure $< u_i >$ and $< p >$, and the deviatoric (or turbulent) velocity and pressure u_i' and p'. Thus, $u_i =< u_i > + u_i'$ and $p =< p > + p'$ in which $i = 1,2,3$ for a three-dimensional flow. If the fluid is assumed incompressible, the mean flow field is governed by the Reynolds Averaged Navier-Stokes equations:

$$\frac{\partial \langle u_i \rangle}{\partial x_i} = 0 \tag{1}$$

$$\frac{\partial \langle u_i \rangle}{\partial t} + \langle u_j \rangle \frac{\partial \langle u_i \rangle}{\partial x_j} = -\frac{1}{\rho}\frac{\partial \langle p \rangle}{\partial x_i} + g_i + \frac{1}{\rho}\frac{\partial \langle \tau_{ij} \rangle}{\partial x_j} - \frac{\partial \langle u_i' u_j' \rangle}{\partial x_j} \tag{2}$$

in which ρ is the density of the fluid, g_i the i-th component of the gravitational acceleration, and the mean molecular stress tensor $< \tau_{ij} >= 2\mu < \sigma_{ij} >$ with μ being the molecular viscosity and $< \sigma_{ij} >$, the rate of strain tensor of the mean flow. In the momentum equation (2), the influence of the turbulent fluctuations on the mean flow field is represented by the Reynolds stress tensor, $-\rho < u_i' u_j' >$. Many second-order turbulence closure models have been developed for different applications. In the present model, the Reynolds stress is approximated by a nonlinear algebraic stress model:

$$\rho\langle u_i'u_j'\rangle = \frac{2}{3}\rho k\delta_{ij} - C_d\frac{k^2}{\varepsilon}\left(\frac{\partial\langle u_i\rangle}{\partial x_j}+\frac{\partial\langle u_j\rangle}{\partial x_i}\right) - \rho\frac{k^3}{\varepsilon^2}\left[\begin{array}{l} C_1\left(\frac{\partial\langle u_i\rangle}{\partial x_l}\frac{\partial\langle u_l\rangle}{\partial x_j}+\frac{\partial\langle u_j\rangle}{\partial x_l}\frac{\partial\langle u_l\rangle}{\partial x_i}-\frac{2}{3}\frac{\partial\langle u_l\rangle}{\partial x_k}\frac{\partial\langle u_k\rangle}{\partial x_l}\delta_{ij}\right) \\ +C_2\left(\frac{\partial\langle u_i\rangle}{\partial x_k}\frac{\partial\langle u_j\rangle}{\partial x_k}-\frac{1}{3}\frac{\partial\langle u_l\rangle}{\partial x_k}\frac{\partial\langle u_l\rangle}{\partial x_k}\delta_{ij}\right) \\ +C_3\left(\frac{\partial\langle u_k\rangle}{\partial x_i}\frac{\partial\langle u_k\rangle}{\partial x_j}-\frac{1}{3}\frac{\partial\langle u_l\rangle}{\partial x_k}\frac{\partial\langle u_l\rangle}{\partial x_k}\delta_{ij}\right) \end{array}\right] \quad (3)$$

in which C_d, C_1, C_2 and C_3 are empirical coefficients, δ_{ij} is the Kronecker delta, $k = <u_i'u_i'>/2$ is the turbulent kinetic energy, and $\varepsilon = \nu <(\partial u_i'/\partial x_j)^2>$ is the dissipation rate of turbulent kinetic energy, where $\nu = \mu/\rho$ is the molecular kinematic viscosity. It is noted that for the conventional eddy viscosity model $C_1 = C_2 = C_3 = 0$ in equation (3) and the eddy viscosity is then expressed as $\nu_t = C_d k^2/\varepsilon$. Compared with the conventional eddy viscosity model, the nonlinear Reynolds stress model (3) can be applied to general anisotropic turbulent flows.

The governing equations for k and ε are modeled as (Lin and Liu, 1998 a, b),

$$\frac{\partial k}{\partial t}+\langle u_j\rangle\frac{\partial k}{\partial x_j} = \frac{\partial}{\partial x_j}\left[\left(\frac{\nu_t}{\sigma_k}+\nu\right)\frac{\partial k}{\partial x_j}\right]-\langle u_i'u_j'\rangle\frac{\partial\langle u_i\rangle}{\partial x_j}-\varepsilon \quad (4)$$

$$\frac{\partial \varepsilon}{\partial t}+\langle u_j\rangle\frac{\partial \varepsilon}{\partial x_j}=\frac{\partial}{\partial x_j}\left[\left(\frac{\nu_t}{\sigma_\varepsilon}+\nu\right)\frac{\partial \varepsilon}{\partial x_j}\right] + C_{1\varepsilon}\frac{\varepsilon}{k}\nu_t\left(\frac{\partial\langle u_i\rangle}{\partial x_j}+\frac{\partial\langle u_j\rangle}{\partial x}\right)\frac{\partial\langle u_i\rangle}{\partial x_j}-C_{2\varepsilon}\frac{\varepsilon^2}{k} \tag{5}$$

in which $\sigma_k, \sigma_\varepsilon, C_{1\varepsilon}$ and $C_{2\varepsilon}$ are empirical coefficients. The coefficients in equation (3) to (5) have been determined by performing many simple experiments and enforcing the physical realizability; the recommended values for these coefficients can be found in Lin and Liu (1998 a, b).

Appropriate boundary conditions need to be specified. For the mean flow field, both the no-slip and the free-slip boundary condition can be imposed on the solid boundary. Along the mass surface, the velocity of the moving boundary is either prescribed or determined by dynamic equilibrium of the mass. The zero-stress condition is required on the mean free surface by neglecting the effect of airflow. For the turbulent field, near the solid boundary, the log-law distribution of mean tangential velocity in the turbulent boundary layer is applied so the values of k and ε can be expressed as functions of distance from the boundary and the mean tangential velocity outside of the viscous sub-layer. On the free surface, the zero-gradient boundary conditions are imposed for both k and ε, *i.e.*, $\partial k/\partial n = \partial \varepsilon/\partial n = 0$. A low level of k for the initial and inflow boundary conditions is assumed.

In the numerical model, the RANS equations are solved by a finite difference two-step projection method. The forward time difference method is used to discretize the time derivative. The advection terms are discretized by the combination of the central difference and upwind methods. The central difference method is employed to discretize the pressure gradient terms as well as stress gradient terms. The VOF method is used to track the free surface. The transport equations for k and ε are solved with the similar method used in solving the momentum equations (Lin and Liu 1998 a, b).

Numerical Results and Discussions

To validate the numerical model, numerical simulations of several laboratory experiments have been carried out for waves generated by vertical bottom movements (Hammack, 1973) and by a sliding triangular block on a uniform beach (Heinrich, 1992). In Hammack's experiments waves do not break in the generation region and the present numerical results agree with Hammack's data very well. In this paper we shall focus our discussion on Heinrich's experiments in which the generated waves break.

The computational domain is 12 m in the x-direction and 2 m in the y-direction. A variable grid size system is used in the x-direction with minimum grid size of 0.01 m and a fixed grid size of 0.01 m is employed in the y-

direction. To satisfy all stability conditions and restrictions of the incorporated methods, a fixed time step of 5×10^{-4} s is used. Numerical results in generation (*i.e.*, near moving mass) and propagation regions are compared with experimental data as shown in Figure 1 and 2. The submarine mass movement is modeled by a triangular shaped moving boundary that is initially located at 0.01m below the free surface as in Heinrich (1992). The measured displacement time history from the Heinrich experiment is used as prescribed motion of the triangular mass. Since the grid size is not small enough to resolve the boundary layer, the free-slip boundary condition is applied on all the solid boundaries including sliding body, slopes, and channel bottom. As shown in Figures 1 and 2, wave profiles in the generation region and the propagation region are in good agreement with experimental data. Some deviations are observed, however, in the wave profile at t = 1.5 s when the reflected wave starts to break. It is surmised that the disagreement in wave profile is caused by the random nature of turbulence near wave breaking where the "exact" measured value is difficult to determine.

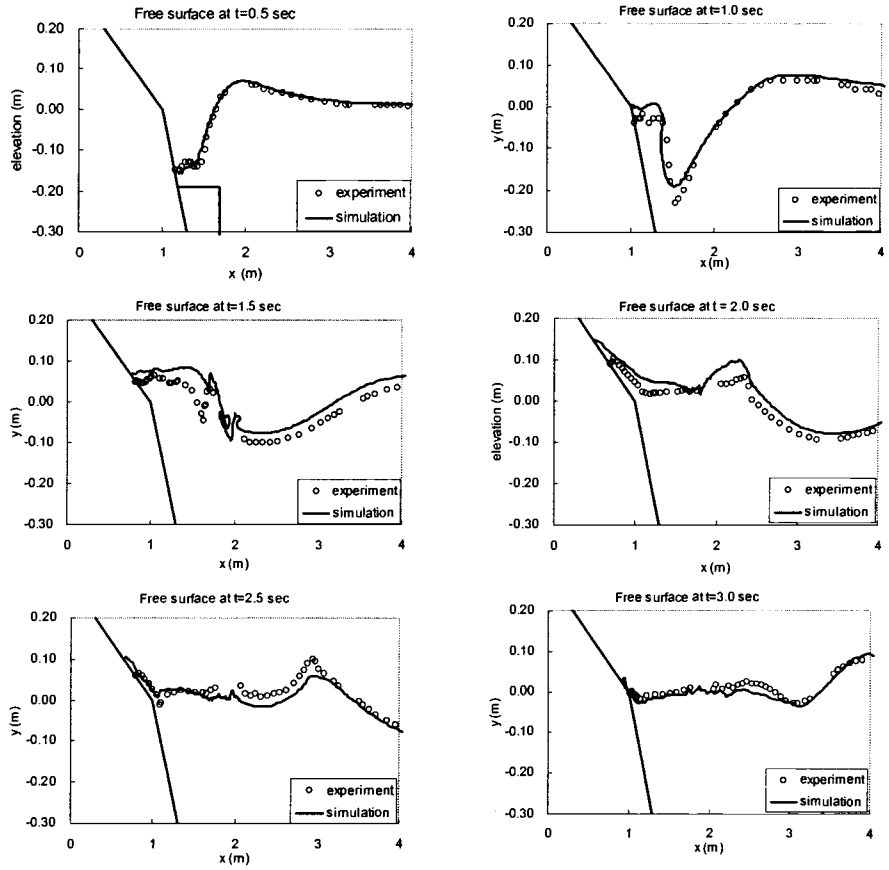

Fig 1. Free surface comparisons between simulation and experimental data at 0.5, 1.0, 1.5, 2.0, 2.5, and 3.0 s in wave generation region. First panel shows portion of triangular shape moving boundary.

A convergence test using minimum grid sizes of 0.005, 0.01, 0.02, and 0.04m has been performed. A fine grid of 30 cells is used to resolve maximum wave height. It is observed that convergence is achieved with a grid size 0.01m. This value (or smaller) is employed throughout the study.

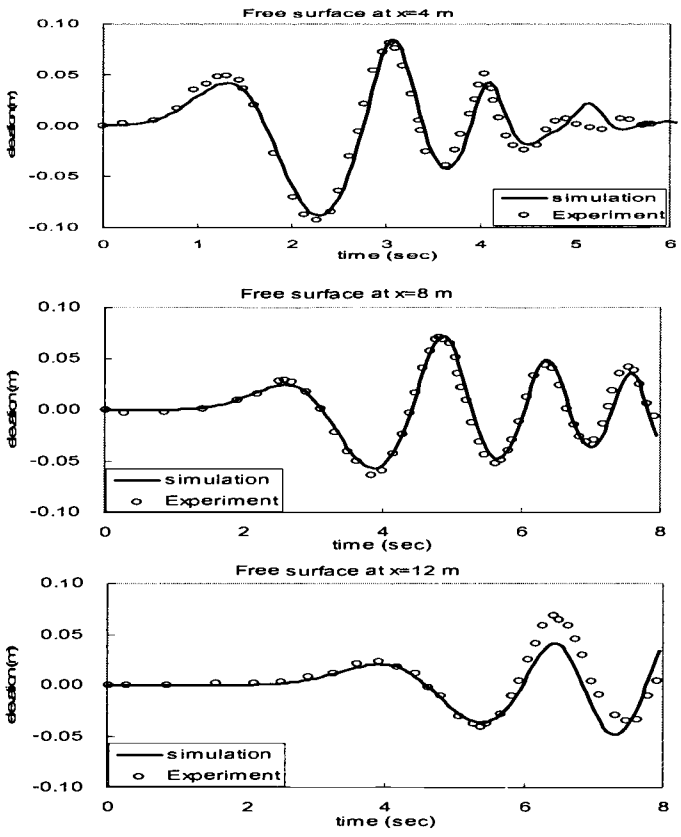

Fig 2. Free surface comparisons between simulation and experimental data at x = 4, 8, and 12 m in propagation region.

Turbulence generation by the submarine mass movement on a beach and its evolution are examined. Figure 3 shows the contours of turbulence intensity at t = 0.5, 1.0, 1.5, 2.0, 2.5, and 3.0 seconds. It is observed that when the mass is in motion turbulence is generated around the upper right corner because of flow separation. Once the waves generated by the moving mass reach shore, waves are reflected. After the mass movement stops, turbulence is

generated by the breaking of the reflected wave near the free surface and turbulence intensity decreases gradually. The maximum turbulence intensity can reach 0.83 m/sec, which is almost 50% of the mean velocity.

The influence of the submarine mass movement velocity is examined by varying the displacement time history. Denoting a0 as the initial acceleration of the mass movement measured in the experiment, we have calculated three additional cases with accelerations that are 0.5a0, 0.75a0 and 1.25a0, respectively. In these simulations the total displacement and the volume of mass movement remain constant so that only one parameter, *i.e.*, velocity of the moving mass, is varied. The effects of mass movement velocity on maximum wave heights, runup and rundown are shown in Figures 4 and 5, respectively. As expected, the magnitudes of the wave height, runup and rundown increase with increasing acceleration.

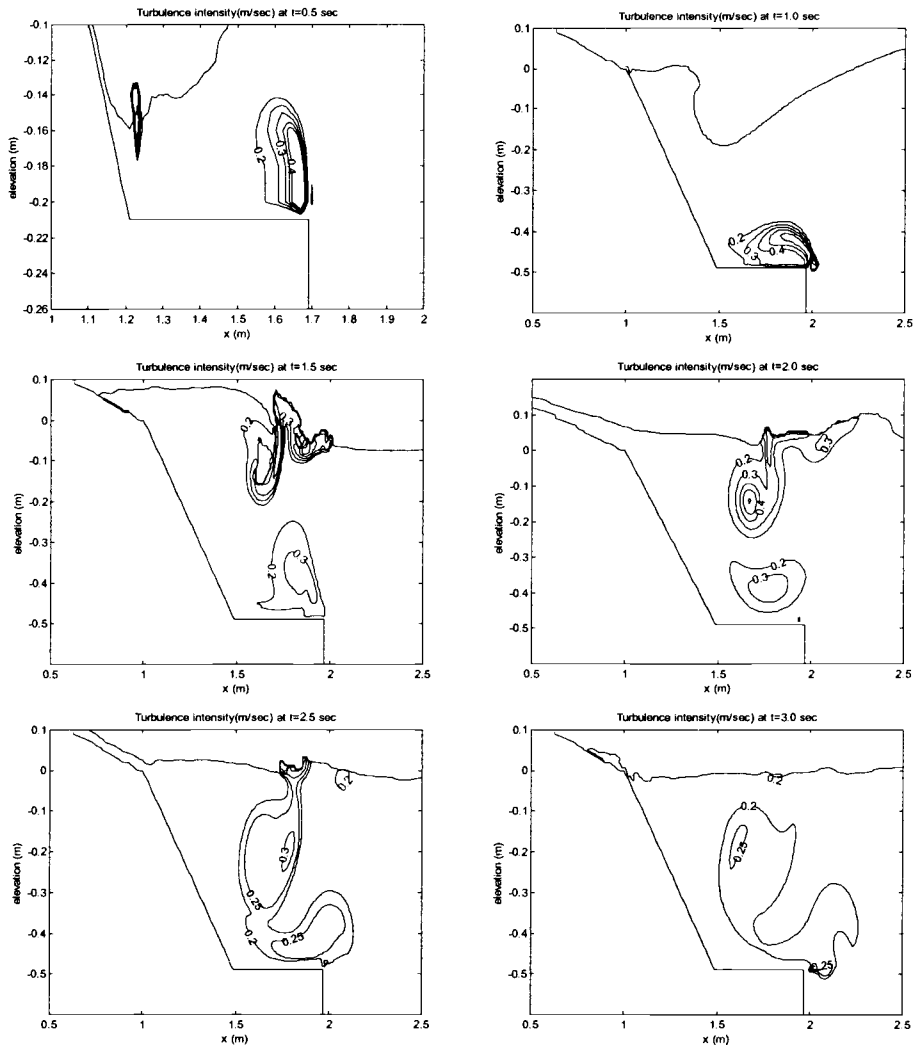

Fig 3. Turbulence intensity around moving body at t = 0.5, 1.0, 1.5, 2.0, 2.5, and 3.0 seconds.

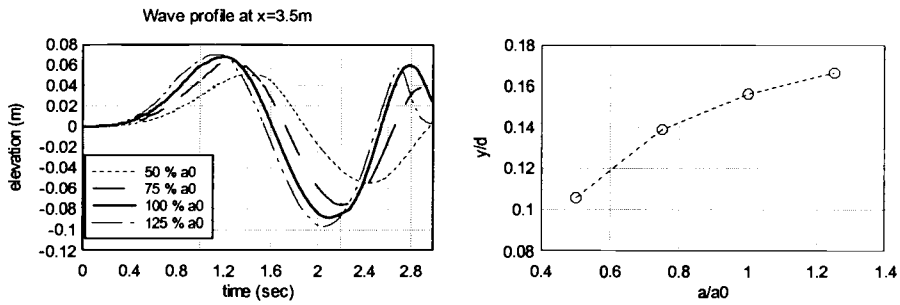

Fig 4. Influence of sliding mass velocity on wave height: (a) Time series of free surface at x = 3.5 m, (b) Maximum wave height.

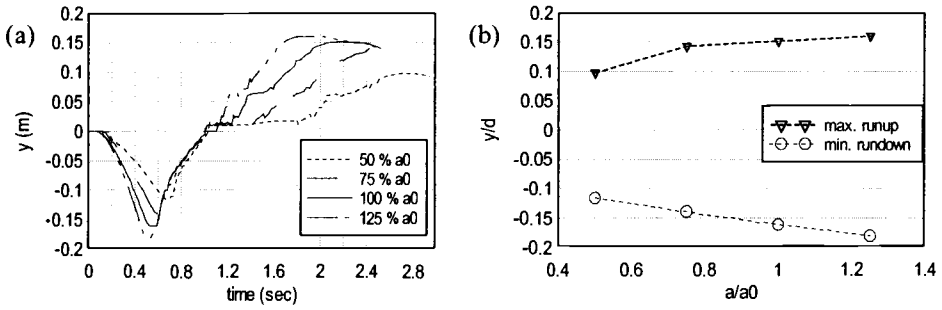

Fig 5. Influence of mass movement velocity on runup and rundown: (a) Elevation of free surface level along solid fixed boundary, (b) Maximum and minimum free surface level.

Another case examined is an aerial slide in which a part of the moving body is initially located above the free surface and slides down along a uniform slope. Therefore, the moving solid boundary intersects the free surface until the moving body is completely submerged. During this period of time, a special treatment in the VOF function is required to satisfy the law of mass conservation. This is necessary because the pressure in the free surface cell is not calculated from the Poisson pressure equation, and is specified by the free surface boundary condition. Thus, a source/sink term cannot be used in the free surface and the moving boundary interface cell to generate an equal amount of fluid corresponding to the volume change due to the moving boundary. An algorithm to treat the free surface and moving-boundary interface cell is developed and incorporated in the code.

Numerical simulations are performed and compared with the experimental data obtained by Heinrich (1992) to validate the predictive

capability of the numerical model for an aerial sliding. The problem setup is exactly the same as that for the submarine slide except that the moving body is located initially just above the free surface. Wave profiles in the generation region at t = 0.6, 1.0, and 1.5 sec are compared with experimental data as shown in Figure 6. From the wave profile at t = 0.6 sec, we observe that the wave starts to break and becomes highly random. The discrepancy of wave profiles at t = 1.5 sec might be attributed to turbulence.

The numerical model developed in this study is utilized to investigate the functional relationship between both the runup and rundown of submarine slide generated waves and the geometric parameters of the sliding body and slope. From the previous work by Chen (2002), the following form of the functional relation is employed.

$$\frac{\eta_{rd}}{b} = c0\gamma^{c1}\left(\frac{A_l}{A_w}\right)^{c2}(\sin\theta)^{c3}(\sin\beta)^{c4} \qquad (6)$$

$$\frac{\eta_{up}}{b} = d0\gamma^{d1}\left(\frac{A_l}{A_w}\right)^{d2}(\sin\theta)^{d3}(\sin\beta)^{d4} \qquad (7)$$

In the above equation, *c0, c1, c2, c3, c4, d0, d1, d2, d3,* and *d4* are constants to be determined, η_{rd} is the maximum rundown, η_{up} is the maximum runup, b is the base length of triangular sliding body, θ is the slope angle, γ is the specific weight of sliding body, β is the angle of top face of sliding body, A_l is the area of sliding body, and A_w is the area of fluid above the sliding body.

A series of numerical experiments is conducted to examine the functional relations.

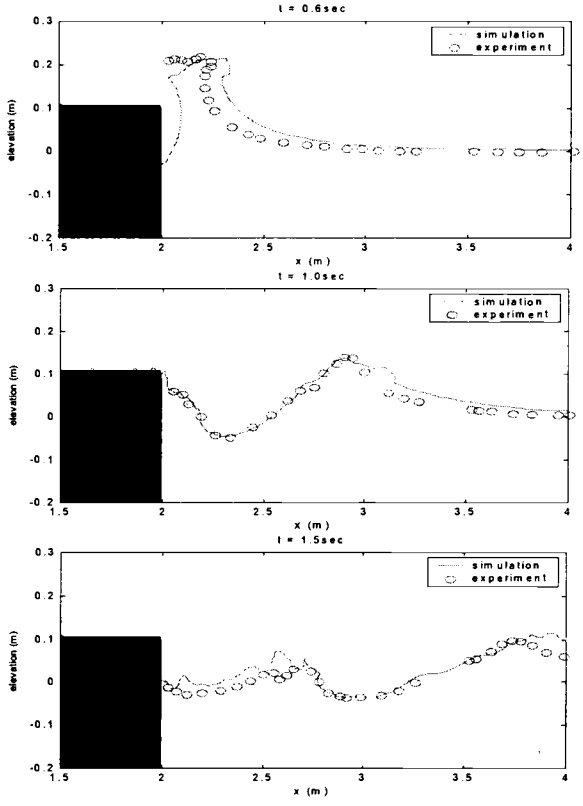

Fig 6. Free surface comparisons between simulation and experimental data at 0.5, 1.0, and 1.5 s in wave generation region. Solid rectangles shows upper right corner of triangular shape moving boundary.

In previous studies (Chen 2002, Grilli and Watts 1999) of functional relations between submarine slide and runup/rundown, the motion of a sliding body is determined by solving the differential equation obtained by balancing inertial, added mass, gravitational, buoyancy, and fluid dynamic drag forces. In

this study, the sliding body movement is not predetermined but obtained by considering the instantaneous dynamic equilibrium of the moving body including the coupled fluid-structure interaction. An iterative procedure is introduced to compute the sliding body movement.

For the numerical experiments for runup and rundown, the computational domain is discretized by 410 x 280 grids points in horizontal and vertical direction, respectively, and variable time step is used to advance solutions in time so that stability conditions are satisfied. The slope where landslides occur and runup/rundown is measured is located on the left end of computational domain. In addition to specifying the domain boundary at the right edge as "open", a sponge layer of sufficient width is placed on the right side to prevent reflections of waves at the domain boundary and ensure full energy absorption (see Figure 7).

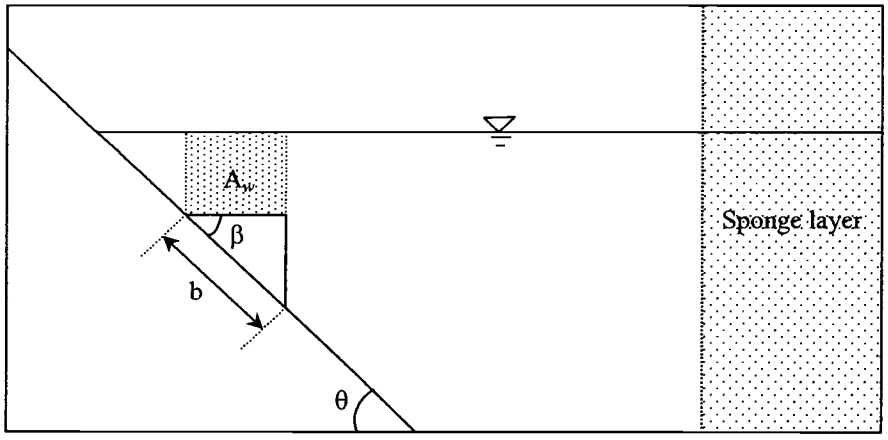

Fig 7. Computational domain and numerical experiment setup

Four sets of numerical experiments are conducted. In each set, only one parameter is varied with all others being fixed so that the effects of varying the particular parameter can be examined. The parameter space used in this study is shown in Table 1. The range of parameter variation is determined by considering the possibility of physical realization. For example, the specific density of landslides can be less than 1.0, but physically it may not be realizable because of the buoyant force.

To measure the runup and rundown, numerical wave gauges are placed along the slope. However, maximum and minimum vertical elevations of the free surface on the slope are recorded as runup and rundown, respectively. The distance that waves move along the slope can also be calculated using the maximum and minimum values in the vertical direction and the slope angle.

Figures 8 and 9 show the effects of parameters considered in this study on rundown/runup and the results of regression analysis. The power curves used to fit the data ensure that runup and rundown do not occur when any of parameters are zero. In determining the final formula for runup and rundown, the power curves are used again and the exponents from the curve fit are multiplied to obtain the coefficients for the final runup and rundown formula.

Test	$sin\theta$	γ	β	A_l	A_w	A_l/A_w	$sin\beta$
1	0.707	1.4	1.0	0.250	0.240	1.0399	0.707
2	0.707	1.8	1.0	0.250	0.240	1.0399	0.707
3	0.707	2.0	1.0	0.250	0.240	1.0399	0.707
4	0.707	2.4	1.0	0.250	0.240	1.0399	0.707
5	0.707	2.8	1.0	0.250	0.240	1.0399	0.707
6	0.707	2.12	0.707	0.125	0.071	1.768	0.707
7	0.707	2.12	0.707	0.125	0.115	1.083	0.707
8	0.707	2.12	0.707	0.125	0.145	0.865	0.707
9	0.707	2.12	0.707	0.125	0.180	0.695	0.707
10	0.707	2.12	0.707	0.125	0.212	0.589	0.707
11	0.707	2.12	0.707	0.125	0.248	0.505	0.707
12	0.707	2.0	1.0	0.25	0.311	2.24	0.985
13	0.707	2.0	1.0	0.25	0.311	2.24	0.966
14	0.707	2.0	1.0	0.25	0.311	2.24	0.940
15	0.707	2.0	1.0	0.25	0.311	2.24	0.866
16	0.707	2.0	1.0	0.25	0.24	1.040	0.707
17	0.643	2.0	1.0	0.25	0.24	1.040	0.707
18	0.574	2.0	1.0	0.25	0.24	1.040	0.707
19	0.500	2.0	1.0	0.25	0.24	1.040	0.707
20	0.423	2.0	1.0	0.25	0.24	1.040	0.707
21	0.342	2.0	1.0	0.25	0.24	1.040	0.707

Table 1.Parameters used for runup and rundown simulations.

Based on the numerical results shown in Figures 8 and 9, the functional relationships between runup/rundown and the parameters are found to be

$$\frac{\eta_{rd}}{b} = 0.4178\gamma^{0.1454}\left(\frac{A_l}{A_w}\right)^{0.2803}(\sin\beta)^{1.4395}(\sin\theta)^{0.5086} \tag{8}$$

$$\frac{\eta_{up}}{b} = 1.0593\gamma^{0.2078}\left(\frac{A_l}{A_w}\right)^{0.1889}(\sin\beta)^{3.6134}(\sin\theta)^{1.6566} \tag{9}$$

Note that larger runup and rundown are observed as expected for increasing mass density, face angle, slope angle, and decreasing initial submergence of the landslide.

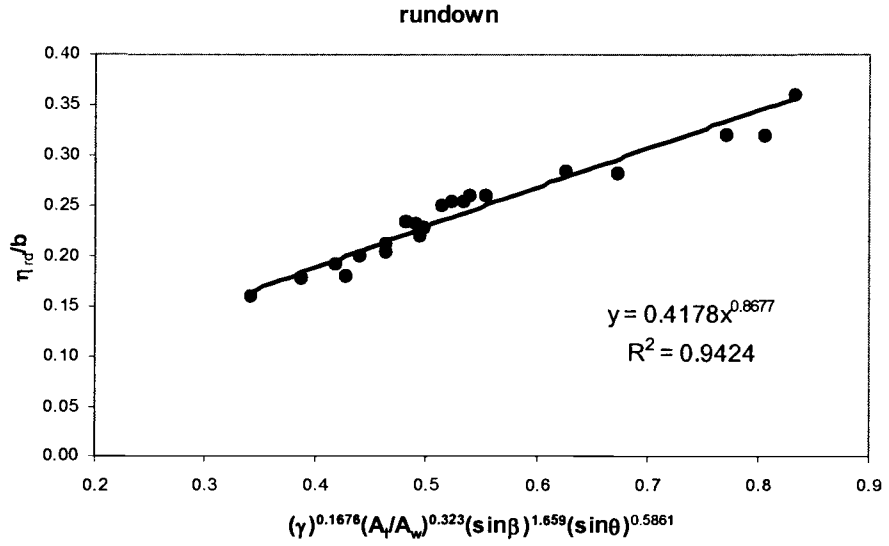

Fig 8. Least square fit of rundown to numerical simulation data.

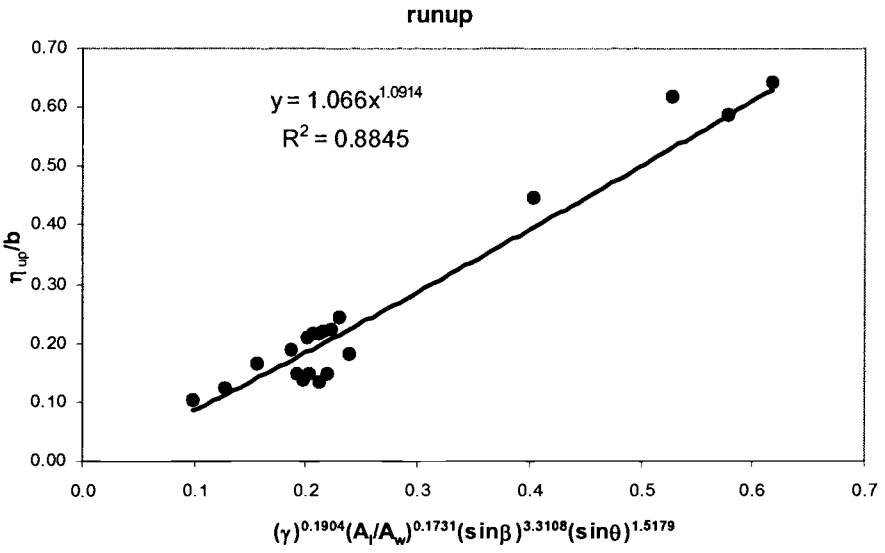

Fig 9. Least square fit of runup to numerical simulation data.

Concluding Remarks

The capability and accuracy of the present numerical model in predicting wave generation by submarine and aerial mass movements and propagation has been validated. In addition, the influence of a moving body velocity on runup and rundown has been examined. For the higher sliding body velocity, maximum runup and rundown are increased as expected.

Turbulence generation by triangular shape moving body occurs around its upper right corner due to flow separation and near the free surface where waves break. Careful experiments measuring the velocity field are desirable to validate the prediction of the turbulence intensity.

Relationships between maximum runup and maximum rundown as functions of the specify density, the initial submergence level, the angle of the moving mass as well as the slope angle are identified. The runup and rundown formulae show good agreement with physical intuitions.

Finally we should remark that the present results are limited to two-dimensional slides, which are uniform along the shoreline. In reality slides are three dimensional. The predicted maximum runup based on the present two-dimensional slides might not be conservative. In the case of a three-dimensional slide, additional lateral (in the alongshore direction) as well as on-offshore waves can be generated due to the free surface drawdown and rebound above the moving slide. This feature requires further study.

Acknowledgements

Partial support from the National Science Foundation Grants CMS-9908392 and CMS-0217744, and the US Office of Naval Research Grants N00014-92-1221 and N00014-04-10008 are gratefully acknowledged.

References

Chen, Y.-Y. 2002 "Numerical modeling of 2D waves generated by submarine landslides", MS thesis, Cornell University.

Grilli, S.T. and Watts, P. 1999 "Modeling of waves generated by a moving submerged body. Applications to underwater landslides". *Eng. Anal. Boundary. Elements*, **23**, 645-656.

Hammack, J.L. 1973. "A note on tsunamis: their generation and propagation in an ocean of uniform depth", *J. Fluid Mech.*, **60**, 769-799.

Heinrich, P. 1992. "Nonlinear water waves generated by submarine and aerial landslides", *J. Waterway, Port, Coastal and Ocean Engrg., ASCE*, **118**, 249-266.

Hsu, T.-J., Sakakiyama, T. and Liu, P.L.-F. 2002 "Validation of a model for wave-structure interactions". *Coastal Engrg,* **46**, 25-50.

Lin, P. and Liu, P.L.-F. 1998a "A numerical study of breaking waves in the surf zone". *J. Fluid Mech.*, **359**, 239-264.

Lin, P. and Liu, P.L.-F. 1998b "Turbulence transport, vorticity dynamics, and solute mixing under plunging breaking waves in surf zone." *J. Geophys. Res.*, **103**, 15677-15694.

Lin, P., Chang, K.-A., and Liu, P.L.-F. 1999 "Runup and rundown of solitary waves on sloping beaches". *J. Waterway, Port, Coastal and Ocean Engrg.*, ASCE, **125** (5), 247-255.

Lynett, P.J. and Liu, P.L.-F. 2002 "A numerical study of submerged landslide generated waves and runup", *Proc. Royal Soc.*, A. **458**, 2885-2910.

Nomenclature

A_l area of sliding body

A_w area of fluid above sliding body

b base length of triangular body

C_1, C_2, C_3, C_d, σ_k, σ_τ, $C_{1\tau}$, $C_{2\tau}$ empirical coefficients

g_i i-th component of gravitational acceleration, m/s^2

k turbulence kinetic energy

p hydrodynamic pressure

u_i i-th component of velocity vector

$\langle\rangle$ ensemble average

β angle of top face of sliding body

Δx, Δy grid size in x and y direction

δ_{ij} Kronecker delta

ε turbulence kinetic energy dissipation rate

η_{rd} maximum rundown

η_{up} maximum runup

μ dynamic viscosity, kg m^{-1} s^{-1}

ν_t eddy viscosity

θ slope angle

ρ density of fluid, kg/m^3

σ strain rate tensor

τ_{ij}^{m} molecular viscous stress tensor

ζ_0 maximum displacement of moving channel bottom

CHAPTER 3

Analysis of Fluid-Structure Interaction Using RANS Equations, Part I: Model Development and Validation

Yuk, D., Yim, S.C. and Liu, P. L.-F.

Abstract

The numerical model (Lin, 1998) for wave hydrodynamics based on Reynolds Averaged Navier-Stokes (RANS) equations with a k-ε turbulence closure model and Volume of Fluid (VOF) method is modified to simulate the interactions between moving rigid body and surrounding fluid. The finite-difference method with a combination of forward and backward difference scheme is employed for the numerical approximations of the velocity of fluid fields with respect to time and space. The volumetric change in a control volume due to rigid-body movement is taken into consideration by modifying the continuity equation. Depending on the movement direction and the orientation of rigid body boundaries, a source/sink term is added in the Poisson Pressure equation that appears in the second step of the two-step projection method employed. Hydrodynamic excitation forces on the structure are determined by integrating the stress (or pressure) components acting normal to the rigid-body surface and the response of the rigid body is computed based on equilibrium of the dynamic forces. An iterative procedure is introduced to satisfy the equilibrium between structural dynamics and hydrodynamic forces at the fluid-structure interface. The equation of motion for structural dynamics is solved using the predictor-corrector method. The numerical model is

validated through comparisons with existing experimental data and analytical solutions from Hammack (1973) and Heinrich (1992).

Introduction

Interactions between fluid and structure have been a phenomenon of great interest to many engineers and scientists due to the wide range of practical applications in aero and hydrodynamics. A great deal of research effort has been made by ocean engineers and hydro-dynamicists to investigate the wave forces on coastal and offshore structures, both theoretically and experimentally. As a result, wave forces on fixed structures have been developed and validated thoroughly through numerous laboratory tests. Depending on the point of view or the problem of interest, the influence of fixed body on fluid and fluid on fixed body can be considered a fluid-structure interaction. In this study, however, fluid-structure interaction refers to the interaction between a moving body (or bodies) and the fluid. Thus, in general, the physical phenomenon becomes more complex due to the strong coupling between the moving body and the fluid compared to the fluid interacting with a fixed body.

In 1991, a numerical model called RIPPLE was developed for transient, two-dimensional, incompressible fluid flows with surface tension on free

surfaces of general (Kothe and *et al,* 1991). In RIPPLE, modeling of wave generation and turbulence was not incorporated, and these components are investigated in the current study. Lin (1998) modified RIPPLE to model the waves and fixed structure including turbulence and named it COrnell BReAking wave and Structure (COBRAS) model. COBRAS has the ability to model breaking waves and interactions between waves and fixed coastal structures. In this Chapter, the modification of COBRAS and the development of an algorithm for the dynamic response of structures to waves and their influence on the fluid are described. To verify and validate the developed model, comparisons are made using numerical results and various experimental data.

Numerical Model for Waves and Stationary Structures

For an incompressible Newtonian fluid, the dynamics of the fluid can be described by the well-known Reynolds Averaged Navier-Stokes (RANS) equations which consist of the continuity equation (1) and the momentum equation (2).

$$\frac{\partial \langle u_i \rangle}{\partial x_i} = 0 \tag{1}$$

$$\frac{\partial\langle u_i\rangle}{\partial t}+\langle u_j\rangle\frac{\partial\langle u_i\rangle}{\partial x_j}=-\frac{1}{\langle\rho\rangle}\frac{\partial\langle p\rangle}{\partial x_i}+g_i+\frac{1}{\langle\rho\rangle}\frac{\partial\langle\tau_{ij}^m\rangle}{\partial x_j}-\frac{\partial\langle u_i'u_j'\rangle}{\partial x_j}+\frac{1}{\langle\rho\rangle^2}\left\langle\rho'\frac{\partial p'}{\partial x_i}\right\rangle-\frac{1}{\langle\rho\rangle^2}\left\langle\rho'\frac{\partial\tau_{ij}^{m'}}{\partial x_j}\right\rangle \quad (2)$$

where subscripts i, j denote the Cartesian component taking 1, 2, 3 for three dimensional flows and $\langle\ \rangle$ the ensemble average of different solutions of the Navier-Stokes equations (NSE). However, the numerical model developed for this study is 2D only. Thus the range of subscripts i, j is limited to 1 and 2. In equations (1) and (2), u_i denotes the i-th component of the velocity vector, ρ the density of fluid, p the pressure, g_i the i-th component of the gravitational acceleration, and τ_{ij}^m the molecular viscous stress tensor. Under the Newtonian fluid assumption, τ_{ij}^m can be expressed by $\tau_{ij}^m = 2\mu\sigma_{ij}$ with μ being the dynamic viscosity (whose unit is kg m^{-1} s^{-1}) and $\sigma_{ij} = \frac{1}{2}\left(\frac{\partial u_i}{\partial x_j}+\frac{\partial u_j}{\partial x_i}\right)$ the strain rate tensor.

In the fifth term of the right hand side of equation (2), there is a correlation between density fluctuations and the gradient of pressure fluctuations. The correlation between density fluctuations and the gradient of viscous stress fluctuations are also included in the sixth term of right hand side of equation (2). Since these correlations are not clearly known up to today and the constant density within the fluid is assumed, the last two terms in equation (2) are neglected in this study. The only additional term when compared to

general NSE is the fourth term of the right hand side of equation (2), i.e., $\frac{\partial\langle u_i u_j\rangle}{\partial x_j}$. The ensemble average of the product of two different velocity fluctuation components in that term is used for the definition of Reynolds stress tensor. The Reynolds stress tensor is defined as

$$R_{ij} = -\langle\rho\rangle\langle u_i' u_j'\rangle \tag{3}$$

In the previous research, many second-order turbulence closure models have been developed for different applications. In this study, the so-called k-ε model, where the Reynolds stress is approximated by a nonlinear algebraic stress model, is employed as the turbulence closure model (Shih *et al.*, 1996).

$$\begin{aligned}\langle\rho\rangle\langle u_i' u_j'\rangle = {} & \frac{2}{3}\rho k\delta_{ij} - C_d\frac{k^2}{\varepsilon}\left(\frac{\partial\langle u_i\rangle}{\partial x_j}+\frac{\partial\langle u_j\rangle}{\partial x_i}\right) \\ & -\rho\frac{k^3}{\varepsilon^2}\left[\begin{array}{l} C_1\left(\frac{\partial\langle u_i\rangle}{\partial x_l}\frac{\partial\langle u_l\rangle}{\partial x_j}+\frac{\partial\langle u_j\rangle}{\partial x_l}\frac{\partial\langle u_l\rangle}{\partial x_i}-\frac{2}{3}\frac{\partial\langle u_l\rangle}{\partial x_k}\frac{\partial\langle u_k\rangle}{\partial x_l}\delta_{ij}\right) \\ +C_2\left(\frac{\partial\langle u_i\rangle}{\partial x_k}\frac{\partial\langle u_j\rangle}{\partial x_k}-\frac{1}{3}\frac{\partial\langle u_l\rangle}{\partial x_k}\frac{\partial\langle u_l\rangle}{\partial x_k}\delta_{ij}\right) \\ +C_3\left(\frac{\partial\langle u_k\rangle}{\partial x_i}\frac{\partial\langle u_k\rangle}{\partial x_j}-\frac{1}{3}\frac{\partial\langle u_l\rangle}{\partial x_k}\frac{\partial\langle u_l\rangle}{\partial x_k}\delta_{ij}\right)\end{array}\right]\end{aligned} \tag{4}$$

where C_1, C_2 and C_3 are empirical coefficients, δ_{ij} is the Kronecker delta, $k = \frac{1}{2}\langle u_i' u_i'\rangle$ is the turbulence kinetic energy and $\varepsilon = \nu\left\langle\left(\partial u_i'/\partial x_k\right)^2\right\rangle$ is the dissipation rate of turbulence kinetic energy with $\nu = \mu/\rho$ the kinematic

viscosity. When compared with the classical linear isotropic eddy viscosity closure model, equation (4) returns to the classical model with C_1=C_2=C_3=0 as shown below.

$$\langle u_i' u_j' \rangle = -2\nu_t \langle \sigma_{ij} \rangle + \frac{2}{3} k \delta_{ij} \tag{5}$$

where $\nu_t = C_d \frac{k^2}{\varepsilon}$ is the eddy viscosity and C_d is another empirical coefficient. The weakness of the linear isotropic eddy viscosity model is that equation (5) may not represent accurately the physics of anisotropic turbulence in complex turbulent flows. The turbulence closure model given in equation (4), however, can be applied to general anisotropic turbulent flows. The governing equation for k and ε (Rodi, 1980) are modeled as

$$\frac{\partial k}{\partial t} + \langle u_j \rangle \frac{\partial k}{\partial x_j} = \frac{\partial}{\partial x_j}\left[\left(\frac{\nu_t}{\sigma_k} + \nu\right)\frac{\partial k}{\partial x_j}\right] - \langle u_i' u_j' \rangle \frac{\partial \langle u_i \rangle}{\partial x_j} - \varepsilon \tag{6}$$

$$\begin{aligned} \frac{\partial \varepsilon}{\partial t} + \langle u_j \rangle \frac{\partial \varepsilon}{\partial x_j} &= \frac{\partial}{\partial x_j}\left[\left(\frac{\nu_t}{\sigma_\varepsilon} + \nu\right)\frac{\partial \varepsilon}{\partial x_j}\right] \\ &\quad + C_{1\varepsilon}\frac{\varepsilon}{k}\nu_t\left(\frac{\partial \langle u_i \rangle}{\partial x_j} + \frac{\partial \langle u_j \rangle}{\partial x}\right)\frac{\partial \langle u_i \rangle}{\partial x_j} - C_{2\varepsilon}\frac{\varepsilon^2}{k} \end{aligned} \tag{7}$$

where $\sigma_k, \sigma_\tau, C_{1\varepsilon}$ and $C_{2\varepsilon}$ are empirical coefficients. The coefficients in equations (4), (6) and (7) have been determined by performing many simple experiments and enforcing the physical realizability; the values for these

coefficients suggested by Lin and Liu (1998) and used in this study are C_1=0.0054, C_2=-0.0171, C_3=0.0027, C_1=1.44, $C_{2\varepsilon}$=1.9, σ_ε=1.3 and σ_k=1.0.

Applying the appropriate boundary conditions, and approximating the derivatives in Navier-Stokes equations using a finite-difference scheme with a combination of backward and forward difference methods, a numerical solution of the Navier-Stokes equations is obtained. Detailed descriptions of the assumptions for the turbulence closure model and the boundary conditions imposed on the computational domain boundaries and internal rigid-body boundaries can be found in a previous study by Lin (1998).

Development of numerical model for Waves and Moving Structures

The continuity equation in the RANS equations is valid for the incompressible fluid with fixed solid boundary. In the presence of a moving boundary, the conventional continuity equation needs to be modified to take the fluid volume change in a cell into consideration. In Figure 1, the initial location of the solid boundary at time t is denoted by AB. At the next time step, $t+\Delta t$, the location of the moving solid boundary is moved to $A'B'$ and the volume change of the solid boundary is denoted by dV_{obs}. For an incompressible fluid, the fluid volume change within a computational cell

during Δt should be the same as that of the moving solid boundary. The volume change in a cell can be expressed as

$$\iint_{S_{cell}} \vec{u} \bullet \vec{n} ds = \iint_{S_{obs}} \vec{v}_{obs} \bullet \vec{n} ds \tag{8}$$

where $\vec{u}$ and $\vec{v}_{obs}$ denote the velocity vectors of the fluid and the moving boundary, respectively. The vector $\vec{n}$ is defined as the unit outward normal to cell boundaries. The double integral with the intervals S_{cell}, S_{obs} represents the surface integration over the whole computational cell and over the surface occupied by moving solid boundary, respectively. The right hand side of equation (8) can be considered as the rate of the volume change of the moving boundary over dt. Thus the fluid volume change in a cell can be expressed as

$$\iint_{S_{cell}} \vec{u} \bullet \vec{n} ds = \frac{dV_{obs}}{dt} \tag{9}$$

and the modified continuity equation for the volume V can be expressed as

$$\frac{\partial \langle u_i \rangle}{\partial x_i} = \frac{1}{V} \frac{dV_{obs}}{dt} \tag{10}$$

The location of the solid boundary is identified by using a partial flow flag. For the more detailed identification of the solid boundary location, additional variables are used. To identify the openness of the cell faces, the variables $ar_{i,j}$ and $at_{i,j}$ are defined as the fractional area open to flow on the right and the top face of the cell (i,j). The fractional volume open to flow at the center of cell (i,j) is denoted by $ac(i,j)$.

Figure 2 shows a typical cell blocked partially by the solid boundary. The shaded area represents the area blocked by the solid boundary and is denoted by $(A_{obs})_{i,j}$. The partial cell variables are computed by

$$ar_{i,j} = \frac{d_j}{\Delta y_j},\quad at_{i,j} = \frac{d_i}{\Delta x_i},\quad ac_{i,j} = 1 - \frac{(A_{obs})_{i,j}}{\Delta x_i \Delta y_j} \tag{11}$$

Then dV_{obs} at the (n+1)-th time level can be calculated by

$$dV_{obs} = (A_{obs})_{i,j}^{n+1} - (A_{obs})_{i,j}^{n} = -\left(ac_{i,j}^{n+1} - ac_{i,j}^{n}\right)\Delta x_i \Delta y_j \tag{12}$$

Since the conservation of mass condition is used to derive the Poisson pressure equation (PPE) in the second step of the two step projection method, PPE needs to be modified accordingly. Imposing the modified continuity condition given by equation (10) yields

$$\frac{\partial}{\partial x_i}\left(\frac{1}{\rho^n}\frac{\partial p^{n+1}}{\partial x_i}\right) = \frac{1}{\Delta t}\frac{\partial \tilde{u}_i^{n+1}}{\partial x_i} - \frac{\left(ac_{i,j}^{n+1} - ac_{i,j}^{n}\right)}{\Delta t^2} \tag{13}$$

The last term in equation (13) functions as a source or sink numerically depending on dV_{obs}. The boundary condition for the Poisson pressure equation imposed on the moving rigid boundary is a Neumann boundary condition.

Theoretically, the velocity of the moving rigid boundary should be the same as the velocity of the fluid on the moving boundary. Due to the finite difference scheme and the partial cell technique employed in this model, however, the moving rigid boundary is not always exactly aligned with the grids. This makes it impossible to specify the velocity boundary condition

precisely on the moving boundary. In addition, when the moving boundary is somewhere between the cell faces, the velocity at the cell face is unknown. Thus, it is impossible to interpolate the velocity at the cell face from the velocity of the moving boundary. Therefore a sink/source term is used to implement moving boundaries instead of specifying velocity boundary conditions.

The pressure and velocity fields are determined from the numerical solution of Navier-Stokes equations. Then the hydrodynamic forces along the surface of moving rigid body are decomposed into the normal and tangential components based on the orientation of rigid boundaries in each computational cell. In the hydrodynamic force computations, it is noticed in Lin (1998) that the grid size is not small enough to resolve boundary layer on solid boundaries and "free-slip" boundary conditions are recommended. Thus it is assumed that tangential velocities around moving rigid body do not change and the shear stress due to the change of tangential velocities on the rigid boundaries is negligible. More detailed discussions about the shear stress will be presented in concluding remarks.

Development of Numerical Model for Dynamic Equilibrium

The displacement of fully or partially submerged rigid body is determined by solving the equation of motion. To describe the motion of the rigid body, local reference system with the origin fixed at the center of rigid body is used. The equation of motion for the rigid body can be expressed as

$$m\ddot{X} + c\dot{X} + k(X) = f_{ext} \tag{14}$$

where, m, c, $k(X)$, f_{ext} and X denote mass, damping coefficient, restoring force, external excitation and local reference system with the origin on the center of gravity of rigid body at initial location, respectively. Depending on the problems of interests and assumptions, damping, restoring and excitation forces should be derived appropriately. Derivation of the case-dependent governing equation for structural dynamics will be discussed later in this Chapter.

One of the key issues in modeling fluid-structure interaction is the interdependency between fluid and structural displacements. In other words, the fluid surrounding the moving rigid body accelerate or decelerate the rigid body and the rigid body response also influence the fluid nearby. This interactive influence is modeled by an iterative procedure developed in this study. The basic idea is that dynamic equilibria for both the structure side and the fluid side have to be always satisfied simultaneously. Let t_n and t_{n+1} denote two consecutive time steps. The information about fluid and structure, i.e., displacement, acceleration, velocity of rigid body and pressure, velocity field

of fluid, at the current time level t_n is known from the previous computation cycle. As the rigid body moves during the differential time period *dt*, the external excitation, which is the integration of pressure along the rigid body surface, will change and the location of rigid boundary, which is determined by the response of the rigid body to external excitation, will also change. At the next time step t_{n+1}, however, dynamic equilibria should be satisfied for both the fluid and the structure. The iterative procedure to satisfy the hydrodynamics and structural dynamics begins with an estimated external excitation force f_{n+1}^1. The subscript $n+1$ and superscript *1* in f_{n+1}^1 represent the time step and the number of iteration, respectively. The excitation at the current time step f_n is used as the first estimate of the excitation at the next time f_{n+1}.

The first estimated structural displacement is calculated and denoted by x_{n+1}^1. Then the location of rigid boundary in the computational domain is reset and the governing equation for fluid is solved. Once the pressure and the velocity field of fluid are computed, the excitation force is computed again with respect to the updated location of the rigid boundary and is denoted f_{n+1}^2. This excitation force f_{n+1}^2 is then used to determine the displacement of structure x_{n+1}^2. By repeating this iteration procedure until f_{n+1}^{k-1} converges to f_{n+1}^k or the difference between f_{n+1}^{k-1} and f_{n+1}^k becomes smaller than a predetermined

tolerance, the response of structure and the pressure and velocity field of fluid at the next time step t_{n+1} are computed. A flow chart of the iterative procedure is shown in Figure 3.

Integration of the second order linear ordinary differential equations (ODE) for structural dynamics is done by the Euler method. The order of accuracy of the Euler method employed in this model is known to be $O(\Delta t)$. There exist other numerical methods with higher order of accuracy for the integration of ODE, e.g., the Runge-Kutta 4^{th} order method. However, the higher order method requires the exact excitation force at the next time step. When the excitation force can be calculated or determined exactly at any time level, other existing higher order method can be employed in the numerical model to improve the accuracy in predicting the structure responses. As described earlier, since the excitation force at the next time level is unknown and estimated at the current time level, the effect of implementation of higher order method like Runge-Kutta 4^{th} order method on improving the accuracy of structural response prediction is expected to be negligible.

Alternatively, when structural dynamic equilibrium can be expressed in the form of linear ordinary differential equations, other numerical methods can be used for the time integration of equations of motions. For example, the dynamic equilibrium of sliding block on a slope can be expressed by second order linear ordinary differential equation. In this case, other methods, such as

the Newmark integration method, can be employed. It is assumed in the Newmark integration method that variation of acceleration during an incremental time Δt is linear.

Special Treatment for Free Surface Piercing

An algorithm is developed and incorporated in the numerical code to model free surface piercing motion of rigid boundary where a part of the moving rigid body interacts with the free surface. A special treatment in the VOF function is required to conserve the total volume of fluid in the computational domain. This is necessary because the pressure in the free surface cell is not calculated from the Poisson pressure equation, and is specified by the free surface boundary condition. Thus, in a cell where the free surface and moving boundary coexist, a source/sink term cannot be used to generate the same amount of fluid as the volume change due to the moving boundary.

In the entire free surface cell including the cell with moving-boundary, advection of VOF function are computed using standard procedures, which can be found in previous studies (Lin 1998). The volume of fluid, which is pushed by the boundary movement, is added in the adjacent cell as described in figure 13. When there are not enough space to add the volume change due to the rigid

boundary motions in the cell (i, j), the fluid volume left after filling the cell is distributed in the next neighboring cell $(i+1, j)$.

Validation of Numerical Model

Several different fluid structure interaction problems are simulated and compared with laboratory test results to validate the accuracy and capability of the numerical model developed in this study.

Moving Channel Bottom and Wave Generation

A series of laboratory tests had been performed on wave generation due to channel bottom movement and its propagation by Hammack (1973). Experiments were conducted in a flume with movable flat bottom. A part of the bottom was raised or dropped with different characteristic displacement time histories. Complete descriptions of the experimental setup and additional theoretical works can be found in Hammack (1973). In this study, only the wave profiles measured in the generation region is compared with simulation results. The experiment model setup is shown in Figure 4.

The time histories used for the displacement of channel bottom are referred to as the exponential and the half-sine bed movements, with both bed

movements asymptotically approach to a maximum displacement ζ_0. These displacements are given by

$$\zeta_e(x,t) = \zeta_0\left(1 - e^{\alpha t}\right)H\left(b^2 - x^2\right) \tag{15}$$

$$\zeta_s(x,t) = \zeta_0\left[\frac{1}{2}\left(1 - \cos\frac{\pi t}{T}\right)H(T-t) + H(t-T)\right]H\left(b^2 - x^2\right) \tag{16}$$

where H is the Heaviside step function. One of the parameters that characterize the bed movements is the characteristic time t_c. As shown in Figure 5, the characteristic time for the exponential bed movement is chosen such that $t=t_c$ when $\zeta/\zeta_0=2/3$ and for the half-sine bed movement the total time of movement T is defined as t_c.

These two different bed movements are subdivided into three categories depending on the time-size ratio. It is defined as $t_c\sqrt{gh}/b$ and used to characterize the bed movement in more details. When $t_c\sqrt{gh}/b << 1$, the bed movement is referred to as impulsive motion and when $t_c\sqrt{gh}/b >> 1$, it is called creeping motion. For the time-size ratio $t_c\sqrt{gh}/b$ of order 1, it is called transitional motion.

A series of experiments was conducted in a wave tank 103.8 ft long, 2 ft deep and 15.5 in wide. Since the moving channel bottom is symmetric about x=0, the origin of the theoretical model was represented in the experiment by the vertical wall at the upstream end of the wave tank. Thus only half of the

deformation and fluid domain was modeled experimentally. The free surface elevation was measured at the center line of the bed deformation $x/h = 0$ (i.e., the upstream end wall in the wave tank) and at the downstream edge of the bed deformation $x/h = b/h$.

The time history of the free-surface elevation of waves generated by both positive and negative bed motions were measured in the experiment. However, the experiments with positive bed motion are examined in this study. Moreover, the other parts of this model which are responsible for wave propagation and free surface tracking are already validated in previous research (Lin, 1998). Thus, the experimental results in the generation region obtained from the positive channel bottom motions are used here to validate the numerical model with the moving boundary.

In the numerical simulation, the computational domain of 4.5 m long in x-direction and 0.12 m deep y direction is discretized by variable grid size with minimum grid sizes Δx =0.5 cm and Δy =0.05 cm. Considering the maximum amplitude of wave generated by the bottom movement in the experiment is in the range of 1~1.5 cm, 20~25 grids which are estimated to be fine enough to resolve the measured wave height accurately are used in the numerical modeling. The detailed parameters of the numerical model are given in Table 1.

Table 1 Parameters of numerical model for various bed movements

		b(cm)	h(cm)	ζ_0(cm)	t_c(sec)	α
Half-sine bed motions	Impulse	61	10	1.0	0.080	•
	Transition	61	50	0.5	0.248	•
	Creeping	30.5	50	5.0	4.326	•
Exponential bed motions	Impulse	61	5	1.0	0.060	18.271
	Transition	61	5	0.5	0.340	3.232
	Creeping	61	5	1.5	7.581	0.145

In the numerical modeling, the time history of the bed movement is given by equations (15) and (16). Thus the iterative procedure for the interaction between the moving bottom and the fluid is not employed in this particular case. Numerical experiments are performed just for the verification and validation purpose. The nondimensional wave profiles measured at two different locations within the generation region are compared and shown in Figures 6 and 7.

As shown in these figures, the numerical results are in good agreements with the experimental data for both the half-sine and the exponential bed movements. However, some discrepancies are observed in Figure 6(a) where the half-sine displacement time history is used with the impulsive characteristic time. It is noticed that the maximum wave height measured from the experiment is greater than the maximum displacement of the bed. In the

numerical model developed here, as discussed earlier, it is assumed that the volume change due to the moving boundary be the same as the volume change of the fluid within a computational cell. Thus, cavity between the moving boundary and the fluid is not allowed to occur. However, for the maximum wave height at the center of the moving bed to be greater than the maximum bed displacement, there should be some void between the fluid and the moving bed. It is not possible to determine if there were cavities during the experiments based on the results presented in the paper. In most of the other cases, the numerical results clearly demonstrated the accuracy and capability of the numerical model for the vertically moving channel bottom and wave generation.

Submerged Sliding Block

Sliding of a triangular-shape rigid body on a slope and the resulting wave generation have been examined experimentally and numerically by Heinrich (1992). On a 1:1 slope, the triangular shape block was placed at 0.05 m below the free surface initially. The triangle block was released and slid down the slope due to gravitational force. At the end of the slope a small block is placed to stop the sliding body. The configuration of the experiment is shown in Figure 8.

For the numerical modeling of sliding block and wave generation experiments, the computational domain of size 12 m in the x-direction by 2 m in the y-direction is discretized. Variable grid size is used for horizontal axis with a minimum grid size of 0.01 m and a fixed grid size of 0.01 m is used for vertical axis. To satisfy all the stability conditions of the incorporated method, fixed time step Δt of 5×10^{-4} seconds is used. Numerical results in generation (i.e., near sliding block) and propagation regions are compared with experimental data are shown in Figures 8 and 9. The measured displacement time history from Heinrich's experiment is used as prescribed motion of the triangular block. Since the grid size is not small enough to resolve boundary layer as discussed in the previous study by Lin (1998), the free-slip boundary condition is applied on all the solid boundaries including sliding body, slopes, and channel bottom.

For dynamic equilibrium of sliding block in fluid, wave force, gravity and frictional force between the sliding block and the slope are considered as external forces. In deriving the governing equation for the sliding block motion, each force is decomposed into x and y component according to the local coordinate system as shown in Figure 9.

The gravitational force F_g and its local x and y components F_{gx}, F_{gy} are shown In Figure 9(a). The hydrodynamic forces acting normal to the horizontal and vertical faces of the sliding block are obtained by integration of normal

pressure on the faces and denoted $F_{x'}$, $F_{y'}$, as shown in Figure 9(b). Then the resultant force is decomposed into F_x, F_y, which are the tangential and normal forces, respectively, acting on the slope. The total normal force on the slope, i.e. $F_{gy}+F_y$, is used to compute the frictional force between the sliding block and the slope. Mathematical expressions for the conversion of the forces between the sliding block and the slope are given as

$$F_g = m \cdot g, \quad F_{gx} = F_g \sin 45°, \quad F_{gy} = F_g \cos 45° \tag{17a}$$

$$F = \sqrt{F_{X'}{}^2 + F_{Y'}{}^2} \tag{17b}$$

$$F_x = \sqrt{F_{x'}^2 + F_{y'}^2} \sin\theta, \quad F_y = \sqrt{F_{x'}^2 + F_{y'}^2} \cos\theta \tag{17c}$$

$$\phi = \tan^{-1} \frac{F_{Y'}}{F_{X'}}, \ \theta = 45° - \phi \tag{17d}$$

$$\begin{aligned} \vec{F} = m\ddot{x} &= \textit{gravity force} + \textit{wave force} - \textit{frictional force} \\ &= F_{gx} - F_x - c_f \left(F_{gy} + F_y\right) \\ &= F_g \sin 45° - \sqrt{F_{X'}{}^2 + F_{Y'}{}^2} \sin\theta \\ &\quad - c_f \left(F_g \cos 45° + \sqrt{F_{X'}{}^2 + F_{Y'}{}^2} \cos\theta\right) \\ &= mg \sin 45° - \sqrt{F_{X'}{}^2 + F_{Y'}{}^2} \sin\theta \\ &\quad - c_f \left(mg \cos 45° + \sqrt{F_{X'}{}^2 + F_{Y'}{}^2} \cos\theta\right) \end{aligned} \tag{17e}$$

$$\begin{aligned} m\ddot{x} = mg \sin 45° &- \sqrt{F_{X'}{}^2 + F_{Y'}{}^2} \sin\theta \\ - c_f &\left(mg \cos 45° + \sqrt{F_{X'}{}^2 + F_{Y'}{}^2} \cos\theta\right) \end{aligned} \tag{17f}$$

The resulting governing equation for sliding block motion is given by equation (17f) where c_f denote the friction coefficient and θ the slope angle. The friction coefficient is estimated to be 0.9. This value is obtained by testing several different friction coefficients and applying curve fitting technique. As a numerical method to solve the second order ordinary differential equation, the Newmark method discussed previously is employed in this case.

The displacement time history of the sliding block computed by the fluid-structure interaction model is also compared with experimental data. In the study by Heinrich, the displacement of the moving body could not be computed because of some unidentified numerical instabilities in his numerical model which was developed based on the 2D SOLA VOF model. However, the current model presented in this study shows successfully its capability and accuracy of predicting the displacement of the block as shown in Figure 10.

Two distinct parts of the numerical model are validated though the same set of experimental data. Implementation of the moving boundary algorithm using modified continuity equation is validated by comparing the simulation results with the prescribed motions. The measured time history of the sliding block from the experiment is used as input prescribed motion for the model. Snap shots of wave profiles at 0.5, 1.0, 1.5, and 2.0 seconds from numerical model with the prescribed motions and experimental data are compared and shown in the first column of Figure 11. The iterative procedure

for dynamic equilibrium and its associated solution algorithm are also validated. In the fluid-structure interaction simulation, the displacements is not predetermined or given but computed by the numerical model. The second column of Figure 11 shows the comparisons between experimental data and fluid-structure interaction model results. In the legend, simulation represents the prescribed motion results and interaction represents fluid-structure interaction model results.

In both simulations with prescribed motion and with fluid-structure interaction, a negative wave is generated above the horizontal face of sliding block at 0.5 second. Free surface elevation above the sliding block is decreased until the moving block is stopped by a stopper placed at the bottom of the slope. After the trough is generated, the free surface bounced back along the slope. Runup on the slope and breaking of reflected wave are observed. Part of the fluid was reflected from the slope and the top part of the reflected wave with very steep profile plunged. In the region of breaking waves, it may be difficult to measure the exact free surface elevation with a wave gauge due to the possibility of multiple-valued free surface elevations. Thus, only simulation results are shown in the free surface at 1.5 sec near $x = 2$ m where multiple values of the free-surface elevations were observed. As shown in Figures 11 and 12, it is noticed that the predicted wave profiles in the generation region and the propagation region show good agreement with experimental data.

Aerial Landslide

To verify and validate the algorithm for surface piercing motion of rigid boundary, laboratory test results of aerial landslides where the experimental setup is exactly same as the submerged sliding block except the initial location of block are used. The computational domain, grids and time step used for aerial slide is exactly same as those for the submerged sliding. The same triangular block is located initially just above free surface and then released. The wave profiles in generation region measured at 0.6, 1.0 and 1.5 s are compared with numerical results and shown in Figure 14. From the wave profile at t = 0.6 sec, it is observe that the wave starts to break and becomes highly nonlinear. The discrepancy of wave profiles at t = 1.5 sec may be attributed to turbulence.

The numerical results are in good agreement with experimental data as shown in Figure 14. The good agreements in comparisons with experimental data indicate that the interactions between moving structure/free surface and structure/fluid are modeled accurately in general. As shown in the wave profile at 0.6 sec, experimental data is not available in the region where multiple values of free surface elevation exist. The continuous free surface profile from the contact point of the free surface on moving body surface to the domain boundary would be very useful to examine and validate the structure/free surface interactions in more detail.

Concluding Remarks

A numerical model for the fluid-structure interaction phenomenon is developed in this study. The dynamics of fully submerged and aero structures are modeled as moving rigid boundaries with the surrounding fluid. The volume change due to the moving boundary in a computational cell is implemented by modifying the discrete continuity equation. An iterative procedure is developed to model the coupled structural dynamics and hydrodynamics. Numerical model is validated through three laboratory tests as discussed earlier.

In the moving channel bottom simulations, the free-surface profiles in the generation region are in excellent agreement with experimental data. Also, as shown previously, the capability and accuracy of numerical model are validated with different displacement time histories. Stability and robustness of numerical code is validated through the displacement computation in sliding block comparisons.

To assess the validity of the assumption that the shear stress on the moving boundaries is negligible in the problems examined in this study, tangential and normal components of wave force are computed using friction velocities and pressures. As shown in Figure 14, it is noted that the tangential

forces are less than 2.1 % and 0.07 % of the normal forces on the top and front faces of the sliding body, thus justifying the assumption of negligible shear stress for the particular cases presented in this study.

Additional challenging fluid structure interaction problems will be examined as an application of the numerical model. It is expected that the validated numerical model can be utilized to understand and analyze the complex physical phenomena associated with fluid-structure interaction in near future.

Acknowledgements

Partial support from the National Science Foundation Grants CMS-9908392 and CMS-0217744, and the US Office of Naval Research Grants N00014-92-1221 and N00014-04-10008 are gratefully acknowledged.

Reference

Dean, R.G. and Dalrymple, R.A. 1984. Water wave mechanics for engineers and scientists. Prentice Hall.

Lin, P. 1998. Numerical modeling of breaking waves. Ph.D. Thesis. Cornell University.

Hammack, J.L. 1973. A note on tsunamis: their generation and propagation in an ocean of uniform depth. *J. Fluid Mech.*, **60**, 769-799.

Heinrich, P. 1991. Nonlinear numerical model of landslide-generated water waves. *Int.J. Engr. Fluid Mech.*, **4(4)**, 403-416.

Heinrich, P. 1992. Nonlinear water waves generated by submarine and aerial landslides. *J. Waterway, Port, Coastal and Ocean Engr.*, ASCE, **118**, 249-266.

Hsu, T. 1999. A numerical study of wave-structure interaction using Reynolds Averaged Navier-Stokes equations with k-ε turbulence closure model. MS Thesis. Cornell University.

Lin, P. and Liu, P.L.-F. 1998a A numerical study of breaking waves in the surf zone. *J. Fluid Mech.*, **359**, 239-264.

Lin, P. and Liu, P.L.-F. 1998b Turbulence transport, vorticity dynamics, and solute mixing under plunging breaking waves in surf zone. *J. Geophys. Res.*, **103**, 15677-15694.

Lin, P., and Liu, P.L.-F. 1999 Internal wave-maker for Navier-Stokes equation models. *J. Waterway, Port, Coastal and Ocean Engr.*, ASCE, **125** (4), 207-215.

Lin, P., Chang, K.-A., and Liu, P.L.-F. 1999 Runup and rundown of solitary waves on sloping beaches. *J. Waterway, Port, Coastal and Ocean Engr.*, ASCE, **125** (5), 247-255.

Liu, P.L.F. and Lin, P. 1997. A numerical model for breaking waves: The volume of fluid method. Report No. CACR-97-02. Center for Applied Coastal Research.

Nichols, B.D. and Hirt, C.W. 1971. Improved free surface boundary conditions for numerical incompressible-flow calculations. *J. Comp. Phys.*, **8**, 434-448.

Noda, E. 1970. Water waves generated by landslides. J. Waterways, Harbors and Coastal Engr. Div., ASCE, **125** (4), 207-215.

Rodi, W. 1980 Turbulence models and their application in hydraulics – A state-of-the-art review. I.A.H.R. publication.

Shih, T.H., Zhu, J., and Lumley, J.L. 1996 Calculation of wall-bounded complex flows and free shear flows. *International J. for Numerical Mthods in Fluids*, 23, 1133-1144

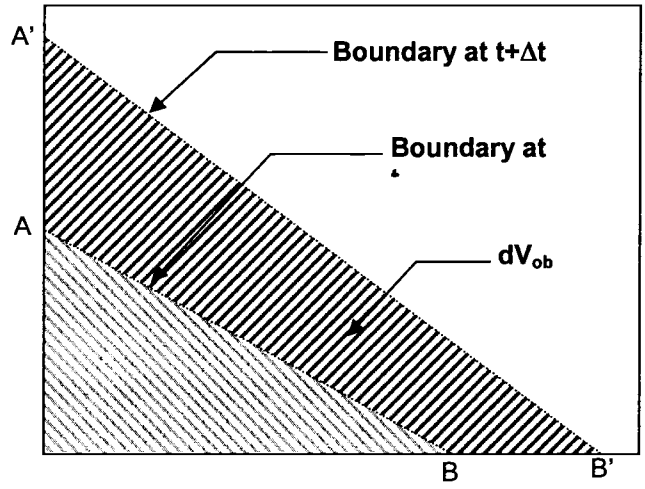

Fig. 1 Fluid volume change within a computational cell due to the moving boundary

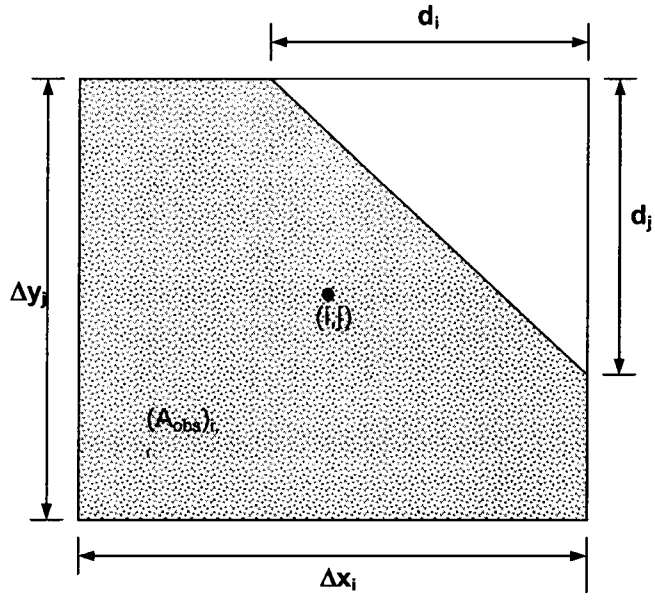

Fig. 2 Partially blocked cell by solid boundary

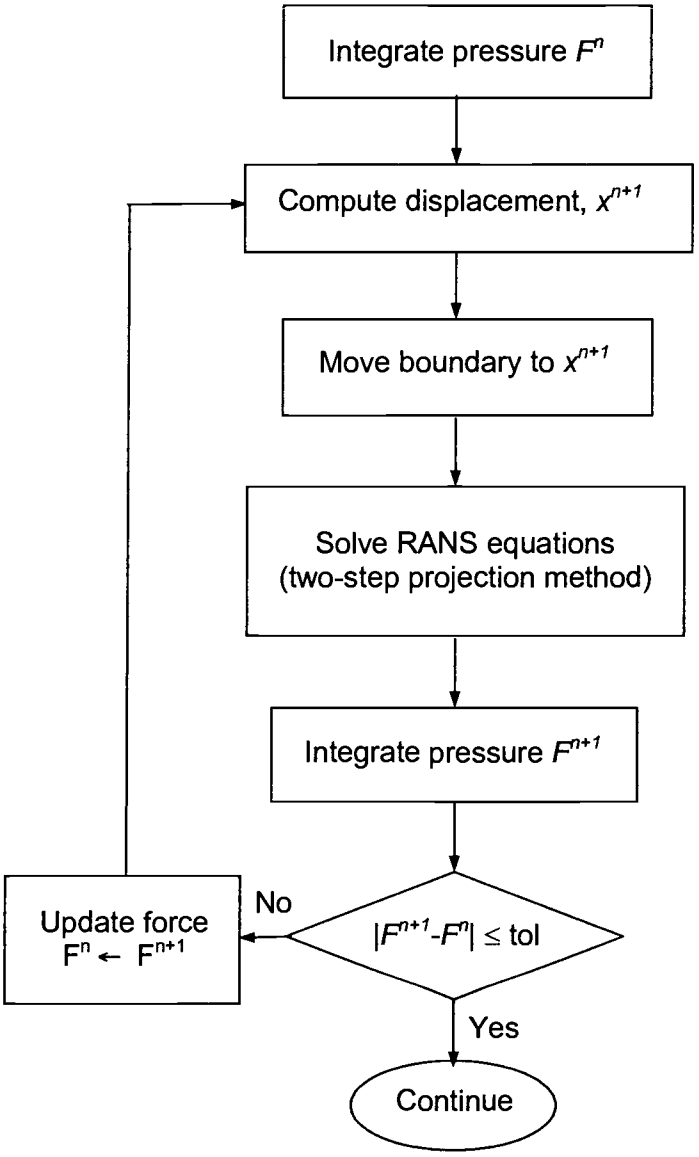

Fig. 3 Flow chart of iteration procedure for force and displacement computation

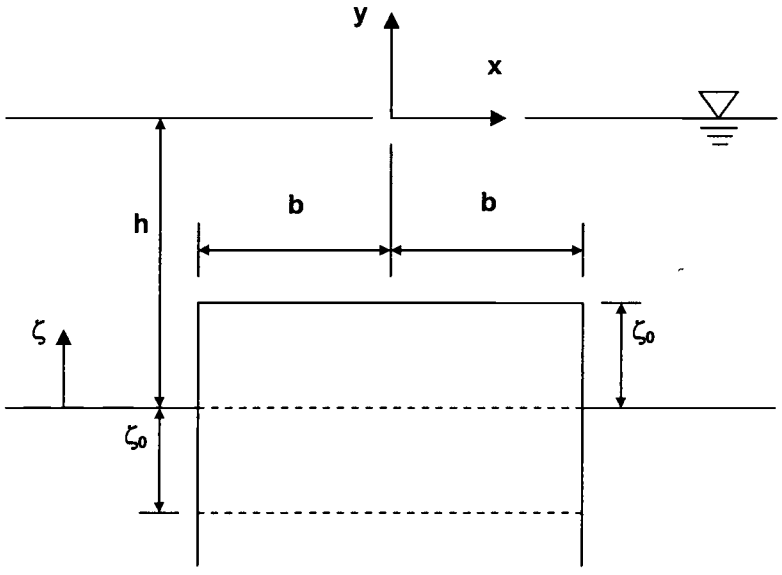

Fig. 4 Theoretical bed deformation model

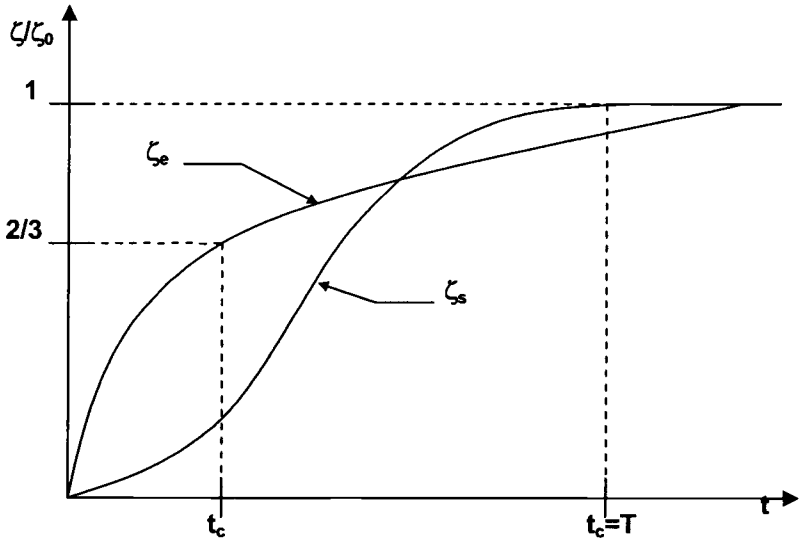

Fig. 5 Time histories of exponential and half-sine bed movements

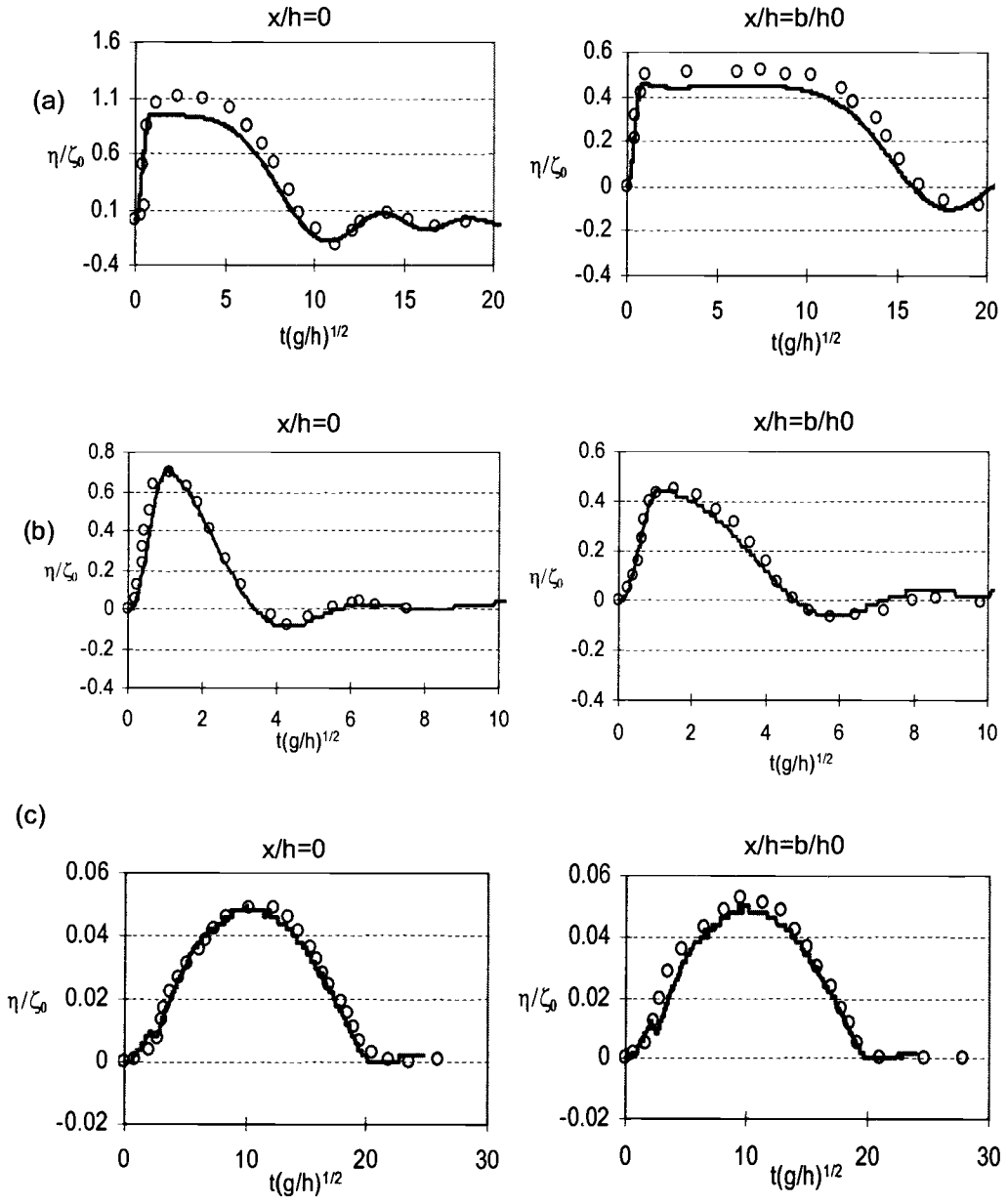

Fig. 6 Comparisons of wave profiles between experimental data and numerical results using half-sine displacement time history for impulsive, transitional and creeping motions: (a) Exponential motion. (b) Transitional motion, (c) Creeping bed motion. ——— Numerical results. oooooooo Experimental data.

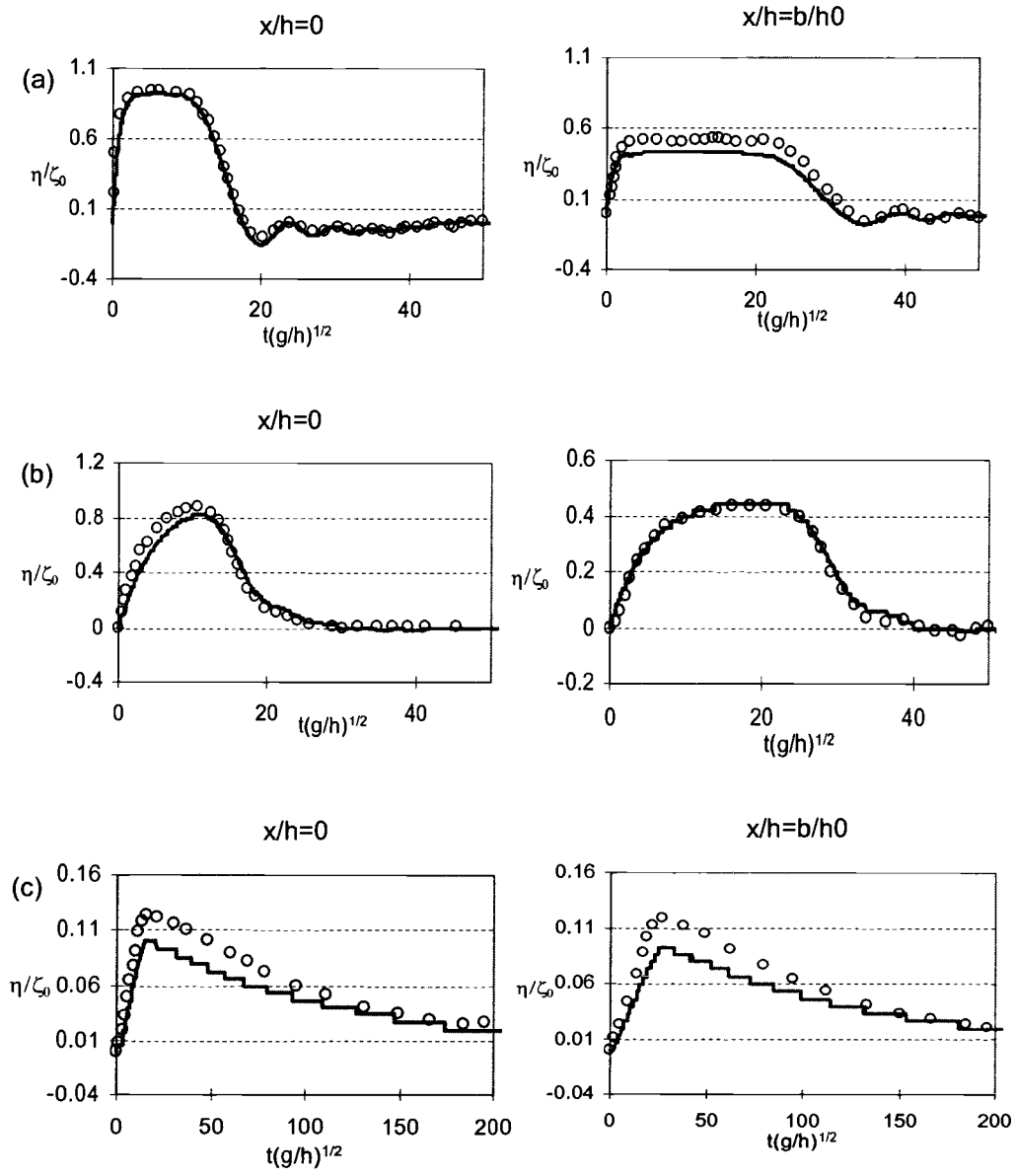

Fig. 7 Comparisons of wave profiles between experimental data and numerical results using exponential displacement time history for impulsive, transitional and creeping motions: (a) Exponential motion. (b) Transitional motion, (c) Creeping bed motion. ——— Numerical results. oooooooo Experimental data.

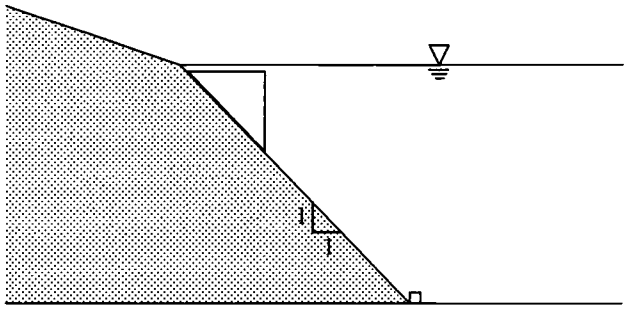

Fig. 8 Experimental setup for sliding block generated waves

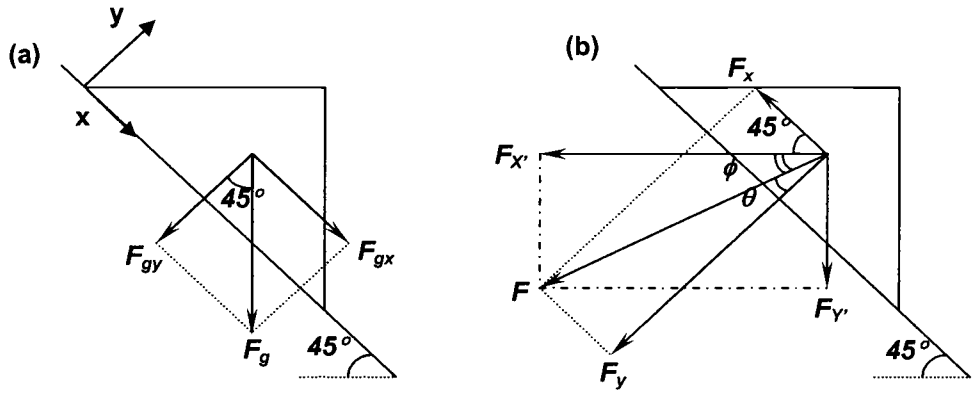

Fig. 9 Forces acting on sliding block and its component: (a) gravity force (b) wave force

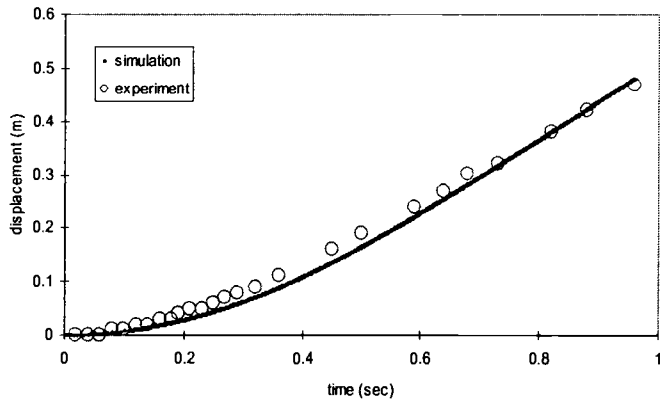

Fig. 10 Displacement time history comparison with experimental data and simulation results

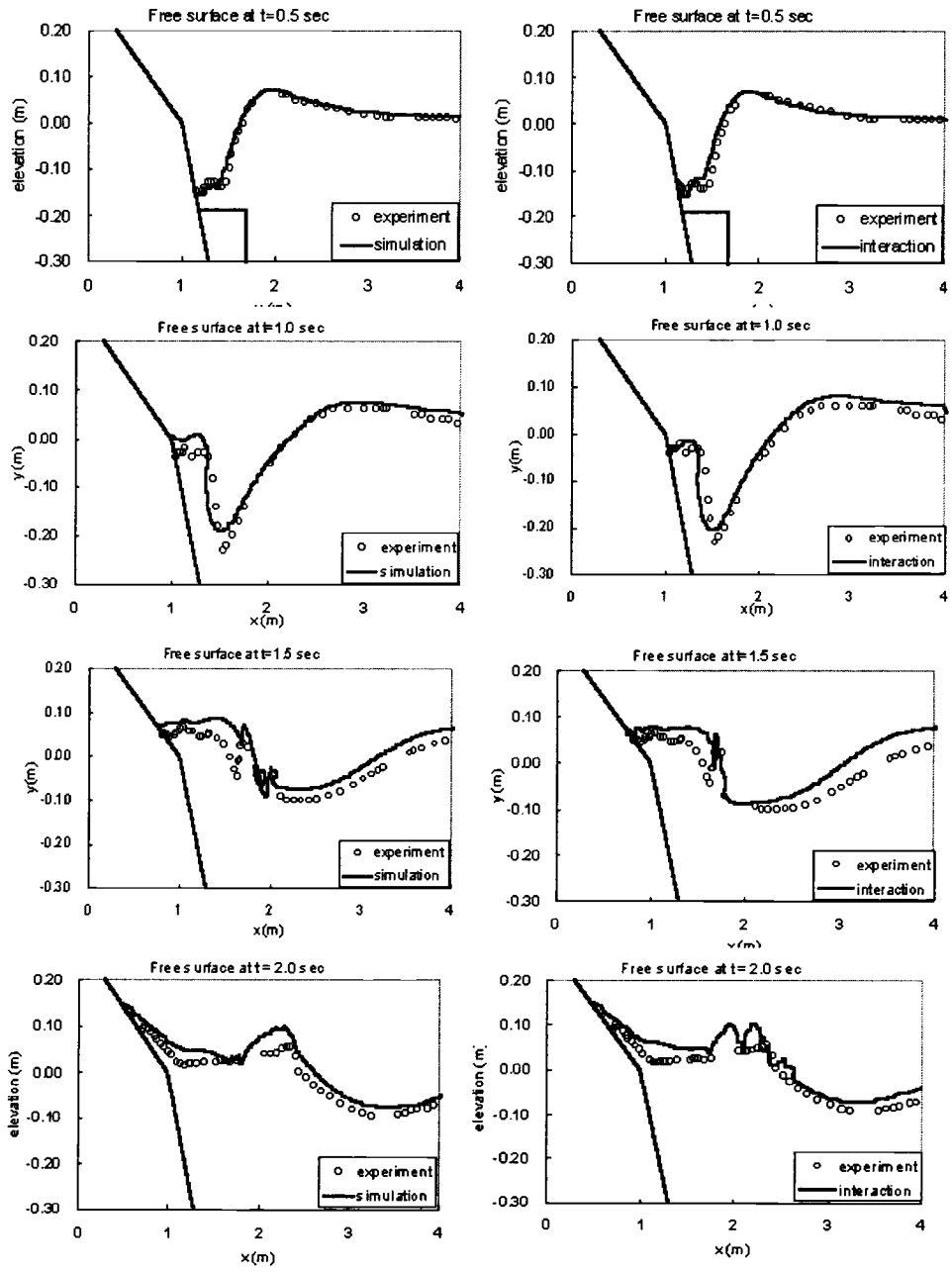

Fig. 11 Free surface comparisons between simulations and experimental data at 0.5, 1.0, 1.5, and 2.0 s in generation region

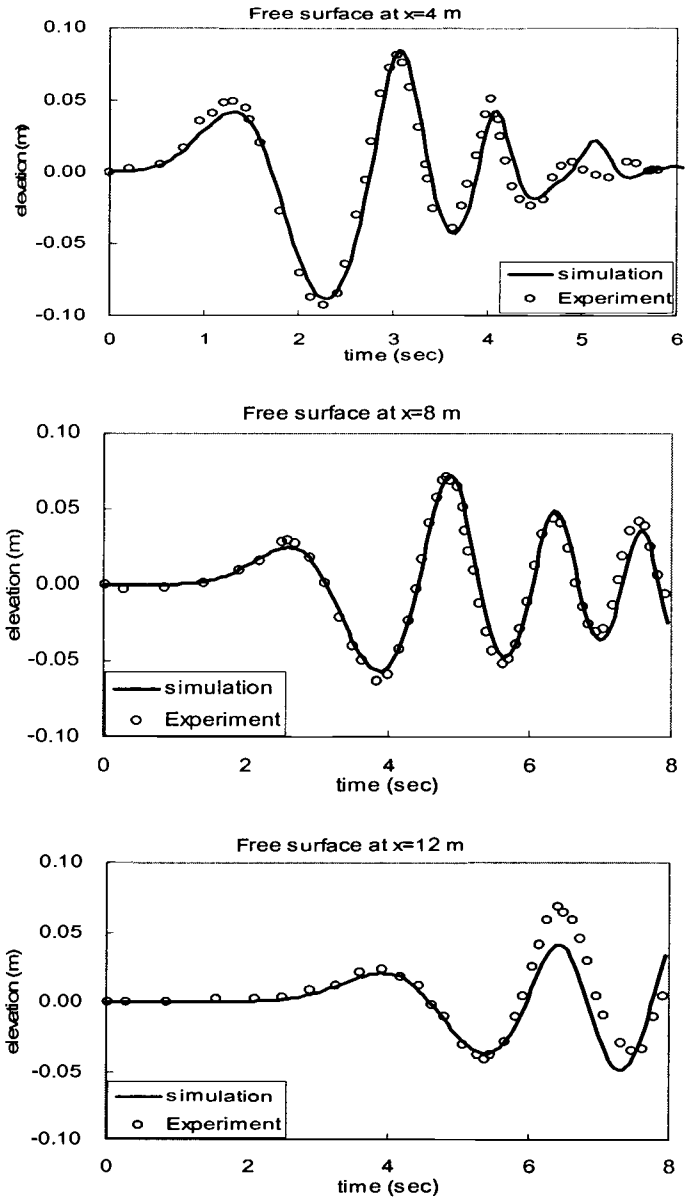

Fig. 12 Free surface comparisons between simulation and experimental data at x = 4, 8, and 12 m in propagation region.

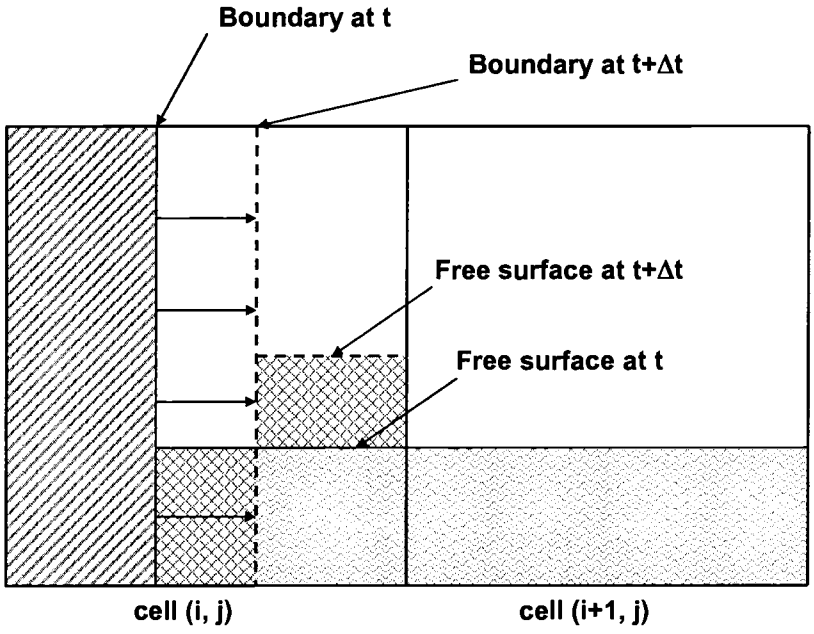

Fig. 13 VOF modification in free surface and moving-boundary interface cell

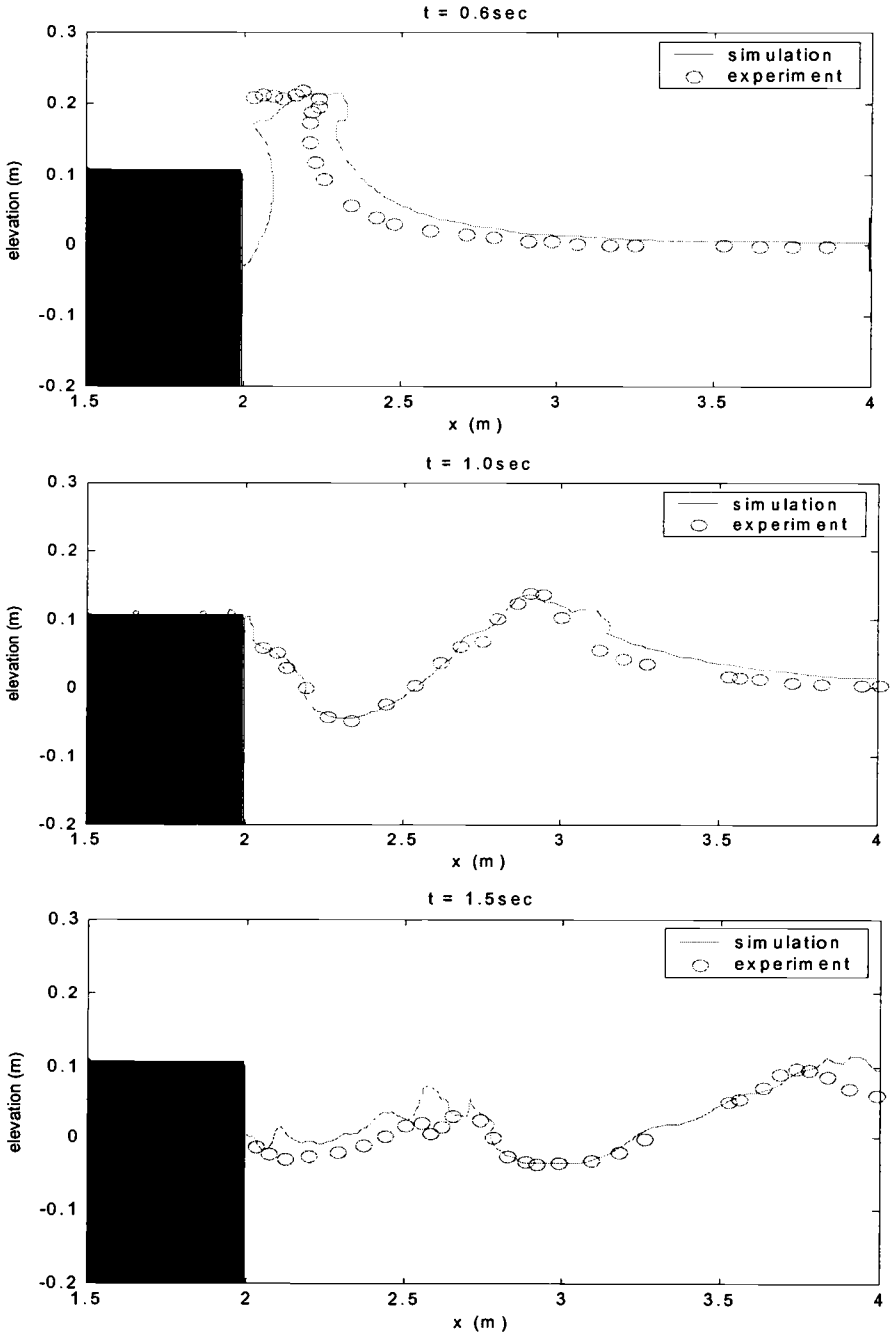

Fig. 14 Free surface comparisons between simulation and experimental data at 0.6, 1.0, and 1.5 s in wave generation region. Solid rectangles shows upper right corner of triangular shape moving boundary.

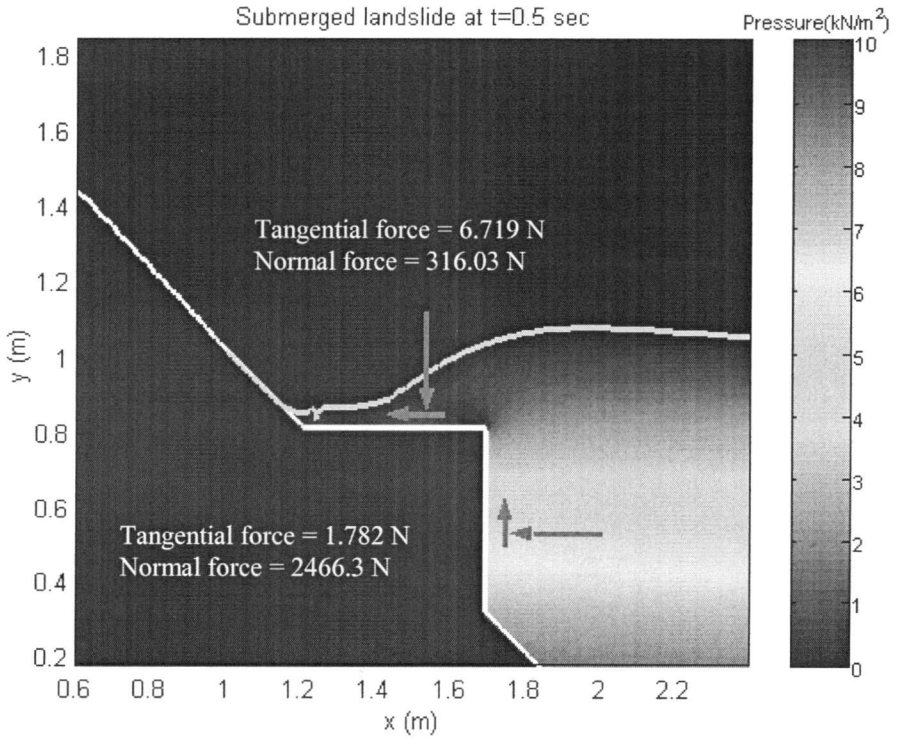

Fig 15. Snapshot of subaerial landslide at 0.5 sec with tangential force and normal force on moving boundaries.

Nomenclature

$ac(i,j)$ fractional volume open to flow in cell (i, j)

b width of moving channel bottom

c damping coefficient

c_f friction coefficient

$C_1, C_{2,}, C_{3,}, C_{d,}, \sigma_k, \sigma_\tau, C_{1\tau}, C_{2\tau}$ empirical coefficients

f_e external excitation

F_g gravitational force

F_{gx}, F_{gy} local x and y components of F_g

g_i i-th component of gravitational acceleration, m/s^2

h water depth

H Heaviside step function

$k(x)$ restoring force

k turbulence kinetic energy

m structure mass

$\vec{n}$ unit normal vector

t_c characteristic time

u_i i-th component of velocity vector

$\vec{u}$ fluid velocity vector

$\vec{v}_{obs}$ moving boundary velocity vector

V volume of a computational cell

$\langle\rangle$ ensemble average

Δx, Δy grid size in x and y direction

ε turbulence kinetic energy dissipation rate

μ dynamic viscosity, kg m^{-1} s^{-1}

ν_t eddy viscosity

θ slope angle

ρ density of fluid, kg/m^3

σ strain rate tensor

τ_{ij}^{m} molecular viscous stress tensor

ζ_0 maximum displacement of moving channel bottom

CHAPTER 4

Analysis of Fluid-Structure Interaction Using RANS Equations, Part II: Application to an Experimental Moored Structure

Yuk, D., Yim, S.C. and Liu, P. L.-F.

Abstract

Dynamic responses of a moored structure subjected to periodic wave excitations are predicted by a 2-dimensional numerical fluid-structure interaction model. For the numerical modeling of fluid, Reynolds Averaged Navier-Stokes equations (RANSE) with the k-ε turbulence closure model is employed. Free surface of waves is tracked by the Volume of Fluid (VOF) method and a piecewise constant scheme is used to reconstruct the free surface. An experimental moored structure approximated as a rigid body in the numerical modeling and the nonlinear equation of motion with polynomial nonlinear restoring force is solved to determine the structural dynamic responses. For the analysis of moored structure dynamics, the Lagrangian formulation is used. Iterative procedures are developed to model fully coupled interactions of the moving rigid body with the surrounding fluid. Moored structures approximated by single degree-of-freedom (SDOF) and multi degree-of-freedom (MDOF) systems are modeled and analyzed. Reasonably good agreements are observed for both the SDOF and the MDOF systems between the structural dynamic response predictions by the numerical model and the laboratory test results. Characteristic behaviors of nonlinear dynamic system such as sub-harmonic, super-harmonic responses are also identified by the numerical model. The time histories of the free surface elevation near

moored structure are also predicted by the current numerical model and compared with experimental data. In general, comparisons of wave profiles near the structure region show good agreements for most of waves tested in the laboratory with various characteristics. The capability and accuracy of the numerical model developed in this study is validated through comparisons with experimental data.

Introduction

The dynamic interaction between fluid and structure has been the subject of great interest to many scientists and engineers for several decays. Many theories and methods have been developed analytically and numerically for the analysis of fluid and structural dynamics and applied to fields of marine structures, naval architectures, tsunami hazard mitigation, etc. Among numerous applications of fluid-structure interaction models, interactions between a moored structure and ocean waves are examined in this study.

To predict wave forces on submerged structures, several theories such as small body, large body and Froude-Krylov have been developed. Although some general criteria about the applicable conditions for each theory have been proposed previously, it is often not clear which theory can predict the wave forces on a structure better than other for the specific conditions at hand. A

numerical model which can be used to predict the wave force accurately under most conditions could provid better understanding of the physics of moored structural dynamics under hydrodynamic excitations. In this study, comparisons with experimental data are made as a mean of assessing the accuracy of the present numerical models. In addition to predicting of wave force, the moored structure under periodic and random waves also features nonlinear behaviors such as amplitude jump phenomena, coexisting attractors and bifurcation, which also make the response behavior and hence the analysis even more complex.

In this study, the numerical model is developed to predict the dynamic responses of moored structure subjected to the periodic wave force excitations. General application procedures of the fully coupled fluid-structure interaction model for the moored structure analysis will be discussed. Comparisons between simulations and laboratory test results are made to validate the capability and accuracy in prediction of the moored sphere responses under hydrodynamic excitation forces. Limitations and capabilities of the numerical model observed in the modeling of experimental moored structure will also be discussed.

In order to apply the fluid-structure interaction model to analyze an experiment, a numerical model need to consider the experimental setup, the dimensions, material properties and input parameters used in the laboratory

experiments. Then the equation of motion (EOM) for structures need to be derived based on a Lagrangian formulation. Derivation of the EOM starts with the analysis of internal and external forces associated with the structural system and hydrodynamic environment. All the coefficients that appear in the EOM should be determined based on the experimental configuration, material properties and appropriate system identification techniques.

Once the EOM for moored structural system is formulated, the numerical method to solve the EOM should be determined. Depending on the structural system and types of EOM, different numerical techniques might be required.

Appropriate boundary conditions for rigid moving boundaries and computational domain boundaries should be determined. In addition, the appropriate grid size in horizontal and vertical directions also need to be considered based on the given wave conditions and the region of interest. In general, finer grids are needed near moving boundaries to ensure accurate modeling of interactions between structural system and surrounding fluid. Since the boundary conditions and grid size are among the most important factors which can affect the stability and accuracy of the numerical modeling, careful consideration is required in applying boundary conditions and determining grid size.

The analysis procedure adopted in this study may be summarized in the following steps:

1. Development of numerical model based on experiment setup
2. Consideration of forces associated with structure and fluid
3. Derivation of EOM for structure system
4. Identification of coefficients in EOM
5. Determination of boundary conditions and grid size

Description of Laboratory Tests

A series of laboratory tests has been conducted to examine the nonlinear behavior of moored structure under wave excitation at Wave Research Laboratory at Oregon State University. The profile view of the 2-dimensional large wave flume and the location of the moored structure and the wave generator are shown in Figure 1. The test results have been investigated and analyzed using a small body theory, independent flow field theory and fully nonlinear potential flow model by Lin *et al* (2002, 2004).

Experiments consist of a sphere with 0.457 m diameter made of PVC and strings attached to the sphere. Hinged wave maker placed at the left end is used to generate periodic waves in the 2 dimensional flume which is 104 m long, 3.7 m wide and 4.6 m deep with an artificial beach placed at the other

end of flume to absorb the wave energy. The sphere is filled with water and is neutrally buoyant when fully submerged. In a previous study (Gottlieb *et al*, 1997), it is shown that the restoring force from the mooring lines attached to the sphere is nonlinear and can be approximated by a third order polynomial. For the single degree of freedom (SDOF) model, a steel rod is placed through the center of the sphere to restrict the motion to surge direction only. To minimize the friction between the sphere and the rod, steel bearings were inserted. In the multi degree of freedom (MDOF) tests, the steel rod is removed so that the sphere can move or rotate in surge, heave and roll directions. However, in modeling the moored sphere as MDOF system, only surge and heave motions are considered because the experimental data show that the roll motion of sphere is negligible.

Development of Numerical Model

Development of Numerical Model based on Experimental Configuration

The sphere of known radius which was used in the laboratory test is converted to an "equivalent" cylinder of undetermined diameter as in the previous study by Lin *et al* (2002). A target circle radius is chosen as the most likely to match based on the assumption that the hydrodynamic forces on a circle of unit width will match the hydrodynamic forces on the average radius

of the sphere. Accordingly, Figure 2 shows the geometric basis for the choice of circle diameter, and equation (1) shows how the target radius is selected.

$$b = \frac{R}{2}\int_0^{\pi} \cos^2\theta d\theta = \frac{\pi}{4}R \qquad (1)$$

Waves are generated by the wave board hinged at the bottom driven hydraulically by a piston that is digital controlled. In the numerical model, waves are generated at the left boundary of computational domain by specifying the velocities and free surface elevations based on linear wave theory, stokes 4^{th}, 5^{th} order wave theory, and cnoidal wave theory. On the right side of the computational domain, artificial damping zone is placed to prevent wave reflection from the boundary.

Modeling of Forces Associated with Structure and Fluid

The following forces associated with the experimental moored structure system are taken into consideration, the hydrodynamic forces from the fluid; structural and hydrodynamic damping forces; restoring forces from the mooring lines and inertia force from the structure mass. The hydrodynamic forces are obtained by integrating the dynamic pressure from the fluid over the surface of moving structure which can be expressed as

$$f_{ext}(t) = \iint_A \vec{n} \cdot p(t)\, dxdy \qquad (2)$$

where *p(t)* is the hydrodynamic pressure obtained by solving the RANS equations, $\vec{n}$ is the unit normal vector to the material body surface. The details of external force computations will be discussed later in this paper.

The hydrodynamic force component, which is tangential to the material body surface, is neglected due to the boundary conditions imposed on the moving solid boundaries, i.e., "free-slip" boundary condition.

Equation of Motion for the Structural System

The experimental moored system is modeled as a mass, spring and dashpot system with nonlinear restoring force due to the geometric configuration of mooring lines. The schematic diagram of the numerical model for the EOM derivation is shown in Figure 3. It is known from the previous study by Yim *et al* (1991) that the restoring forces provided by the mooring lines can be approximated by the third order polynomials shown in equation (3a). The EOM for the MDOF system has also been extensively examined and expressed by Yim *et al* (2000) as in equation (3b).

$$\text{SDOF}: \; m\ddot{x}_1 + c\dot{x}_1 + k_1 x_1 + k_2 x_1^2 + k_3 x_1^3 = f_{ext1} \tag{3a}$$

$$\text{MDOF}: \begin{array}{l} m_1\ddot{x}_1 + c_1\dot{x}_1 + k_{11}x_1 + k_{12}x_1^2 + k_{13}x_1^3 + k_{14}x_1x_2^2 = f_{ext1} \\ m_2\ddot{x}_2 + c_2\dot{x}_2 + k_{21}x_2 + k_{22}x_2^2 + k_{23}x_2^3 + k_{24}x_1^2x_2 = f_{ext2} \end{array} \tag{3b}$$

where x_1, x_2 are displacements of material body in surge and heave direction, respectively, m is the mass, c is the damping coefficient, k_1, k_2, k_3 are the restoring force coefficients and f_{ext1}, f_{ext2} are the external forces on rigid structure from hydrodynamic pressures in the surge and heave directions. In equation (3), the dot and double dot on the displacements represent the first and second derivatives of x with respect to time and the time variable, i.e., t, is suppressed for simplicity. The last terms on the left hand side of equation (3b) show the coupling effect of surge and heave motions on the structural dynamic responses.

The structural damping force(s) is (are) assumed to be linear, proportional to the velocity of material body, i.e., $c\dot{x}_1$ or $c_1\dot{x}_1$, $c_2\dot{x}_2$.

Identification of Coefficients in the EOM

In the EOM for the SDOF and MDOF systems as given in equation (3), various coefficients are determined directly from the material properties and/or by applying system identification techniques. For the mass of the moored structure in the numerical model, the measured weight of the structure is converted based on the "equivalent" cylinder conversion described earlier in this paper. For the coefficients of the restoring forces, the restoring force, $f_s(\Delta x_1)$, is defined based on the geometry of the system as

$$f_s(\Delta x_1) = \left(\frac{F_o}{\sqrt{sl^2 + \Delta x_1^{\,2}}} + \left(1 - \frac{sl}{\sqrt{sl^2 + \Delta x_1^{\,2}}} \right) K \right) \Delta x_1 \qquad (4)$$

where F_o, sl, Δx_1 and K denote initial spring tension, initial spring length, structure displacement in the surge direction and the linear spring constant, respectively. Figure 4 shows the variations of restoring forces as a function of the structure displacement. The coefficients of restoring forces are determined such that the approximated restoring force with a third order polynomial can best approximate the restoring forces i.e., $f_s(\Delta x_1)$ in equation (4). The restoring force coefficients for MDOF system are determined similarly.

For the damping coefficients, it is found in the previous study by Yim et al (1999) that 3 % of the critical damping for SDOF system and 1 % for MDOF system can be used to approximate the damping force of the experimental moored structure based on the small body approximation. The damping coefficients are calculated as shown in equation (5).

$$C = \xi C_{cr} = \xi(2m\omega) \qquad (5)$$

where m is the mass of the moored structure and ω is the natural frequency of the structural system in radian. A set of coefficients used in the numerical simulations is adopted from the previous study by Narayanan and Yim (2004).

Determination of Boundary Conditions and Grid Size

Appropriate boundary conditions need to be specified in the modeling of experimental moored structure. In the current numerical model, it is possible to impose the no-slip boundary condition or the free-slip boundary condition on the solid boundary. However, since the grid size is not sufficiently fine to resolve the boundary layer on the material body surface, the free-slip boundary condition is used as suggested by Lin (1998). At the left boundary of the computational domain, the velocities and free surface elevation are specified to generate the trains of waves based on the various linear and nonlinear wave theories such as Stoke's 4^{th}, 5^{th} order waves and cnoidal waves. At the other boundary of the computational domain, the so-called "open" (or radiation) boundary condition is imposed so that the waves can propagate through the domain boundary without reflections. To prevent possible reflection from the right domain boundary, an artificial sponge layer is also used to damp out the waves.

For mesh generation, the grid size in horizontal and vertical directions, i.e., δx and δy, need to be determined. Ideally, the same order of magnitude in grid sizes, i.e., $\delta x \cong \delta y$, is recommended to avoid any possible numerical errors. However, in the case of moored structure experiments, relatively large size of δx compared to δy are used to resolve the waves with long wave lengths. Using

non-uniform grid sizes, fine grids are generated near moving rigid body region and less fine grids are used in the other region.

Iterative Procedure for Dynamic Equilibrium

To advance the predicted response motion of the submerged rigid body under hydrodynamic excitations, external forces acting on the rigid body at (n+1)-th time level are required. However, the displacement of the moored structure between n-th and (n+1)-th time step is unknown. Since the hydrodynamic excitation forces at (n+1)-th time step depends partially on the structural displacement, the forces acting on the structure are also unknown at (n+1)-th time step. Thus an iterative procedure is introduced to estimate the displacement and forces at (n+1)-th time step. The iterative procedure begins with the estimated force, $\tilde{F}_I^n$ which is obtained by integrating the pressure along the structure boundary at t^n. The subscript and superscript of $\tilde{F}_I^n$ denote the number of iterations and the time level, respectively. Then the equation of motion for the structure with $\tilde{F}_I^n$ is solved to determine the displacement of moving boundary, $\tilde{x}_I^{n+1}$. The pressure is then integrated along the boundary again to compute the total force on the structure after boundary moved to $\tilde{x}_I^{n+1}$. Then the resulting force obtained with updated boundary location at $\tilde{x}_I^{n+1}$ is set

to be $\widetilde{F}_2^n$ and used as an updated estimate of the external force at time t^{n+1}. By repeating this procedure until the estimated force at t^{n+1} converges to F^{n+1} and satisfies a preset convergence criteria, the final external force F^{n+1} and boundary location x^{n+1} at t^{n+1} are resolved. A flow chart of the iterative procedure is shown in Figure 5.

Integration of the second order nonlinear ordinary differential equations (ODE) is performed using the Euler method. The accuracy of Euler method is known to be O(Δt). Higher order numerical methods for integration of ODE, (e.g., Runge-Kutta 4th order method) had been considered. However, the higher order method requires the exact excitation force at the next time step. When excitation force can be calculated or determined exactly at any time step, higher order methods can be employed in the numerical model to improve the accuracy in predicting the structural responses. Because the excitation force at the next time step is not known and estimated at the current time step, the effect of implementing higher order method such as Runge-Kutta 4th order method to improve the accuracy of structural response prediction is expected to be negligible.

Numerical Results and Discussions

The numerical model developed in this study is applied to predict and analyze 12 laboratory tests with various wave periods and wave heights. The wave periods and heights are varied from 1.33 sec to 12 sec and from 0.1 m to 0.8 m, respectively as shown in table 1 and 2. Wave numbers and wave lengths are computed using the dispersion equation and the series of laboratory tests are categorized into deep, intermediate and shallow water conditions based on the criteria proposed by Chakrabarti (1987). Among several wave gauge data, the time series of free surface elevation measured by the wave gauge at the location of 0.46 m ahead of the sphere are examined. The displacements of rigid body in surge and heave direction are recorded based on the variation of the string attached to the sphere. More detailed and complete descriptions regarding the physical configuration and analysis of the laboratory tests can be found in the report by Yim *et al* (1993).

The computational domain is discretized with non-uniform structured grids and numerical wave gauges are placed at exactly same locations as in the laboratory tests to record free surface elevation and to compare the numerical results with the experimental data. Relatively smaller grid sizes are used near the moving rigid body region for better resolution of solid structure boundary.

Table 1 Wave parameters used in experiments of SDOF system

Test	H (m)	T (sec)	L (m)	h/L	Remarks
D1	0.20	1.3	2.64	1.04	Deep water
D2	0.76	2.0	6.19	0.44	Intermediate water
D3	0.61	6.5	32.23	0.08	Intermediate water
D9	0.55	2.0	6.19	0.44	Intermediate water
D14	0.10	3.7	16.60	0.17	Intermediate water

Table 2 Wave parameters used in experiments of MDOF system

Test	H (m)	T (sec)	L (m)	h/L	Remarks
E2	0.34	1.43	3.19	0.86	Deep water
E3	0.22	1.25	2.44	1.13	Deep water
E4	0.41	10.0	50.89	0.05	Intermediate water
E5	0.37	6.67	33.15	0.08	Intermediate water
E6	0.49	2.22	7.53	0.36	Intermediate water
E7	0.30	12.0	61.42	0.04	Shallow water
E13	0.34	2.22	7.53	0.36	Intermediate water

In the numerical tests, the wave number and corresponding wave length are determined based on the dispersion equation for the given conditions, i.e., wave height, wave period and water depth. Depending on the wave length of each test, the horizontal length of computation domains and grid sizes are varied to make computation more efficient and stable. The length of the damping zone is also increased in the tests with longer wave length.

The damping coefficient and restoring force coefficients used in the equation of motion for structural dynamics are adopted from the previous study of system identification method by Narayanan (1999) and adjusted slightly for

the best fit in the current model. Once those coefficients are fine tuned, the set of coefficients for structural dynamics are held constant throughout each set of experimental data to check the robustness and consistency of current numerical model. The coefficients of EOM used in modeling of the experimental moored structure are shown in Table 3.

Table 3 Coefficients of EOM for SDOF and MDOF system

	[m]	[c]	[k]
SDOF	[105]	[0.03]	[412.24 558.25 1832.18]
MDOF	$\begin{bmatrix} 105 \\ 105 \end{bmatrix}$	$\begin{bmatrix} 0.03 \\ 0.01 \end{bmatrix}$	$\begin{bmatrix} 412.24 & 558.25 & 1832.18 & 4580.45 \\ 412.24 & 558.25 & 1832.18 & 5038.5 \end{bmatrix}$

The effect of steel rod which is installed in the laboratory tests to restrict the moored structure motion to surge direction only for SDOF system is assumed to be negligible and is ignored in the numerical modeling. It is assumed that friction between steel rod and sphere is negligible due to bearings. In wave force computation, only the normal force to rigid body surface is considered and the tangential component of wave force is neglected in the current model, i.e., free-slip condition is applied on the moving rigid body boundaries. Normal component of wave forces along the rigid body surface is integrated to compute the total wave force acting on the rigid body.

Numerical results are generally in good agreements with experimental data for both SDOF and MDOF systems as shown in Figures 6-17. Nonlinear response characteristics such as harmonic response, sub-harmonic response and super-harmonic response are successfully identified by the current fluid-structure interaction model. However, some disagreements are observed in those cases with long wave periods, i.e., Test E4, E5, E7. In numerical tests with wave periods of 6.67 sec, 10 sec and 12 sec, it is noticed that numerical model tends to overestimate the amplitude of structure response in heave motion and the high frequency components of structure responses are more prominent in the numerical results than the experimental data. Those disagreements between the numerical results and the experimental data may be caused by the strong nonlinearity in waves and the energy accumulation in the flume.

Even though 2-dimensional numerical model is utilized to describe 3-dimensional sphere motions, numerical results are generally in very good agreements with the measured data as shown in the comparisons. Considering the current computing resources available and computation intensity required for 3-dimensional model in general, current 2-dimensional numerical model might be chosen as an alternative way to analyze 3-dimensional fluid-structure interaction problems more efficiently in terms of computational efforts.

To assess the validity of assumption that tangential force is negligible, normal and shear force components are computed by integrating stresses along the surface of rigid body. It is observed in MDOF system test (Test E3) as shown in Figure 18 that the ratios of tangential force to normal force are 0.23% (=0.104N/45.0N) and 0.072% (0.0234N/32.5N) in horizontal and vertical directions respectively. It is concluded that the effect of tangential stress on rigid body motion is negligible.

Concluding Remarks

The fluid-structure interaction model with RANS equations is applied to analyze the nonlinear dynamic response of moored structure under periodic waves. The dynamic structural systems are modeled by SDOF and MDOF system. The nonlinearities in waves and associated effects on structural systems are examined.

Numerical simulations are conducted for 12 tests with various water depths, wave heights and wave periods. The characteristic behaviors of the nonlinear dynamic structure (i.e., sub-harmonic and super-harmonic responses) are observed in numerical simulations. The numerical results are compared with experimental data and reasonably good agreements are observed in general.

Acknowledgements

Partial support from the National Science Foundation Grants CMS-9908392 and CMS-0217744, and the US Office of Naval Research Grants N00014-92-1221 and N00014-04-10008 are gratefully acknowledged.

.

References

Chakrabarti, S.K. 1987. Hydrodynamics of Offshore Structures. Springer-Verlag.

Chang, K. 1999. Experimental study of wave breaking and wave-structure interaction. Ph.D. Thesis. Cornell University.

Lin, H. and Yim, S. C. S. 2004. Stochastic analysis of a single-degree-of-freedom nonlinear experimental moored system using an independent-flow-field model. *J. Engineering Mechanics*, 130I2, 161-170

Lin, P. 1998. Numerical modeling of breaking waves. Ph.D. Thesis. Cornell University.

Lin, P. and Liu, P.L.-F. 1998a A numerical study of breaking waves in the surf zone. *J. Fluid Mech.*, 359, 239-264.

Lin, P. and Liu, P.L.-F. 1998b Turbulence transport, vorticity dynamics, and solute mixing under plunging breaking waves in surf zone. *J. Geophys. Res.*, 103, 15677-15694.

Lin, P., and Liu, P.L.-F. 1999 Internal wave-maker for Navier-Stokes equation models. *J. Waterway, Port, Coastal and Ocean Engr.*, ASCE, 125 (4), 207-215.

Lin, P., Chang, K.-A., and Liu, P.L.-F. 1999 Runup and rundown of solitary waves on sloping beaches. *J. Waterway, Port, Coastal and Ocean Engr.*, ASCE, 125 (5), 247-255.

Liu, P.L.F. and Lin, P. 1997. A numerical model for breaking waves: The volume of fluid method. Report No. CACR-97-02. Center for Applied Coastal Research.

Lynett, P.J. and Liu, P.L.-F. 2002 A numerical study of submerged landslide generated waves and runup. *Proc. Royal Soc.*, A. 458, 2885-2910.

Mei, C.C. 1989. The applied dynamics of ocean surface waves. World Scientific.

Narayanan, S. and Yim, S.C.S. 2004. Modeling and identification of a nonlinear SDOF moored structure, Part 1—Hydrodynamic models and algorithms. *J. of Offshore Mechanics & Arctic Engineering*. 126 I2, 175

Narayanan, S. and Yim, S.C.S. 2004. Modeling and identification of a nonlinear SDOF moored structure, Part 2—Comparisons and sensitivity study. *J. of Offshore Mechanics & Arctic Engineering*. 126 I2, 175

Lin, H., Robinson, D., Yim, S.C.S., and Tanizawa, K. 2002. Prediction of Surge Motions of a Submerged Body Using a Fully Nonlinear Wave-Structure-Interaction Model. *Proceedings of the Eleventh International Offshore and Polar Engineering Conference*, Kitakyushu, Japan, 263-270.

Yim, S.C.S., Myrum, M.A., Gottlieb, O., Lin, H. and Shih, I-Ming. 1993. Summary and preliminary analysis of nonlinear oscillations in a submerged mooring system experiment. Report No. OE-93-03. Office of Naval Research.

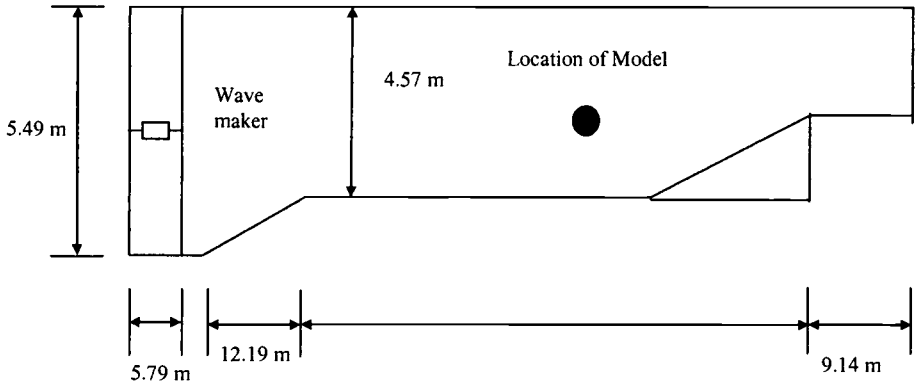

Fig. 1 Profile view of the experimental model in a 2-D wave flume

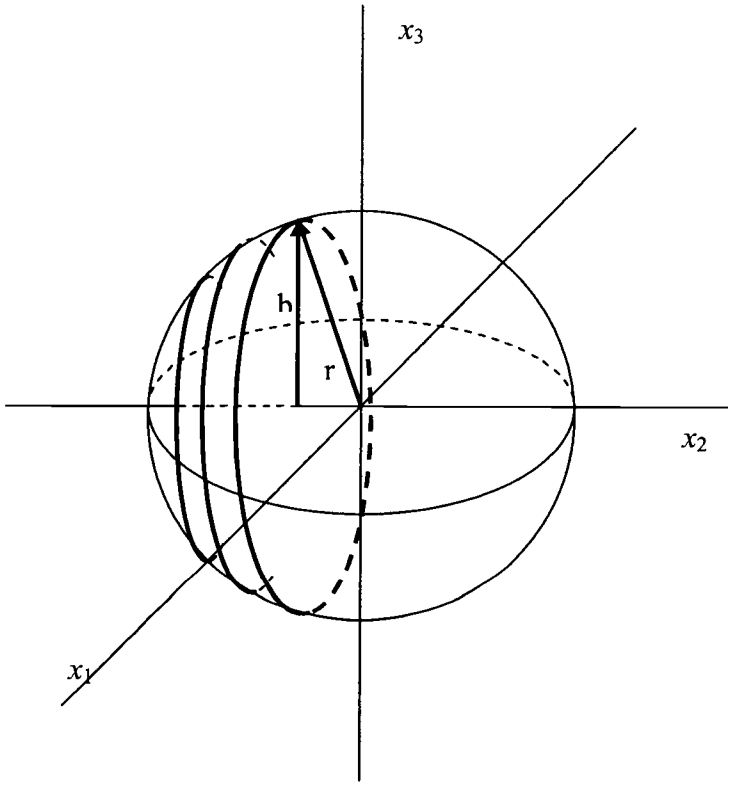

Fig. 2 Sphere of radius R with average disk of radius b

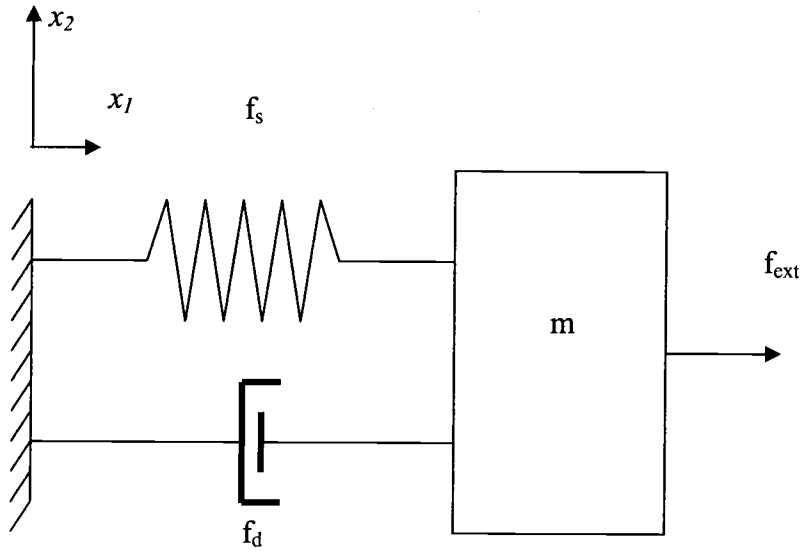

Fig. 3 Schematic diagram of mass, spring and dash-pot system with external force

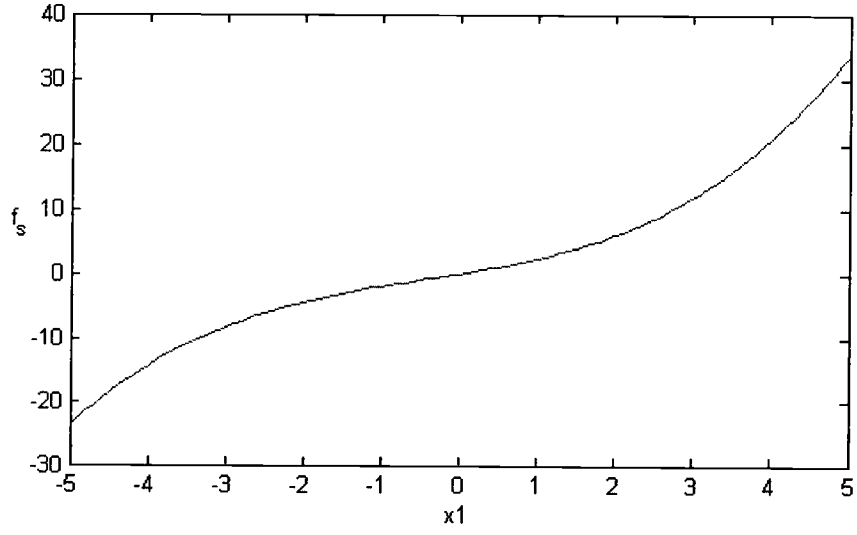

Fig. 4 Restoring force from mooring lines

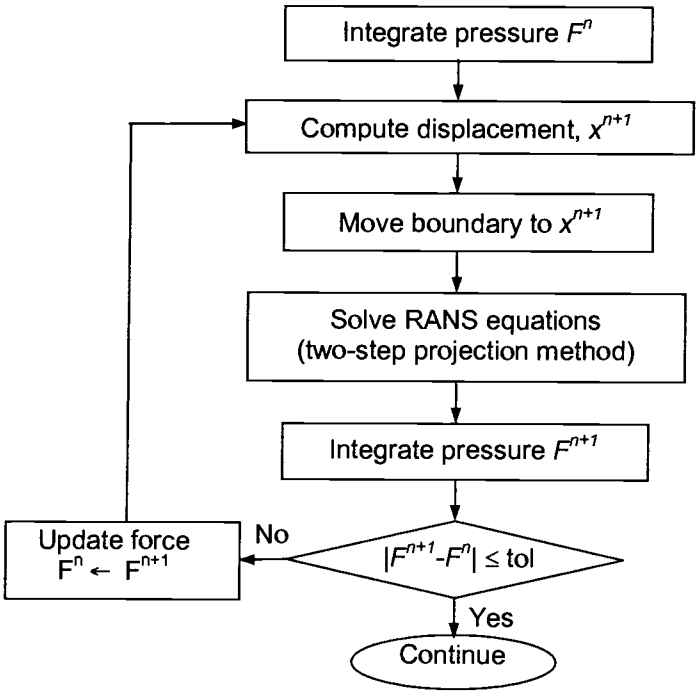

Fig. 5 Flow chart of iteration procedure for dynamic equilibrium

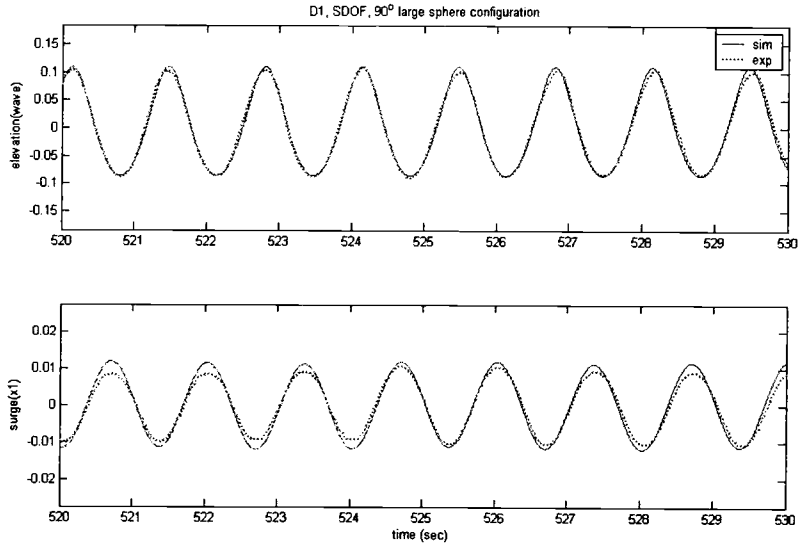

Fig.6 Time series of free surface elevation and surge response of structure (Test D1)

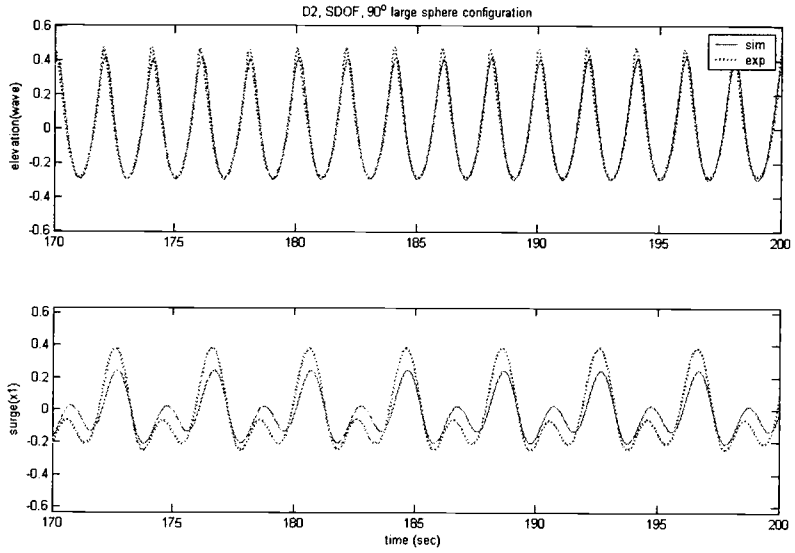

Fig.7 Time series of free surface elevation and surge response of structure (Test D2)

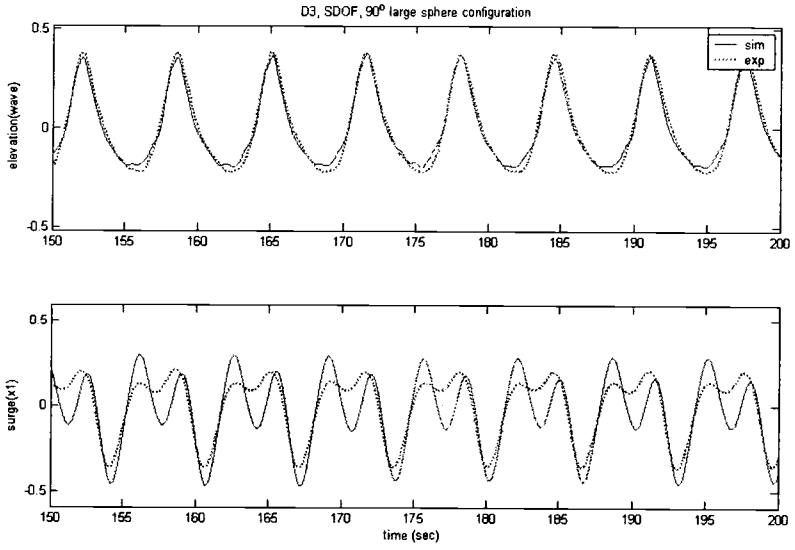

Fig.8 Time series of free surface elevation and surge response of structure (Test D3)

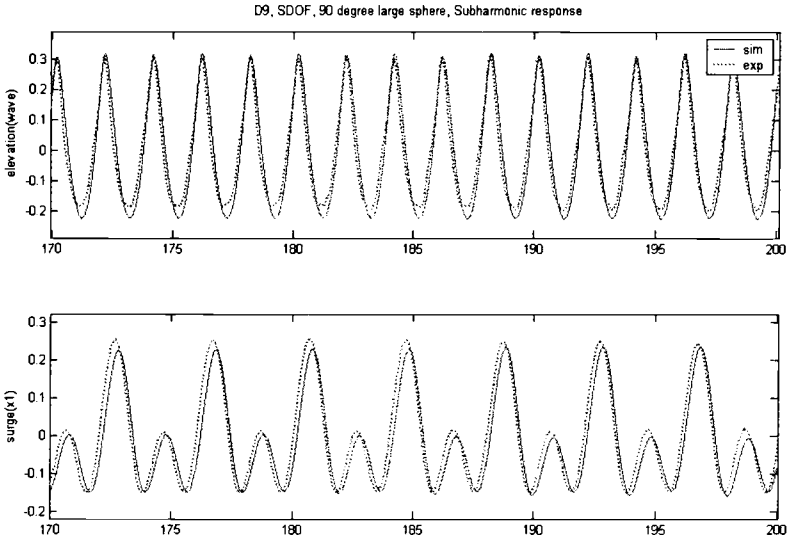

Fig.9 Time series of free surface elevation and surge response of structure (Test D9)

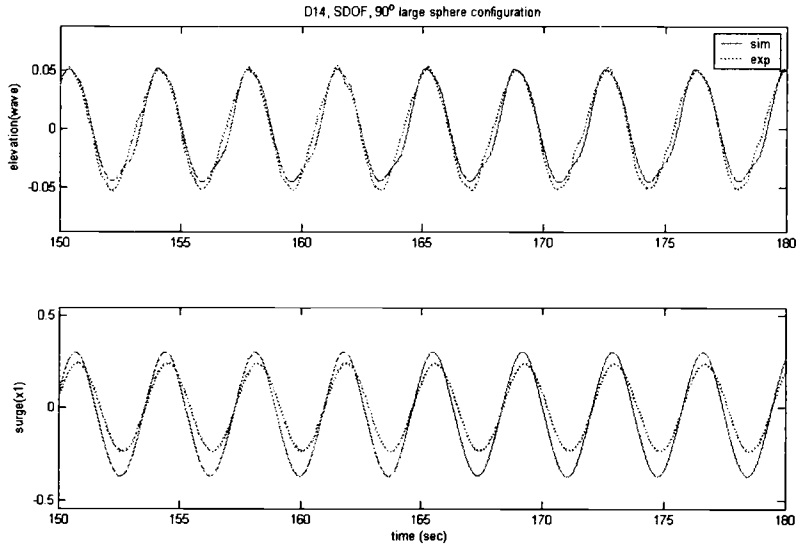

Fig.10 Time series of free surface elevation and surge response of structure (Test D14)

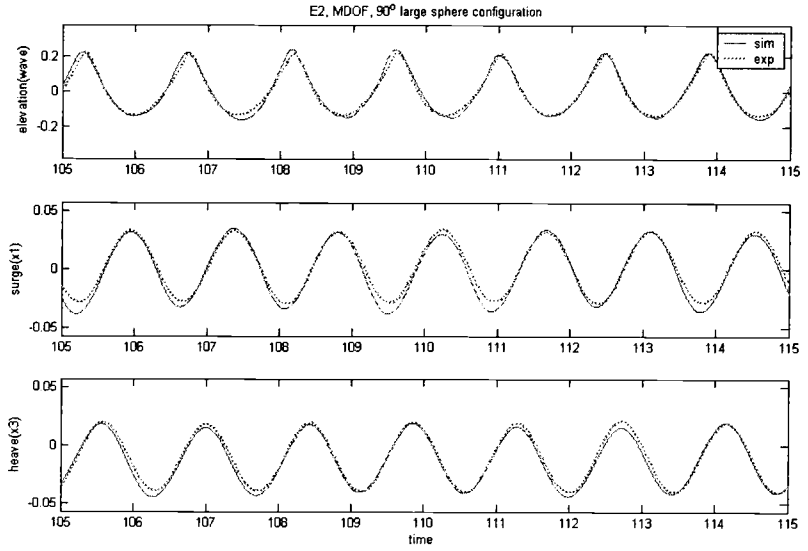

Fig.11 Time series of free surface elevation, surge and heave responses of moored structure (Test E2)

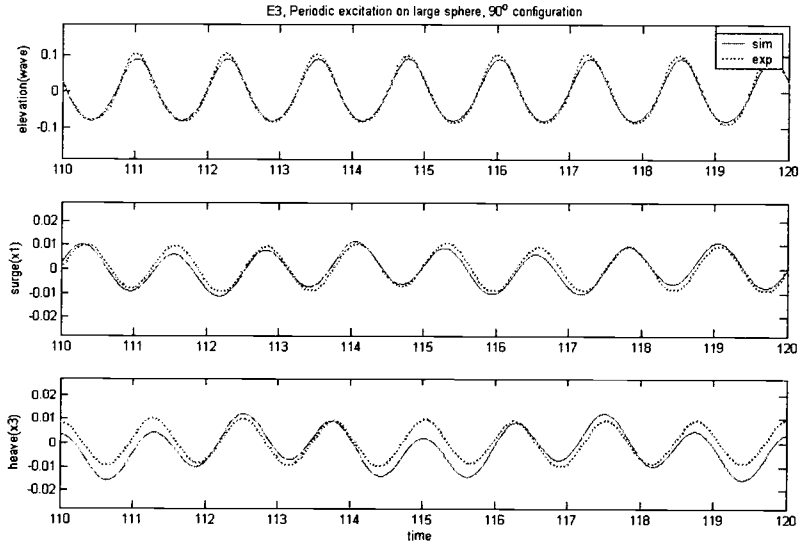

Fig.12 Time series of free surface elevation, surge and heave responses of moored structure (Test E3)

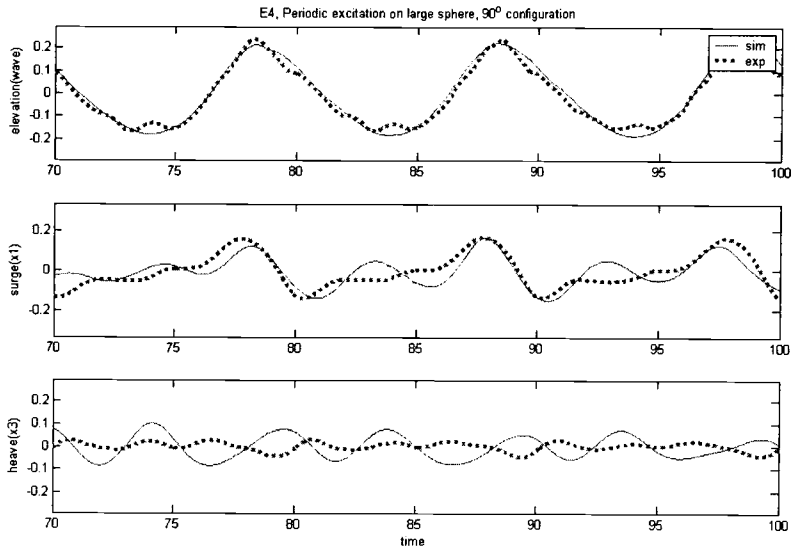

Fig.13 Time series of free surface elevation, surge and heave responses of moored structure (Test E4)

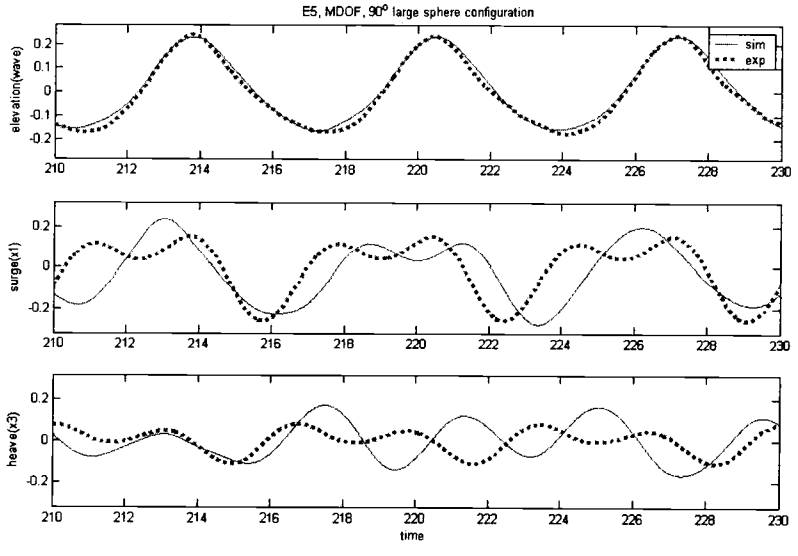

Fig.14 Time series of free surface elevation, surge and heave responses of moored structure (Test E5)

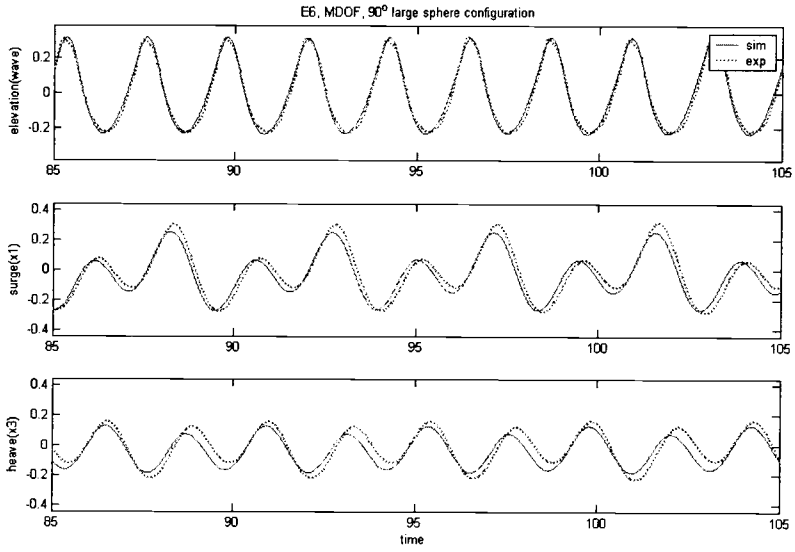

Fig.15 Time series of free surface elevation, surge and heave responses of moored structure (Test E6)

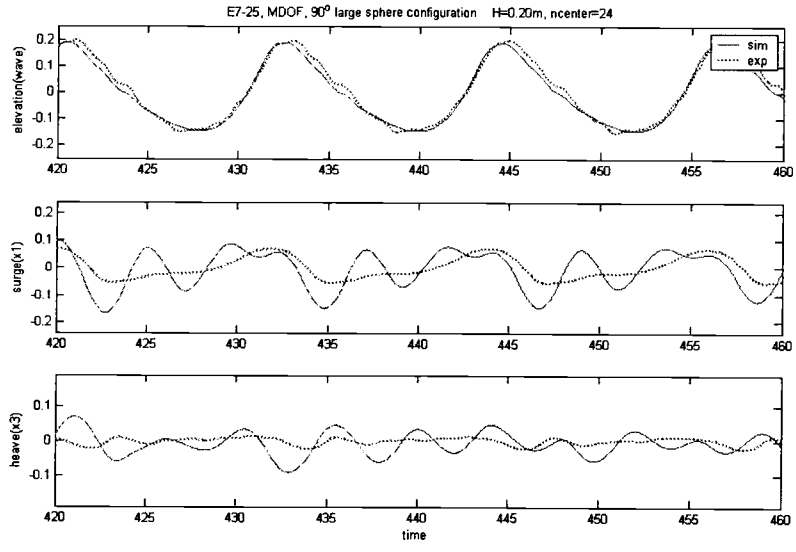

Fig.16 Time series of free surface elevation, surge and heave responses of moored structure (Test E7)

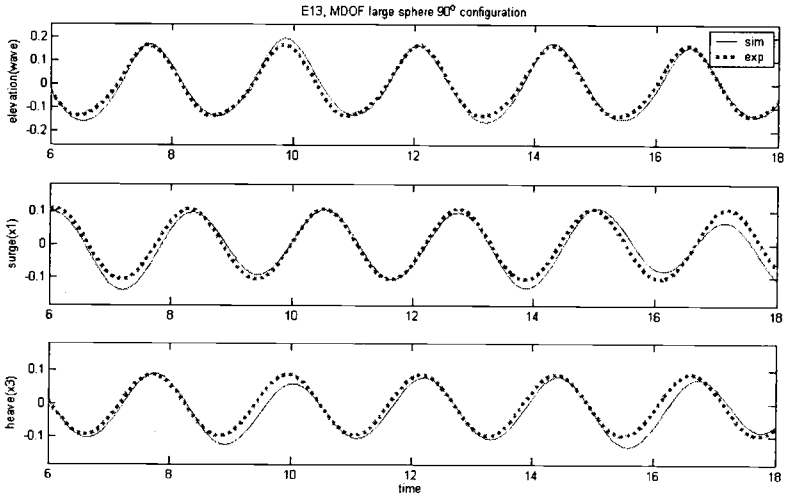

Fig.17 Time series of free surface elevation, surge and heave responses of moored structure (Test E13)

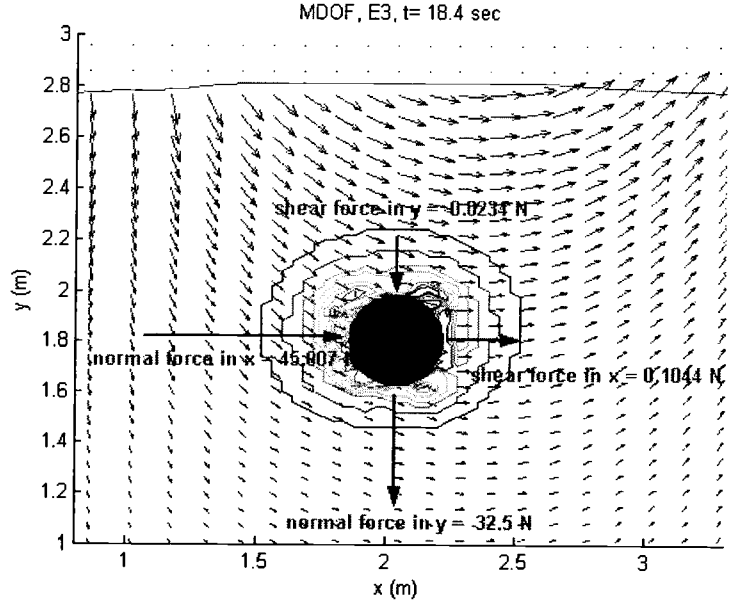

Fig.18 Snapshot of velocity field and turbulence intensity and normal/shear force components on rigid body at t=18.4 sec (Test E3)

Nomenclature

b	radius of equivalent 2D circle
c	damping coefficient
c_{cr}	critical damping coefficient
F_0	initial spring tension
f_{ext}	external excitation
f_s	restoring force from mooring lines
h	water depth
H	wave height
$[k]$	restoring force coefficient matrix
K	linear spring constant
L	wave length
m	structure mass
R	radius of sphere
sl	initial spring length
T	wave period
x_1	structure displacement in surge direction
ξ	structural damping ratio
ω	natural frequency of structural system, radian

CHAPTER 5

Numerical Modeling of Submerged and Aerial Drop of Rigid Body and Wave Generation

Yuk, D., Yim, S.C., Liu, P.L.-F., Panizzo, A. and Risio, M.

Abstract

Interactions of freely falling rigid body with fluid flow is examined in this paper. A two dimensional numerical model, based on Reynolds Averaged Navier Stokes equations, has been utilized to calculate the free surface deformation and the displacement of a rectangular shape rigid body in time domain. The k-ε closure model is employed to compute the turbulence associated with wave breaking. Numerical simulations with several different initial locations of rigid body have been performed and the influence of moving rigid body on incompressible Newtonian fluid flow is examined. As a solution method for complex fluid-structure interactions, an iterative procedure in which the displacement of moving rigid body is determined by balancing the hydrodynamic force and structural dynamic force is employed. Numerical results are compared with experimental data, which has been performed in a two-dimensional flume. Images of free surface profile and falling rigid body recorded from the laboratory tests by high speed camera are compared with numerical results. The velocity field, pressure distribution, and turbulence intensities in fluid are also predicted and presented in this paper. The capability and accuracy of present numerical model is verified and validated through the comparisons of numerical prediction with experimental data.

Introduction

Recently, significant progresses have been made in the field of numerical analysis of multi-physics problems with the aids of advanced computing technology. One of the inter-disciplinary problems with a wide range of application area is the fluid-structure interaction. Numerical tools for the analysis of fluid flow and structural mechanics have been developed separately using different mathematical approaches. Conventionally, Eulerian formulation is widely used to describe fluid flow because it is relatively easier to implement the conservation law of fluid. On the other hand, Lagrangian formulation has been a dominant approach in developments of numerical tools for structural dynamics because it is more convenient to describe the material surface displacement or the dynamic response of structural system. Recently mixed Eulerian-Lagrangian formulation has been used widely in developing numerical model for fluid-structure interaction.

In fluid-structure interaction problems, it is required to describe two physical phenomena with different characteristics, especially the "fully" coupled interactions between fluid flow and structure. By "fully" coupled interactions, it is referred that structural dynamic responses affect the fluid and vice versa.

In the previous study by Yuk *et al* (2004), the numerical model for fluid-structure interaction has been developed. In the model, the dynamics responses of structure are determined using Lagrangian approach and the fluid dynamics are modeled using Eulerian formulation. Exchanges of information between moving rigid body and fluid flow based on different formulations are made possible by introducing an iterative procedure with the partial cell technique. The iterative procedure is developed based on the dynamic equilibrium. The displacement of dynamic structure is determined in such a way that the equilibrium on the interface between fluid and rigid body can be satisfied simultaneously at each time steps.

The numerical model developed previously is applied to predict the aerial and submerged drop of rigid body and generation/propagation of waves due to the rigid body motion. To demonstrate the accuracy and capability, comparisons of numerical results with experimental data will be presented. Observations and interpretations of numerical results will be discussed.

Model Description

The mean flow field are solved using Reynolds Averaged Navier Stokes (RANS) equations which is given as

$$\frac{\partial \langle u_i \rangle}{\partial x_i} = 0 \tag{1}$$

$$\frac{\partial \langle u_i \rangle}{\partial t} + \langle u_j \rangle \frac{\partial \langle u_i \rangle}{\partial x_j} = -\frac{1}{\langle \rho \rangle}\frac{\partial \langle p \rangle}{\partial x_i} + g_i + \frac{1}{\langle \rho \rangle}\frac{\partial \langle \tau_{ij}^m \rangle}{\partial x_j} - \frac{\partial \langle u_i' u_j' \rangle}{\partial x_j} + \frac{1}{\langle \rho \rangle^2}\left\langle \rho' \frac{\partial p'}{\partial x_i} \right\rangle - \frac{1}{\langle \rho \rangle^2}\left\langle \rho' \frac{\partial \tau_{ij}^{m'}}{\partial x_j} \right\rangle \tag{2}$$

where subscripts i, j denote the Cartesian component taking 1, 2 for two dimensional flows and $\langle\ \rangle$ the ensemble average of different solutions of the Navier-Stokes equations (NSE). In equations (1) and (2), u_i denotes the i-th component of the velocity vector, ρ the density of fluid, p the pressure, g_i the i-th component of the gravitational acceleration, and τ_{ij}^m the molecular viscous stress tensor. Under the Newtonian fluid assumption, τ_{ij}^m can be expressed by $\tau_{ij}^m = 2\mu\sigma_{ij}$ with μ being the dynamic viscosity (whose unit is kg m^{-1} s^{-1}) and $\sigma_{ij} = \frac{1}{2}\left(\frac{\partial u_i}{\partial x_j} + \frac{\partial u_j}{\partial x_i}\right)$ the strain rate tensor.

In the fifth term of the right hand side of equation (2), there is a correlation between density fluctuations and the gradient of pressure fluctuations. The correlation between density fluctuations and the gradient of viscous stress fluctuations are also included in the sixth term of right hand side of equation (2). However, since these correlations are not clearly known up to today and the constant density within the fluid is assumed, the last two terms in

equation (2) are neglected in this study. The only additional term when compared to general NSE is the fourth term of the right hand side of equation (2), i.e., $\frac{\partial\langle u_i u_j\rangle}{\partial x_j}$. The ensemble average of product of two different velocity fluctuation components in that term is used for the definition of Reynolds stress tensor. The Reynolds stress tensor is defined as

$$R_{ij} = -\langle\rho\rangle\langle u_i' u_j'\rangle \tag{3}$$

In previous research work, many second-order turbulence closure models have been developed for different applications. In this study, the so-called k-ε model where the Reynolds stress is approximated by nonlinear algebraic stress model is employed as the turbulence closure model (Shih *et al.*, 1996).

$$\begin{aligned}\rho\langle u_i' u_j'\rangle = {} & \frac{2}{3}\rho k\delta_{ij} - C_d\frac{k^2}{\varepsilon}\left(\frac{\partial\langle u_i\rangle}{\partial x_j}+\frac{\partial\langle u_j\rangle}{\partial x_i}\right) \\ & -\rho\frac{k^3}{\varepsilon^2}\left[\begin{array}{l} C_1\left(\frac{\partial\langle u_i\rangle}{\partial x_l}\frac{\partial\langle u_l\rangle}{\partial x_j}+\frac{\partial\langle u_j\rangle}{\partial x_l}\frac{\partial\langle u_l\rangle}{\partial x_i}-\frac{2}{3}\frac{\partial\langle u_l\rangle}{\partial x_k}\frac{\partial\langle u_k\rangle}{\partial x_l}\delta_{ij}\right) \\ +C_2\left(\frac{\partial\langle u_i\rangle}{\partial x_k}\frac{\partial\langle u_j\rangle}{\partial x_k}-\frac{1}{3}\frac{\partial\langle u_l\rangle}{\partial x_k}\frac{\partial\langle u_l\rangle}{\partial x_k}\delta_{ij}\right) \\ +C_3\left(\frac{\partial\langle u_k\rangle}{\partial x_i}\frac{\partial\langle u_k\rangle}{\partial x_j}-\frac{1}{3}\frac{\partial\langle u_l\rangle}{\partial x_k}\frac{\partial\langle u_l\rangle}{\partial x_k}\delta_{ij}\right)\end{array}\right]\end{aligned} \tag{4}$$

where C_1, C_2 and C_3 are empirical coefficients, δ_{ij} Kronecker delta, $k = \frac{1}{2}\langle u_i' u_i'\rangle$ the turbulence kinetic energy and $\varepsilon = \nu\left\langle\left(\partial u_i'/\partial x_k\right)^2\right\rangle$ the

dissipation rate of turbulence kinetic energy with $\nu = \mu/\rho$ the kinematic viscosity. When compared with the classical closure model which is called linear isotropic eddy viscosity model, equation (4) returns to classical model with C_1=C_2=C_3=0 as shown below.

$$\langle u_i' u_j' \rangle = -2\nu_t \langle \sigma_{ij} \rangle + \frac{2}{3} k \delta_{ij} \tag{5}$$

where $\nu_t = C_d \frac{k^2}{\varepsilon}$ is the eddy viscosity and C_d is another empirical coefficient. The weakness of the linear isotropic eddy viscosity model is that equation (5) may not accurately represent the physics of anisotropic turbulence in complex turbulent flows. However, the turbulence closure model given in equation (4) can be applied to general anisotropic turbulent flows. The governing equation for k and ε (Rodi, 1980) are modeled as

$$\frac{\partial k}{\partial t} + \langle u_j \rangle \frac{\partial k}{\partial x_j} = \frac{\partial}{\partial x_j}\left[\left(\frac{\nu_t}{\sigma_k} + \nu\right)\frac{\partial k}{\partial x_j}\right] - \langle u_i' u_j' \rangle \frac{\partial \langle u_i \rangle}{\partial x_j} - \varepsilon \tag{6}$$

$$\begin{aligned} \frac{\partial \varepsilon}{\partial t} + \langle u_j \rangle \frac{\partial \varepsilon}{\partial x_j} &= \frac{\partial}{\partial x_j}\left[\left(\frac{\nu_t}{\sigma_\varepsilon} + \nu\right)\frac{\partial \varepsilon}{\partial x_j}\right] \\ &\quad + C_{1\varepsilon}\frac{\varepsilon}{k}\nu_t\left(\frac{\partial \langle u_i \rangle}{\partial x_j} + \frac{\partial \langle u_j \rangle}{\partial x}\right)\frac{\partial \langle u_i \rangle}{\partial x_j} - C_{2\varepsilon}\frac{\varepsilon^2}{k} \end{aligned} \tag{7}$$

where $\sigma_k, \sigma_\tau, C_{1\varepsilon}$ and $C_{2\varepsilon}$ are empirical coefficients. The coefficients in equations (4), (6) and (7) have been determined by performing many simple experiments and enforcing the physical realizability; the values for these

coefficients suggested by Lin and Liu (1998) and used in this study are C_1=0.0054, C_2=-0.0171, C_3=0.0027, C_1=1.44, $C_{2\varepsilon}$=1.9, σ_ε=1.3 and σ_k=1.0.

Applying appropriate boundary conditions, and approximating the derivatives in Navier-Stokes equations using a finite-difference scheme with a combination of backward and forward difference methods, numerical solution of Navier-Stokes equations are obtained. Detailed descriptions of assumptions for the turbulence closure model and the boundary conditions imposed on the computational domain boundaries and internal rigid-body boundaries can be found in a previous study by Lin (1998).

Experimental Setup

21 Experiments are done at LIAM laboratory, L'Aquila University, Italy by Panizzo and Marcello with various configurations as shown in Table 1. Among 21 tests, 3 representative cases will be presented in this paper and the results of the rest can be found in the Appendix B of Yuk's Ph.D dissertation (2004).

A box is placed in a two-dimensional flume of 12 m length, 0.45 m depth and 0.3 m width. The box of 0.3 m width is placed in the flume and the space between box and vertical wall of flume is less than 1 mm. The specific weight of box is 1.33 ton/m^3. The lengths of rectangular rigid body are varied

from 0.05 m, 0.1 m and 0.15 m, while the width and height of 0.1 m are not changed.

Table 1 Experiments configurations

Initial box location	Box length	Water depth	Test
+ 3 cm	5 cm	6 cm	L5H6P3
		10 cm	L5H10P3
	10 cm	6 cm	L10H6P3
		10 cm	L10H10P3
		18 cm	L10H18P3
		23 cm	L10H23P3
	15 cm	6 cm	L15H6P3
- 3 cm	5 cm	6 cm	L5H6M3
	10 cm	6 cm	L10H6M3
		10 cm	L10H10M3
		18 cm	L10H18M3
		23 cm	L10H23M3
	15 cm	6 cm	L15H6M3

Initial box location	Box length	Water depth	Test
0 cm	5 cm	6 cm	L5H6PM0
		10 cm	L5H10PM0
		18 cm	L5H18PM0
	10 cm	6 cm	L10H6PM0
		10 cm	L10H10PM0
		18 cm	L10H18PM0
		23 cm	L10H23PM0
	15 cm	6 cm	L15H6PM0

The box is initially located partially submerged 3 cm below the still water level, on still water lever and 3 cm above still water level, respectively. Water depth is also varied from 6 cm, 10 cm, 18 cm, and 23 cm. Five wave gauges are installed along the flume to measure the free surface elevation and digital video camera (Canon XM1) with resolution of 25 frames/sec is also used to record the wave profile in generation region. The profile view and plane view of the two-dimensional flume and locations of wave gauges are shown in Figure 1.

Numerical Modeling

The freefalling rigid body and wave generation/propagation is modeled in two-dimensional vertical plane. The computational domain of 1.4m × 0.4 m is discretized with uniform grid size of 0.5 cm in horizontal direction and 0.25 cm in vertical direction. The rectangular shape rigid body is placed at the left end of the domain and free-slip boundary conditions are applied on all the boundaries except the right end of computational domain. The radiation boundary condition is imposed on the right end of domain to ensure continuous outflow through the boundary.

In the numerical modeling, it is assumed that there is no space between moving rigid boundary and the left boundary of computational domain and the motion of falling body is always in perfectly vertical direction without rotation. Frictional forces acting on the surface of that box that is in contact with the vertical wall of the flume is assumed to be proportional to the contact area of wall. i.e. larger frictional forces are used for the box with a larger dimension.

In computing wave force on rigid body, shear stress which is applied in tangential direction to moving boundary is assumed to negligible. Thus only normal forces obtained by integrating pressures along the moving boundaries are considered in this study. More detailed discussions will be presented in concluding remarks.

Although experiments are done in a two-dimensional flume, the box and flume have width of 0.3 m. In numerical model, the width in z-direction is assumed to be unit length which is 1 m in this case. To take this three-dimensional width into account, the hydrodynamic force which is obtained by integrating pressure along the moving rigid body is multiplied by 0.3 which is the ratio of the width of flume to theoretical domain width, i.e., 0.3 m / 1.0 m.

In the first representative case which is referred to L10H10M3, the box with dimension of 0.1 m × 0.3 m × 0.1 m (length×width×height) is located initially 3 cm below the still water level (SWL) and released into the 0.1 m deep water. The time history of box displacement computed based on the dynamic equilibrium by using iterative procedure is compared with experimental data in Figure 3. In the snapshot of Figure 3, the rigid body boundaries and the free surfaces in thick solid lines, which are obtained from the numerical model, is scaled and overlapped on the experimental images for direct comparisons. The Snapshot of rigid body and free surface at t=+0.32 sec in Figure 3 shows that the predicted location of rigid body and free surface profile are in good agreements with experimental data. Notice that the displacement of moving body in numerical simulation does not reach the bottom boundary. In numerical modeling, the rigid body movement is limited and controlled not to drop below the computational cell height above the

bottom boundary due to the instability and limitation of the present numerical model. The instability and limitation will be discussed later in this paper.

While the rigid body is falling, the higher pressure is observed at the bottom left corner of flume and flow separation occurs at the bottom right corner of moving body as shown in the first plots of Figure 5 and 6. In the first plot of Figure 7, the vortex generation in the front of moving body is shown. After rigid body rests on the bottom, the vortex, which is rotating counterclockwise, is detached from the front face of rigid body and propagates in the positive x direction as shown in Figure 7. It is also observed that the pressure near the vortex center is less than hydrostatic pressure. The maximum wave height recorded at x = 0.4 m shows good agreement with experimental data. However, a phase difference is observed. The phase lag is considered to be caused by the different reference time used in the experiment measurement.

In the second case (L10H10P3), the box size and water depth are the same as in the previous case with different initial location of the box, which is 3 cm above SWL. The movement of rigid body and a wave with nonlinear free surfaces at t=+0.32 sec are predicted accurately and the cavitations near the front face of the rigid body clearly shown in the snapshot of Figure 8. Good agreements of rigid body displacement and free surface elevation time histories recorded at x = 0.4m and 0.8m with experiment measurements are observed as shown in Figures 8 and 9. As shown in Figures 10 to 12, the influence of

moving rigid body on fluid is much stronger than in the test with submerged initial location. The free surface in front face of the moving body is separated due to the impact and turbulence with maximum intensity of 0.04 m/s is observed along the steep free surface as shown in the first plot of Figure 12. Higher pressures near bottom left corner of the flume is observed as in the previous test. The maximum pressure and turbulence intensity obtained in this case was higher than the initially submerged box drop test as anticipated. Good agreements of rigid body displacement and free surface elevation time histories recorded at x = 0.4m and 0.8m with experiment measurements are observed as shown in Figures 8 and 9.

In the last case (L10H18P3), the same size of box is initially located 3 cm above the SWL and is released to 0.18 m deep water. The snapshot in Figure 13 shows the location of moving rigid boundaries and the nonlinear wave generation due to the rigid body motions at t=+0.32 sec. The numerical results are in good agreements with experimental data. Up to the point where the moving rigid body is completely submerged, the velocity, pressure and turbulence fields show similar behavior as in the second case. However, it is noticed that the negative wave propagates toward the left end of flume and reflected. As a result, the vortex near the front face of rigid body is not detached and intense turbulence is generated in the region above the rigid body by the reflected wave. Disagreements are noticed in comparisons of free

surface elevation time series after t≈1.5 seconds as shown in Figure 14. It is noticed that the random nature of the splashed water particles and three-dimensional air bubbles observed in laboratory tests might cause those disagreements.

Concluding Remarks

In general, numerical results are in good agreement with experimental data as shown in displacement time history and free surface elevation time series comparisons. The capability and accuracy of the numerical model is verified and validated through the comparisons with various experimental data including submerged and aerial drop of rigid body.

To validate the assumption that shear stress from fluid flow is negligible, shear stress and normal stress are computed using pressure field, turbulence intensity and velocity field of fluid in Test L10H18P3 at t = 0.4 seconds. Tangential forces on top, front and bottom face of moving rigid body are 0.21%, 0.71% and 0.25% of corresponding normal forces as shown in Figure 18. Thus it is concluded that the shear stress is negligible in rigid body drop tests examined in this study.

It is noticed that numerical instability occurs as the moving rigid boundary approaches to the bottom boundary of computational domain. When

the distance from moving boundary and bottom boundary is less than one vertical grid size, the solution of Poisson Pressure equation did not converged after predetermined iteration limit. This instability might be attributed to the limited capability of general finite difference scheme in resolution issue and partial cell treatment since it is impossible to define two different rigid boundaries in one cell by the nature of finite difference scheme.

Acknowledgements

Partial support from the National Science Foundation Grants CMS-9908392 and CMS-0217744, and the US Office of Naval Research Grants N00014-92-1221 and N00014-04-10008 are gratefully acknowledged.

References

Cheng, Franklin Y. 2001. Matrix Analysis of Structural Dynamics. Marcel Dekker.

Lin, P. 1998. Numerical modeling of breaking waves. Ph.D. Thesis. Cornell University.

Rodi, W. 1980 Turbulence models and their application in hydraulics – A state-of-the-art review. I.A.H.R. publication.

Shih, T.H., Zhu, J., and Lumley, J.L. 1996 Calculation of wall-bounded complex flows and free shear flows. *International J. for Numerical Methods in Fluids*, 23, 1133-1144

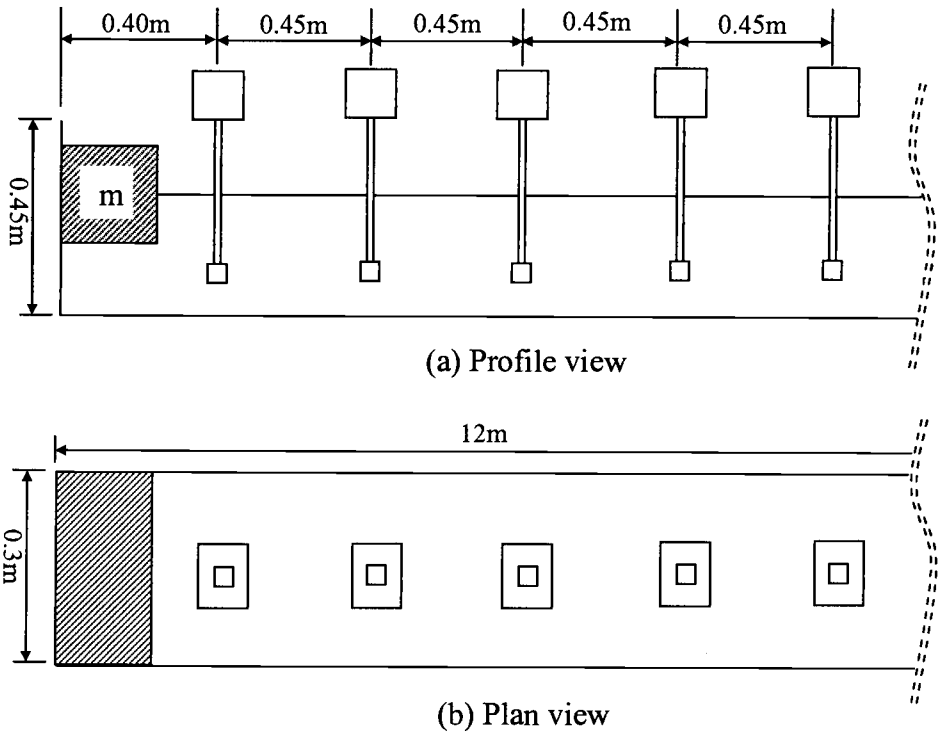

Fig 1. Locations of wave gauges and 2 dimensional flume

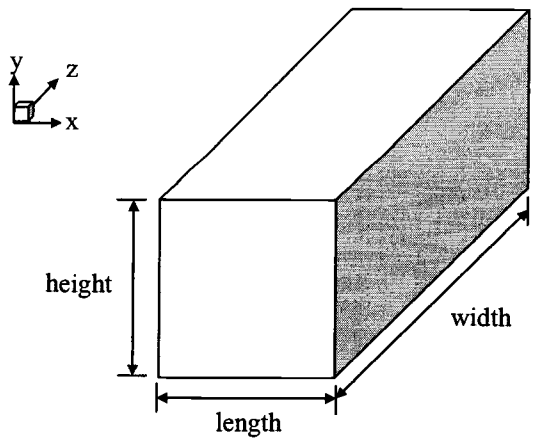

Fig 2. Definition of length, width, and height of rigid body

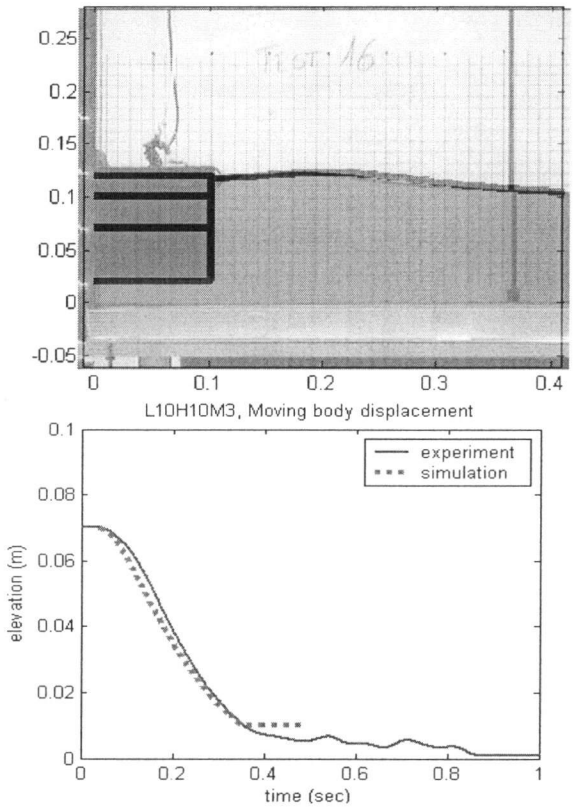

Fig 3. Snapshot of rigid body drop with free surface at t=+0.32 sec and displacement time history of moving rigid body (Test L10H10M3)

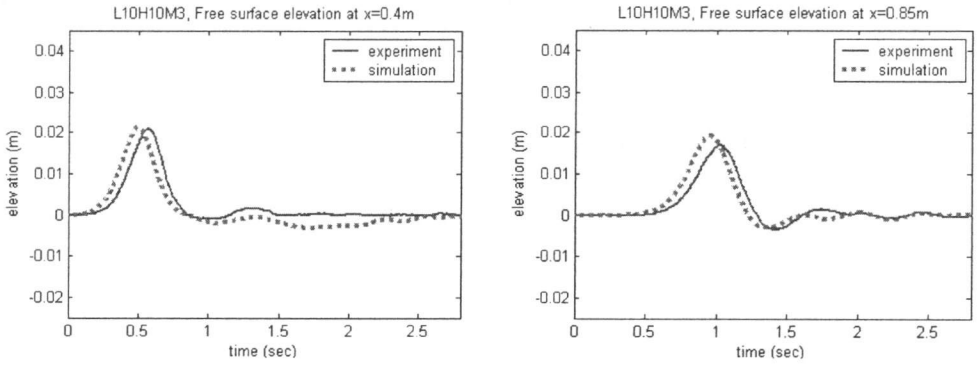

Fig 4. Time series of free surface elevation at x=0.4m and 0.85m (Test L10H10M3)

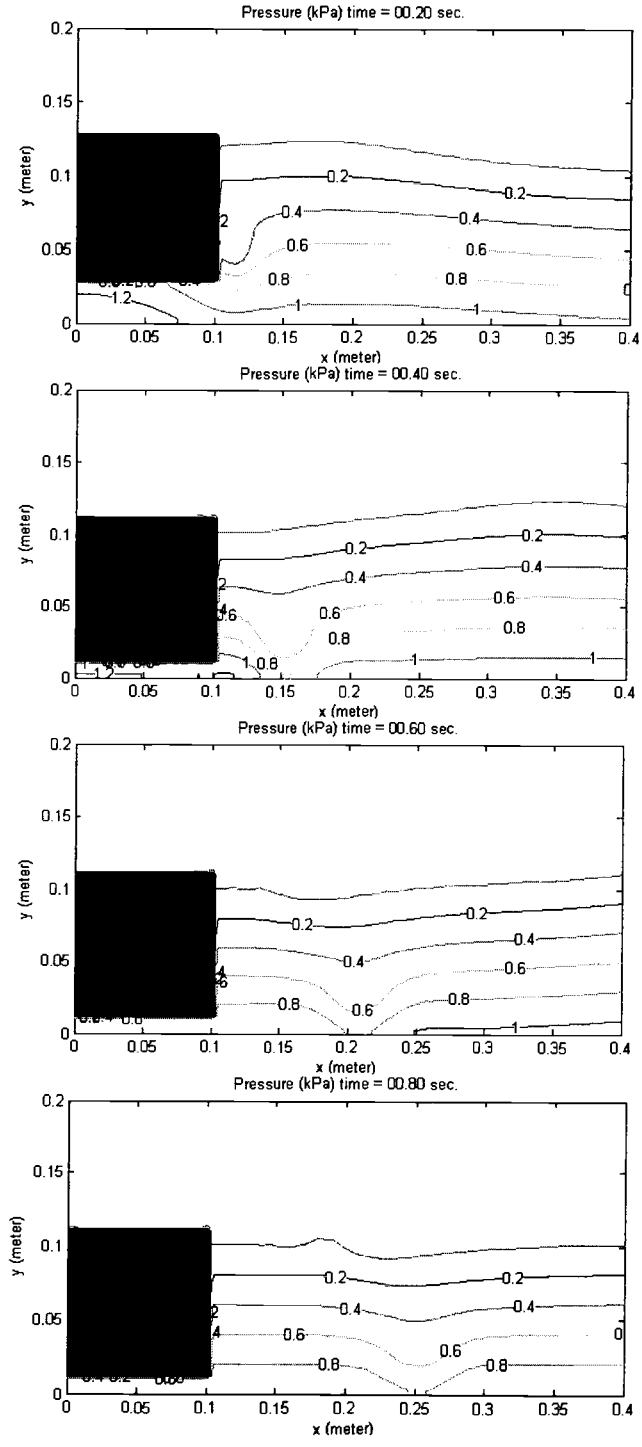

Fig 5. Contour plot of pressure field computed by numerical model at t=0.2, 0.4, 0.6, and 0.8 seconds (Test L10H10M3)

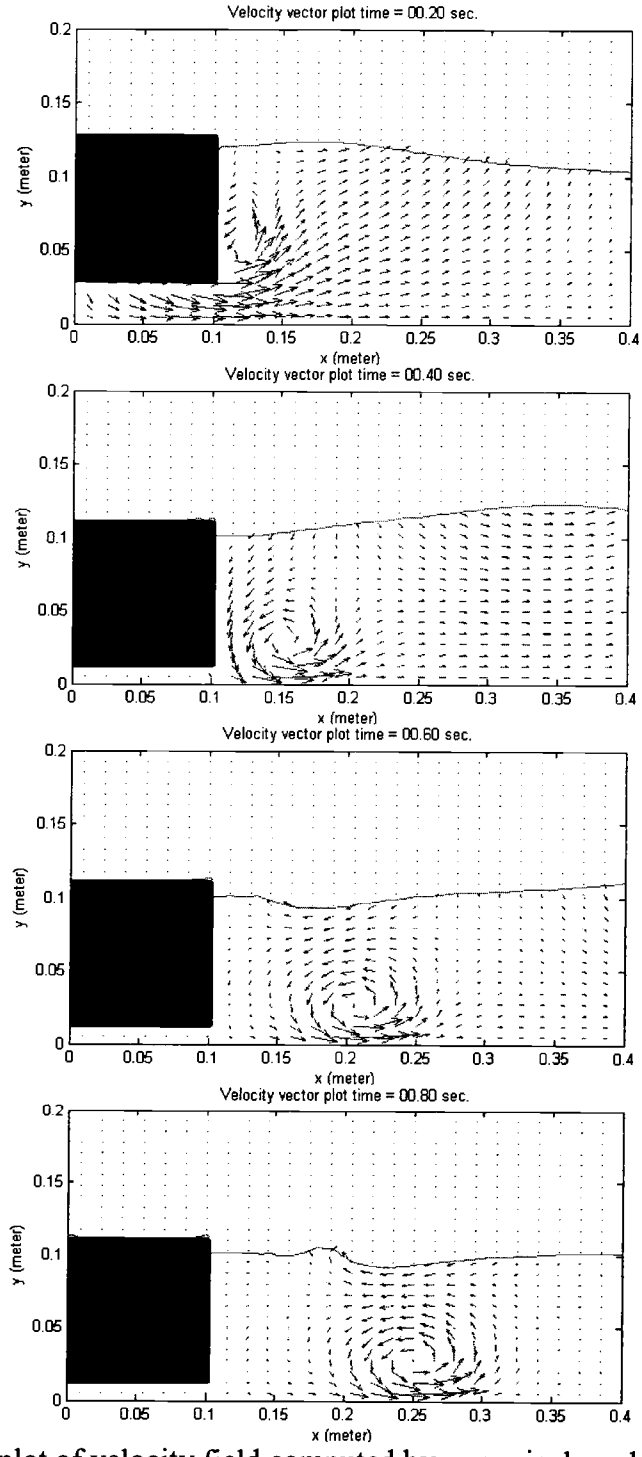

Fig 6. Vector plot of velocity field computed by numerical model at t=0.2, 0.4, 0.6, and 0.8 seconds (Test L10H10M3)

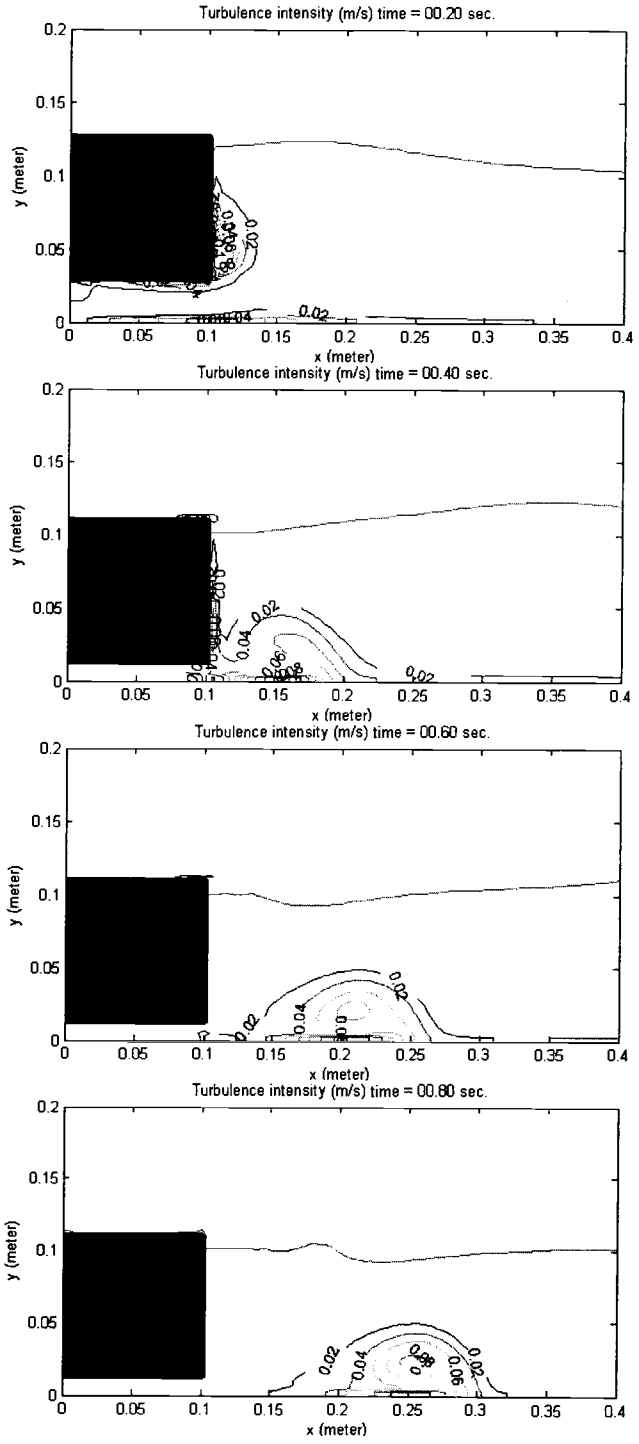

Fig 7. Turbulence intensity (m/s) computed by numerical model at t=0.2, 0.4, 0.6, and 0.8 seconds (Test L10H10M3)

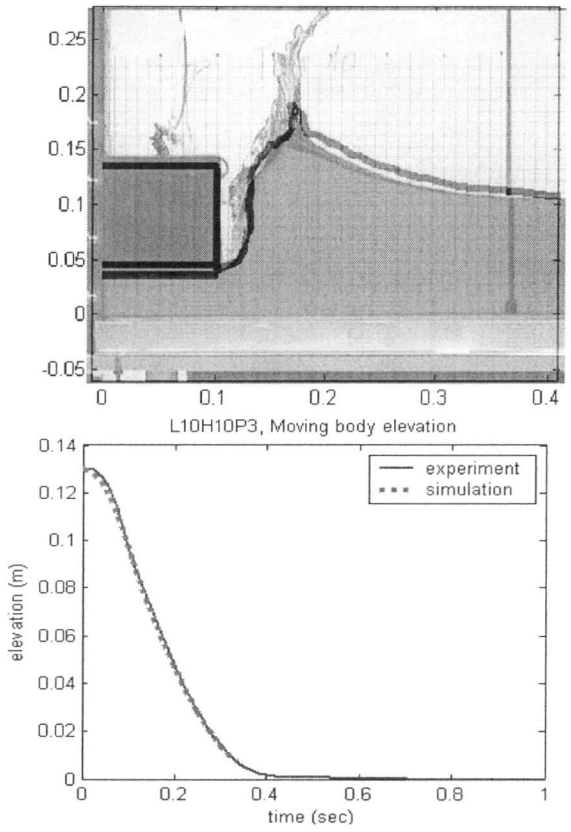

Fig 8. Snapshot of rigid body drop with free surface at t=+0.32 sec and displacement time history of moving rigid body (Test L10H10P3)

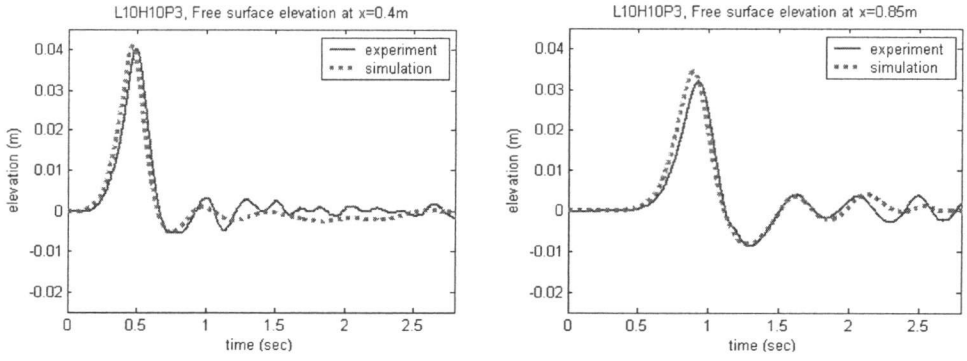

Fig 9. Time series of free surface elevation at x=0.4m and 0.85m (Test L10H10P3)

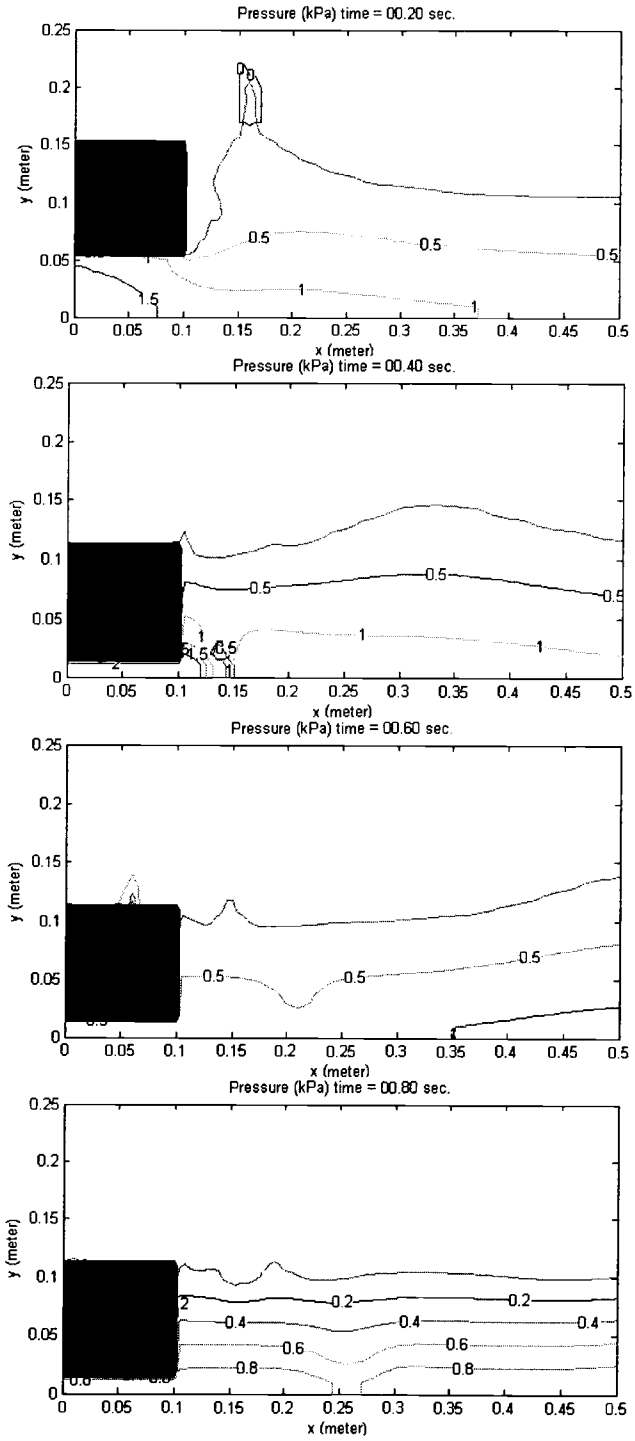

Fig 10. Contour plot of pressure field computed by numerical model at t=0.2, 0.4, 0.6, and 0.8 seconds (Test L10H10P3)

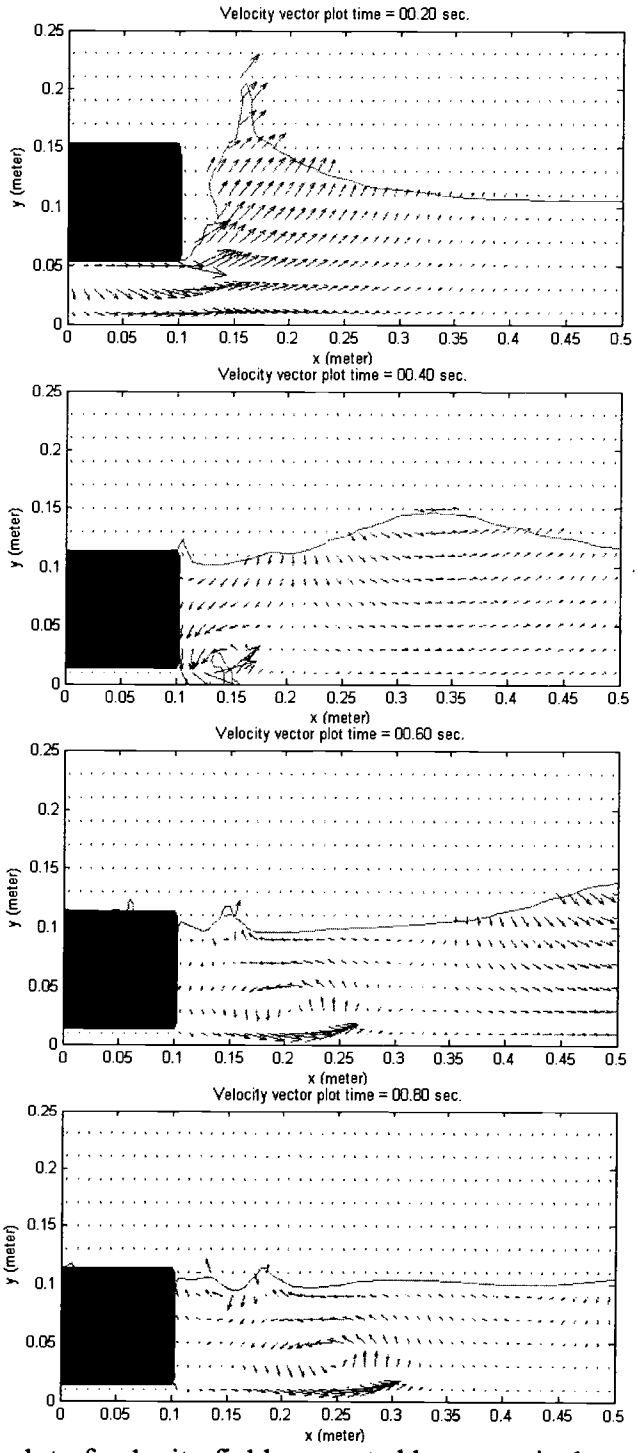

Fig 11. Vector plot of velocity field computed by numerical model at t=0.2, 0.4, 0.6, and 0.8 seconds (Test L10H10P3)

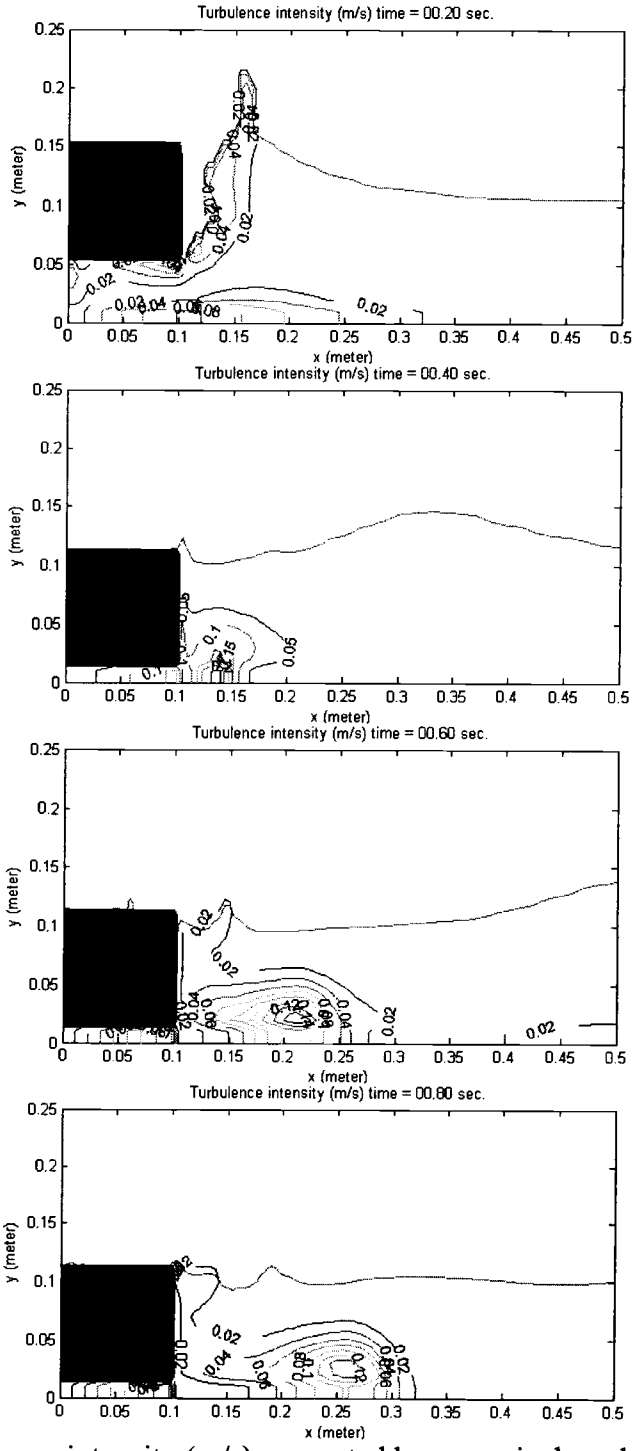

Fig 12. Turbulence intensity (m/s) computed by numerical model at t=0.2, 0.4, 0.6, and 0.8 seconds (Test L10H10P3)

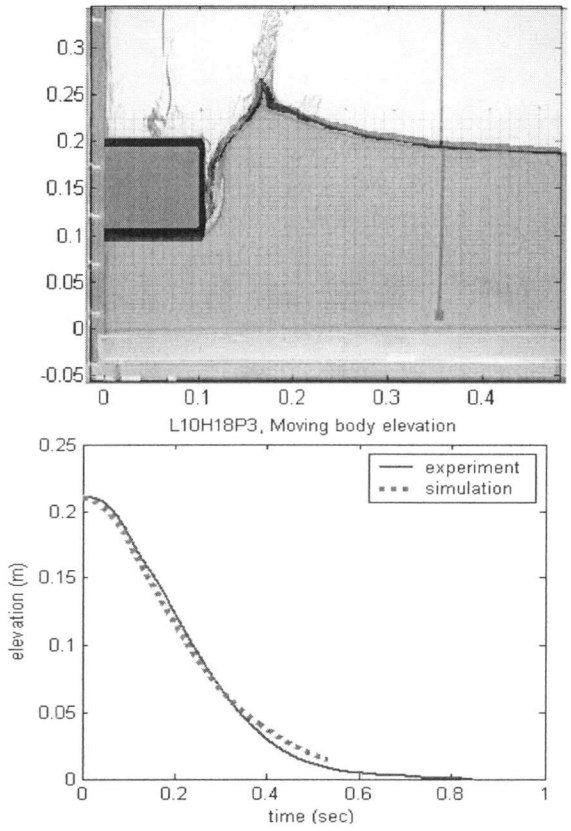

Fig 13. Snapshot of rigid body drop with free surface at t=+0.32 sec and displacement time history of moving rigid body (Test L10H18P3)

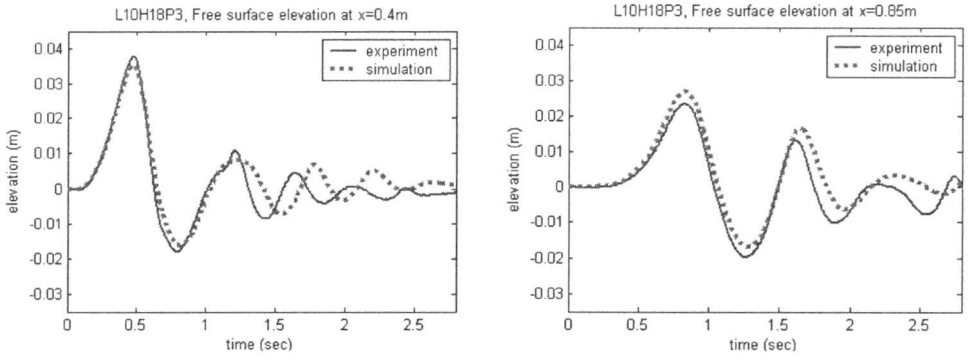

Fig 14. Time series of free surface elevation at x=0.4m and 0.85m (Test L10H18P3)

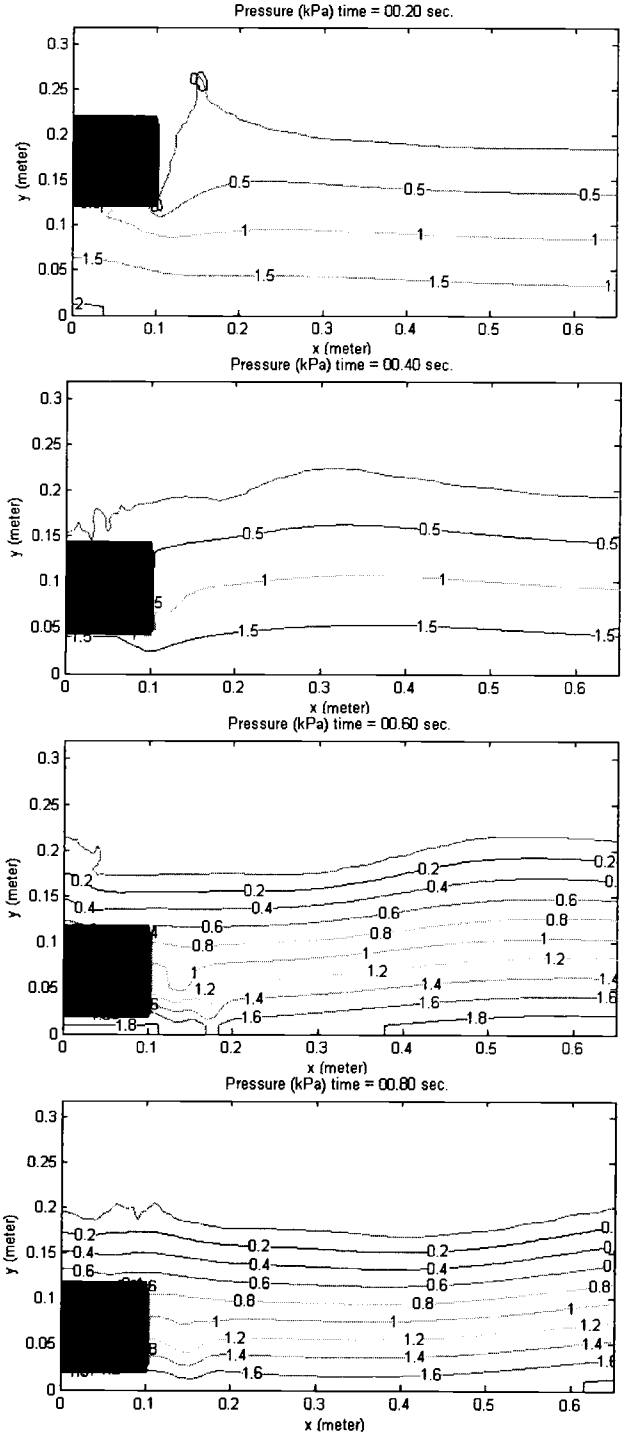

Fig 15. Contour plot of pressure field computed by numerical model at t=0.2, 0.4, 0.6, and 0.8 seconds (Test L10H18P3)

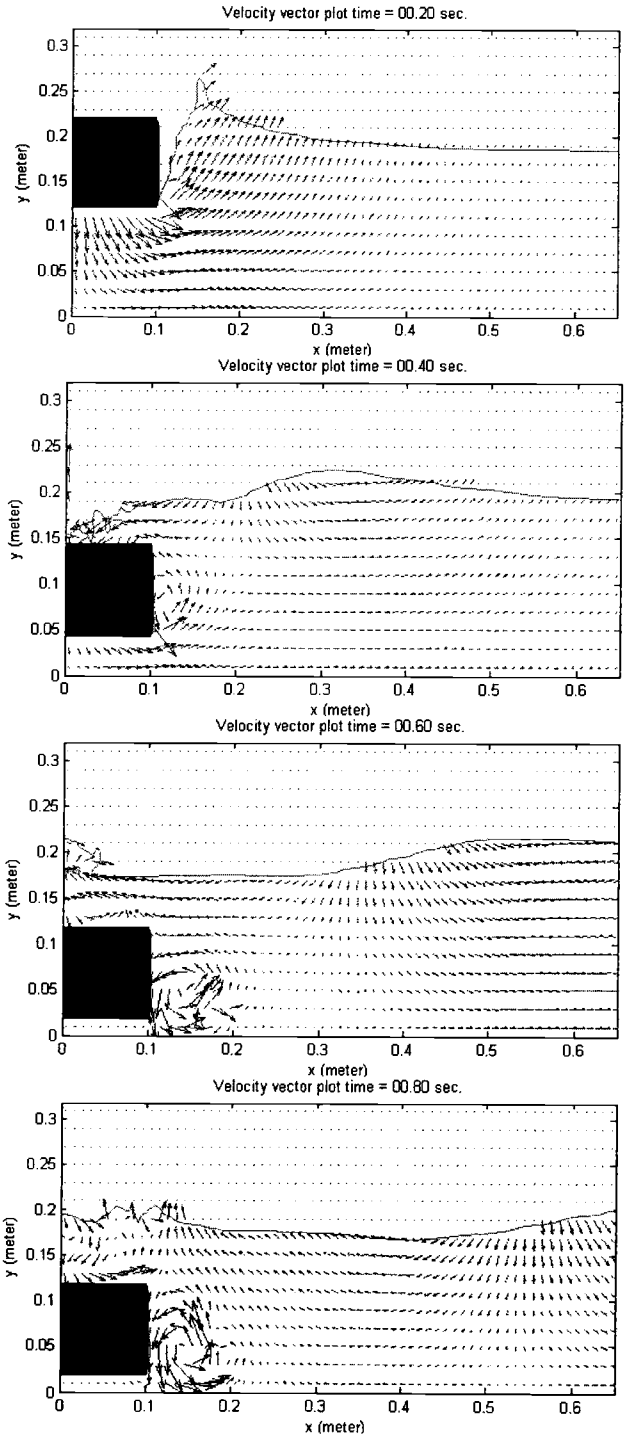

Fig 16. Vector plot of velocity field computed by numerical model at t=0.2, 0.4, 0.6, and 0.8 seconds (Test L10H18P3)

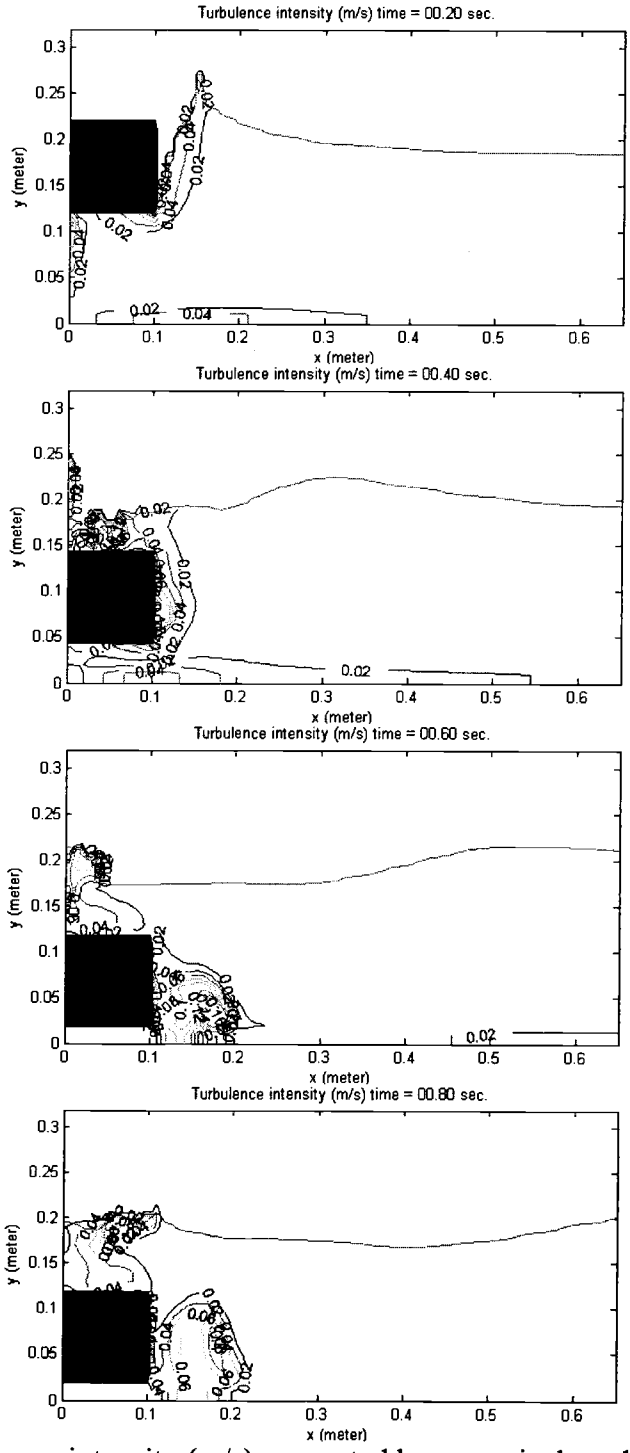

Fig 17. Turbulence intensity (m/s) computed by numerical model at t=0.2, 0.4, 0.6, and 0.8 seconds (Test L10H18P3)

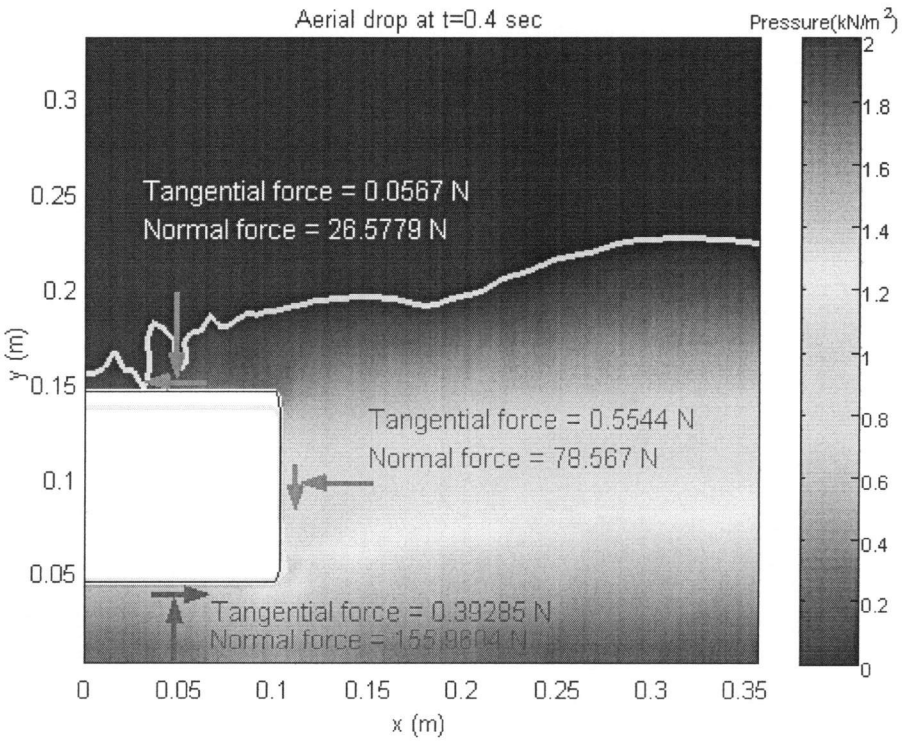

Fig 18. Tangential and normal force on moving boundaries and pressure field at t=0.4 seconds (Test L10H18P3)

CHAPTER 6

Concluding Remarks

A numerical model for fully-coupled interactions of incompressible fluid with a non-stationary rigid structure is developed in this thesis using modified continuity equations. Dynamic equilibrium between the structure and the fluid is satisfied at each time step through the iterative procedure developed in the previous chapters. Comparisons of numerical results with various experimental data are performed to verify and validate the accuracy, applicability and capability of the numerical model in predicting the hydrodynamic and structural dynamic behaviors. Good agreements are observed in the comparisons and the current model is verified and validated.

The free surface of plunging waves generated by a sliding rigid body on the slope is predicted accurately by the current model. It is often difficult to measure the exact free surface elevation of breaking wave because of the multiple values of free surface elevation. The numerical model can be used to

estimate or predict the free surface elevation of plunging waves.

Utilizing the numerical model developed in this study, the functional relationships between the maximum runup/rundown and the specific density, the initial submergence level, the angle of the moving mass, and the slope angle are identified. The maximum runup and rundown formulae derived based on the numerical results provide useful information for tsunami mitigations.

The capability of the present model to predict accurately the dynamic response of a nonlinear structural system as well as nonlinear waves is shown in the comparisons of numerical results with data from the experimental moored structure tests. Characteristic behaviors of the nonlinear structural system are successfully identified.

Although a great deal of advances have been accomplished in computing technologies, the numerical modeling of fluid-structure interaction using RANS equations demands high computing power. The iterative procedure presented in this study for dynamic equilibrium requires 3 to 5 times more computation time on average when compared with the corresponding

numerical modeling without the iterative procedure. Supercomputer and parallel processing are recommended for future use of the present numerical model.

Recommended Future Study

Depending on the structural properties such as Young's modulus, aspect ratio or external excitation conditions, structural systems of interest might need to be considered as flexible bodies. A numerical model for a flexible structure interacting with fluid flow will provide a wider range of application, as well as the basis for a better understanding of the physics associated with fluid-structure interaction.

Two dimensional (vertical plane) models have a limitation in describing motions in a horizontal plane for both the structure and the flow field. In general, structural systems are three dimensional and often not symmetric with respect to the vertical plane. Three dimensional models will be very useful

tools to examine the influence of asymmetric structures on the flow field and vice versa.

BIBLIOGRAPHY

Chang, K. 1999. Experimental study of wave breaking and wave-structure interaction. Ph.D. Thesis. Cornell University.

Chen, S., Johnson, D.B. and Raad, P.E. 1995. Velocity boundary conditions for the simulation of free surface fluid flow. *J. Comp. Phys.*, 116, 262-276.

Chorin, A.J. 1968. Numerical solution of the Navier-Stokes equations. *Math. Comp.*, 22, 745-762.

Chorin, A.J. 1969. On the convergence of discrete approximations of the Navier-Stokes equations. *Math. Comp.*, 23, 341-353.

Dean, R.G. and Dalrymple, R.A. 1984. Water wave mechanics for engineers and scientists. Prentice Hall.

Enet, F., Grilli, S.T. and Watts, P. 2003. Laboratory experiments for tsunamis generated underwater landslides: Comparison with numerical modeling. *Proc. Thirteenth Int. Offshore and Polar Engr. Conf.*, 372-379.

Grilli, S.T. and Watts, P. 1999 Modeling of waves generated by a moving submerged body. Applications to underwater landslides. *Eng. Anal. Boundary Elements*, 23, 645-656.

Hammack, J.L. 1973. A note on tsunamis: their generation and propagation in an ocean of uniform depth. *J. Fluid Mech.*, 60, 769-799.

Heinrich, P. 1991. Nonlinear numerical model of landslide-generated water waves. *Int.J. Engr. Fluid Mech.*, 4(4), 403-416.

Heinrich, P. 1992. Nonlinear water waves generated by submarine and aerial landslides. *J. Waterway, Port, Coastal and Ocean Engr.*, ASCE, 118, 249-266.

Hirt, C.W. and Nichols, B.D. 1981. Volume of fluid (VOF) method for the dynamics of free boundaries. *J. Comp. Phys.*, 39, 201-225.

Hsu, T. 1999. A numerical study of wave-structure interaction using Reynolds Averaged Navier-Stokes equations with k-ε turbulence closure model. MS Thesis. Cornell University.

Hsu, T.-J., Sakakiyama, T. and Liu, P.L.-F. 2002. Validation of a model for wave-structure interactions. *Coastal Engr.*, 46, 25-50.

Kershaw, D.S. 1978. The incomplete Cholesky-Conjugate gradient method for the iterative solution of systems of linear equations. *J. of Comp. Phys.*, 26, 43-65.

Kothe, D.B., Mjolsness, R.C. and Torrey, M.D. 1991. Ripple: A computer program for incompressible flows with free surfaces. Rep. LA-12007-MS. Los Alamos National Laboratory.

Lin, P. 1998. Numerical modeling of breaking waves. Ph.D. Thesis. Cornell University.

Lin, P. and Liu, P.L.-F. 1998a A numerical study of breaking waves in the surf zone. *J. Fluid Mech.*, 359, 239-264.

Lin, P. and Liu, P.L.-F. 1998b Turbulence transport, vorticity dynamics, and solute mixing under plunging breaking waves in surf zone. *J. Geophys. Res.*, 103, 15677-15694.

Lin, P., and Liu, P.L.-F. 1999 Internal wave-maker for Navier-Stokes equation models. *J. Waterway, Port, Coastal and Ocean Engr.*, ASCE, 125 (4), 207-215.

Lin, P., Chang, K.-A., and Liu, P.L.-F. 1999 Runup and rundown of solitary waves on sloping beaches. *J. Waterway, Port, Coastal and Ocean Engr.*, ASCE, 125 (5), 247-255.

Liu, P.L.F. and Lin, P. 1997. A numerical model for breaking waves: The volume of fluid method. Report No. CACR-97-02. Center for Applied Coastal Research.

Lynett, P.J. and Liu, P.L.-F. 2002 A numerical study of submerged landslide generated waves and runup. *Proc. Royal Soc.*, A. 458, 2885-2910.

Mei, C.C. 1989. The applied dynamics of ocean surface waves. World Scientific.

Narayanan, S. 1999. Experimental analysis of a nonlinear moored structure. Ph.D. Thesis. Oregon State University.

Nichols, B.D. and Hirt, C.W. 1971. Improved free surface boundary conditions for numerical incompressible-flow calculations. *J. Comp. Phys.*, 8, 434-448.

Noda, E. 1970. Water waves generated by landslides. *J. Waterways, Harbors and Coastal Engr. Div.*, ASCE, 125 (4), 207-215.

Walder, J.S., Watts, P., Sorensen, O.E. and Janssen, K. 2003. Tsunamis generated by subaerial mass flows. *J. Geophysical Research*, 108, EPM 2, 1-19

Watts, P. 1997. Water waves generated by underwater landslides, Ph.D. Thesis. California Institute of Technology.

Watts, P. and Grilli, S.T. 2003. Underwater landslide shape, motion, deformation and tsunami generation. *Proc. Thirteenth Int. Offshore and Polar Engr. Conf.*, 364-371.

Yim, S.C.S., Myrum, M.A., Gottlieb, O., Lin, H. and Shih, I-Ming. 1993. Summary and preliminary analysis of nonlinear oscillations in a submerged mooring system experiment. Report No. OE-93-03. Office of Naval Research.

Appendices

A. Numerical method for the RANS equations and structural dynamics

Numerical method for RANS equations

$$\frac{\partial \langle u_i \rangle}{\partial x_i} = 0 \tag{1}$$

$$\frac{\partial \langle u_i \rangle}{\partial t} + \langle u_j \rangle \frac{\partial \langle u_i \rangle}{\partial x_j} = -\frac{1}{\langle \rho \rangle} \frac{\partial \langle p \rangle}{\partial x_i} + g_i + \frac{1}{\langle \rho \rangle} \frac{\partial \langle \tau_{ij}^m \rangle}{\partial x_j} - \frac{\partial \langle u_i' u_j' \rangle}{\partial x_j} \tag{2}$$

Two-step projection method

The momentum equation is divided into two equations by introducing the intermediate velocity $\tilde{u}_i$ as

$$\frac{\tilde{u}_i - u_i^n}{\Delta t} = -u_j^n \frac{\partial u_i^n}{\partial x_j} + g_i + \frac{\partial \tau_{ij}^n}{\partial x_j} \tag{3}$$

$$\frac{u_i^{n+1} - \tilde{u}_i}{\Delta t} = -\frac{1}{\rho^n} \frac{\partial p^{n+1}}{\partial x_i} \tag{4}$$

where the superscripts n and $n+1$ represent two consecutive time steps, *i.e.*, $t_{n+1} = t_n + \Delta t$. Taking the divergence and applying the continuity condition to the resulting equation yields

$$\frac{\partial}{\partial x_i}\left(\frac{1}{\rho^n} \frac{\partial p^{n+1}}{\partial x_i} \right) = \frac{1}{\Delta t} \frac{\partial \tilde{u}_i}{\partial x_i} \tag{5}$$

Numerical evaluation of the variables

The linear interpolation is used to evaluate the variables at locations where those variables are not defined originally, e.g., the vertical velocity v at the horizontal cell face. Note that the bracket for the Reynolds average of the variables is dropped in the following equations for the convenience.

$$u_{i,j} = \frac{1}{2}\left\{u_{i+\frac{1}{2},j} + u_{i-\frac{1}{2},j}\right\} \tag{6}$$

$$u_{i,j+\frac{1}{2}} = \frac{u_{i,j+1}\Delta y_j + u_{i,j}\Delta y_{j+1}}{\Delta y_j + \Delta y_{j+1}} \tag{7}$$

$$v_{i,j} = \frac{1}{2}\left\{v_{i,j+\frac{1}{2}} + v_{i,j-\frac{1}{2}}\right\} \tag{8}$$

$$v_{i+\frac{1}{2},j} = \frac{v_{i+1,j}\Delta x_i + v_{i,j}\Delta x_{i+1}}{\Delta x_i + \Delta x_{i+1}} \tag{9}$$

Numerical evaluation of spatial derivatives

$$\left(\frac{\partial u}{\partial x}\right)_{i,j} = \frac{u_{i+\frac{1}{2},j} - u_{i-\frac{1}{2},j}}{\Delta x_i} \tag{10}$$

$$\left(\frac{\partial u}{\partial x}\right)_{i+1,j} = \frac{u_{i+\frac{3}{2},j} - u_{i+\frac{1}{2},j}}{\Delta x_{i+1}} \tag{11}$$

$$\left(\frac{\partial u}{\partial y}\right)_{i+\frac{1}{2},j+\frac{1}{2}} = \frac{u_{i+\frac{1}{2},j+1} - u_{i+\frac{1}{2},j}}{\Delta y_{j+\frac{1}{2}}} \tag{12}$$

$$\left(\frac{\partial u}{\partial y}\right)_{i+\frac{1}{2},j-\frac{1}{2}} = \frac{u_{i+\frac{1}{2},j} - u_{i+\frac{1}{2},j-1}}{\Delta y_{j-\frac{1}{2}}} \tag{13}$$

$$\left(\frac{\partial v}{\partial y}\right)_{i,j} = \frac{v_{i,j+\frac{1}{2}} - v_{i,j-\frac{1}{2}}}{\Delta y_j} \tag{14}$$

$$\left(\frac{\partial v}{\partial y}\right)_{i,j+1} = \frac{v_{i,j+\frac{3}{2}} - v_{i,j+\frac{1}{2}}}{\Delta y_{j+1}} \tag{15}$$

The advection terms in the x-momentum equation

$$u\frac{\partial u}{\partial x} + v\frac{\partial u}{\partial y} = u_{i+\frac{1}{2},j}\left(\frac{\partial u}{\partial x}\right)_{i+\frac{1}{2},j} + v_{i+\frac{1}{2},j}\left(\frac{\partial u}{\partial y}\right)_{i+\frac{1}{2},j} \tag{16}$$

$$\left(\frac{\partial u}{\partial x}\right)_{i+\frac{1}{2},j} = \frac{\left\{\begin{array}{l}\left[1+\alpha\,\mathrm{sgn}\left(u_{i+\frac{1}{2},j}\right)\right]\Delta x_{i+1}\left(\frac{\partial u}{\partial x}\right)_{i,j} \\ +\left[1-\alpha\,\mathrm{sgn}\left(u_{i+\frac{1}{2},j}\right)\right]\Delta x_i\left(\frac{\partial u}{\partial x}\right)_{i+1,j}\end{array}\right\}}{\Delta x_{i+1} + \Delta x_i + \alpha\,\mathrm{sgn}\left(u_{i+\frac{1}{2},j}\right)\left(\Delta x_{i+1} - \Delta x_i\right)} \tag{17}$$

$$\left(\frac{\partial u}{\partial y}\right)_{i+\frac{1}{2},j} = \frac{\left\{\begin{array}{l}\left[1+\alpha\,\mathrm{sgn}\left(v_{i+\frac{1}{2},j}\right)\right]\Delta y_{j+\frac{1}{2}}\left(\frac{\partial u}{\partial y}\right)_{i+\frac{1}{2},j-\frac{1}{2}} \\ +\left[1-\alpha\,\mathrm{sgn}\left(v_{i+\frac{1}{2},j}\right)\right]\Delta y_{j-\frac{1}{2}}\left(\frac{\partial u}{\partial y}\right)_{i++\frac{1}{2},j+\frac{1}{2}}\end{array}\right\}}{\Delta y_{j+\frac{1}{2}} + \Delta y_{j-\frac{1}{2}} + \alpha\,\mathrm{sgn}\left(v_{i+\frac{1}{2},j}\right)\left(\Delta y_{j+\frac{1}{2}} - \Delta y_{j-\frac{1}{2}}\right)} \tag{18}$$

The pressure term

$$\frac{\partial}{\partial x}\left(\frac{1}{\rho^n}\frac{\partial p^{n+1}}{\partial x}\right) + \frac{\partial}{\partial y}\left(\frac{1}{\rho^n}\frac{\partial p^{n+1}}{\partial y}\right) = \frac{1}{\Delta t}\left(\frac{\partial \tilde{u}}{\partial x} + \frac{\partial \tilde{v}}{\partial y}\right) \tag{19}$$

$$\frac{\partial}{\partial x}\left(\frac{1}{\rho^n}\frac{\partial p^{n+1}}{\partial x}\right)_{i,j} = \frac{1}{\Delta x_i}\left\{\frac{1}{\rho^n_{i+\frac{1}{2},j}}\left(\frac{\partial p}{\partial x}\right)^{n+1}_{i+\frac{1}{2},j} - \frac{1}{\rho^n_{i-\frac{1}{2},j}}\left(\frac{\partial p}{\partial x}\right)^{n+1}_{i-\frac{1}{2},j}\right\}$$
$$= \frac{1}{\Delta x_i}\left\{\frac{1}{\rho^n_{i+\frac{1}{2},j}}\left(\frac{p^{n+1}_{i+1,j} - p^{n+1}_{i,j}}{\Delta x_{i+\frac{1}{2}}}\right) - \frac{1}{\rho^n_{i-\frac{1}{2},j}}\left(\frac{p^{n+1}_{i,j} - p^{n+1}_{i-1,j}}{\Delta x_{i-\frac{1}{2}}}\right)\right\} \tag{20}$$

$$\frac{\partial}{\partial y}\left(\frac{1}{\rho^n}\frac{\partial p^{n+1}}{\partial y}\right)_{i,j} = \frac{1}{\Delta y_j}\left\{\frac{1}{\rho^n_{i,j+\frac{1}{2}}}\left(\frac{\partial p}{\partial y}\right)^{n+1}_{i,j+\frac{1}{2}} - \frac{1}{\rho^n_{i,j-\frac{1}{2}}}\left(\frac{\partial p}{\partial y}\right)^{n+1}_{i,j-\frac{1}{2}}\right\}$$
$$= \frac{1}{\Delta y_j}\left\{\frac{1}{\rho^n_{i,j+\frac{1}{2}}}\left(\frac{p^{n+1}_{i,j+1} - p^{n+1}_{i,j}}{\Delta y_{j+\frac{1}{2}}}\right) - \frac{1}{\rho^n_{i,j-\frac{1}{2}}}\left(\frac{p^{n+1}_{i,j} - p^{n+1}_{i,j-1}}{\Delta y_{j-\frac{1}{2}}}\right)\right\} \tag{21}$$

$$\left(\frac{\partial \tilde{u}}{\partial x} + \frac{\partial \tilde{v}}{\partial y}\right)_{i,j} = \frac{\tilde{u}_{i+\frac{1}{2},j} - \tilde{u}_{i-\frac{1}{2},j}}{\Delta x_i} + \frac{\tilde{v}_{i,j+\frac{1}{2}} - \tilde{v}_{i,j-\frac{1}{2}}}{\Delta y_j} \tag{22}$$

$$\rho^n_{i+\frac{1}{2},j} = \frac{\rho^n_{i,j}\Delta x_{i+1} + \rho^n_{i+1,j}\Delta x_i}{\Delta x_i + \Delta x_{i+1}} \tag{23}$$

The stress term in the x-momentum equation

$$\frac{\partial \tau_{xx}}{\partial x} + \frac{\partial \tau_{xy}}{\partial y} = \left(\frac{\partial \tau_{xx}}{\partial x} + \frac{\partial \tau_{xy}}{\partial y}\right)_{i+\frac{1}{2},j}$$
$$= \frac{(\tau_{xx})_{i+1,j} - (\tau_{xx})_{i,j}}{\Delta x_{i+\frac{1}{2}}} + \frac{(\tau_{xy})_{i+\frac{1}{2},j+\frac{1}{2}} - (\tau_{xy})_{i+\frac{1}{2},j-\frac{1}{2}}}{\Delta y_j} \tag{24}$$

$$(\tau_{xx})_{i,j} = \left(\frac{\partial u}{\partial x}\right)_{i,j} = \frac{u_{i+\frac{1}{2},j} - u_{i-\frac{1}{2},j}}{\Delta x_i} \tag{25}$$

$$(\tau_{xy})_{i+\frac{1}{2},j+\frac{1}{2}} = \left(\frac{\partial u}{\partial y}\right)_{i+\frac{1}{2},j+\frac{1}{2}} = \frac{u_{i+\frac{1}{2},j+1} - u_{i+\frac{1}{2},j}}{\Delta y_{j+\frac{1}{2}}} \tag{26}$$

The VOF method

The kinematic boundary condition for the free surface can be expressed as the total derivative of $\rho(x,y,t)$. This implies that the total derivative of the surface with respect to time would be zero on the surface if the surface varies with time.

$$\frac{D\rho}{Dt} = \frac{\partial \rho}{\partial t} + u\frac{\partial \rho}{\partial x} + v\frac{\partial \rho}{\partial y} = 0 \tag{27}$$

Defining $\rho(x,y,t)=F(x,y,t)\rho_f$ and substituting this definition into the equation above yields

$$\frac{\partial F}{\partial t} + u\frac{\partial F}{\partial x} + v\frac{\partial F}{\partial y} = 0 \tag{28}$$

For a computational cell (i, j), the above equation is written in the following finite difference form.

$$F_{i,j}^{n+1} = F_{i,j}^{n} - \frac{\Delta t}{\Delta x_i}\left(u_{i+\frac{1}{2},j}^{n+1} F_R^n - u_{i-\frac{1}{2},j}^{n+1} F_L^n\right) - \frac{\Delta t}{\Delta y_j}\left(v_{i,j+\frac{1}{2}}^{n+1} F_T^n - v_{i,j-\frac{1}{2}}^{n+1} F_B^n\right) \tag{29}$$

Where F_R^n, F_L^n, F_T^n and F_B^n denote the F values on the right, left, top and bottom face of the cell, respectively. Depending on the configuration of the free surface, a different value is assigned to the F at the faces. The algorithm proposed by Hirt and Nichols (1981) where the free surface is reconstructed

either horizontal or vertically in the free surface cells based on the F values at the time step t_n. Based on the spatial derivatives of F, the free surface is reconstructed as following.

$$\left|\frac{\partial F}{\partial y}\right| > \left|\frac{\partial F}{\partial x}\right| \quad \text{and} \quad \frac{\partial F}{\partial x} < 0 \quad \rightarrow \quad \text{vertical free surface on the left side}$$

$$\left|\frac{\partial F}{\partial x}\right| > \left|\frac{\partial F}{\partial y}\right| \quad \text{and} \quad \frac{\partial F}{\partial x} > 0 \quad \rightarrow \quad \text{vertical free surface on the right side}$$

$$\left|\frac{\partial F}{\partial y}\right| > \left|\frac{\partial F}{\partial x}\right| \quad \text{and} \quad \frac{\partial F}{\partial y} < 0 \quad \rightarrow \quad \text{horizontal free surface on the bottom side}$$

$$\left|\frac{\partial F}{\partial y}\right| > \left|\frac{\partial F}{\partial x}\right| \quad \text{and} \quad \frac{\partial F}{\partial y} > 0 \quad \rightarrow \quad \text{horizontal free surface on the top side}$$

The derivatives of F are evaluated by using the central difference scheme.

The derivative of F with respect to x is evaluated as

$$\left(\frac{\partial F}{\partial x}\right)_{i,j} = \frac{\left(\frac{\partial F}{\partial x}\right)_{i+\frac{1}{2},j} \Delta x_{i-\frac{1}{2}} + \left(\frac{\partial F}{\partial x}\right)_{i-\frac{1}{2},j} \Delta x_{i+\frac{1}{2}}}{\Delta x_{i-\frac{1}{2}} + \Delta x_{i+\frac{1}{2}}}$$

$$= \frac{\left\{\frac{\Delta x_{i-\frac{1}{2}}}{\Delta x_{i+\frac{1}{2}}}\left(\hat{F}_{i+1,j} - \hat{F}_{i,j}\right) + \frac{\Delta x_{i+\frac{1}{2}}}{\Delta x_{i-\frac{1}{2}}}\left(\hat{F}_{i,j} - \hat{F}_{i-1,j}\right)\right\}}{\Delta x_{i-\frac{1}{2}} + \Delta x_{i+\frac{1}{2}}} \tag{30}$$

where $\hat{F}_{i,j}$ is the average of the F values in the three vertical neighboring cells, i.e.,

$$\hat{F}_{i,j} = \frac{F_{i,j+1}\Delta y_{j+1} + F_{i,j}\Delta y_j + F_{i,j-1}\Delta y_{j-1}}{\Delta y_{j+1} + \Delta y_j + \Delta y_{j-1}} \tag{31}$$

Once the free surface configuration is reconstructed, the donor-acceptor method is used to advect the VOF function. For the demonstration purpose, the advection in the x direction is discussed here. When $u^{n+1}_{i+\frac{1}{2},j} > 0$, the (i,j) cell becomes the donor cell and the $(i+1,j)$ cell is the acceptor cell. If $u^{n+1}_{i+\frac{1}{2},j} < 0$, the role of the donor and acceptor cells are switched.

When the free surface in the donor cell is horizontal, F^n_R is assigned to be the F value in the donor cell, i.e.,

$$F^n_R = F^n_{i,j} = F^n_{id} \tag{32}$$

If the free surface in the donor cell is vertical, the advection of the VOF function should be more strongly influenced by the F value in the acceptor cell. Therefore, F^n_R is assigned to be the F value in the acceptor cell.

$$F^n_R = F^n_{i+1,j} = F^n_{ia} \tag{33}$$

Under certain conditions, over-filling problems are observed. In other words, the F values become larger than 1.0 in a free surface cell. To prevent this over-

filling problem, a corrector term is used in the acceptor method.

$$F_R^n = F_{ia}^n + \max\left[\left\{\left(\max\left\langle F_{id}^n, F_{idm}^n, k\right\rangle - F_{ia}^n\right) - \frac{\Delta x_{id}}{u_{i+\frac{1}{2},j}^{n+1}\Delta t}\left(F_{dm}^n - F_{id}^n\right)\right\}, 0\right] \tag{34}$$

where k is a factor introduced to prevent spurious advection of a small amount of fluid and often set to be 0.1.

The k-ε equation.

$$\frac{\partial k}{\partial t} + \langle u_j\rangle\frac{\partial k}{\partial x_j} = \frac{\partial}{\partial x_j}\left[\left(\frac{\nu_t}{\sigma_k} + \nu\right)\frac{\partial k}{\partial x_j}\right] - \langle u_i' u_j'\rangle\frac{\partial\langle u_i\rangle}{\partial x_j} - \varepsilon \tag{35}$$

$$\begin{aligned}\frac{\partial \varepsilon}{\partial t} + \langle u_j\rangle\frac{\partial \varepsilon}{\partial x_j} &= \frac{\partial}{\partial x_j}\left[\left(\frac{\nu_t}{\sigma_\varepsilon} + \nu\right)\frac{\partial \varepsilon}{\partial x_j}\right] \\ &\quad + C_{1\varepsilon}\frac{\varepsilon}{k}\nu_t\left(\frac{\partial\langle u_i\rangle}{\partial x_j} + \frac{\partial\langle u_j\rangle}{\partial x}\right)\frac{\partial\langle u_i\rangle}{\partial x_j} - C_{2\varepsilon}\frac{\varepsilon^2}{k}\end{aligned} \tag{36}$$

The advection term

$$\begin{aligned}u\frac{\partial k}{\partial x} &= \left(u\frac{\partial k}{\partial x}\right)_{i,j}^n = u_{i,j}^{n+1}\left(\frac{\partial k}{\partial x}\right)_{i,j}^n \\ &= u_{i,j}^{n+1}\frac{\left[1+\gamma\,\mathrm{sgn}\left(u_{i,j}^{n+1}\right)\right]\Delta x_{i+\frac{1}{2}}\left(\frac{\partial k}{\partial x}\right)_{i-\frac{1}{2},j}^n + \left[1-\gamma\,\mathrm{sgn}\left(u_{i,j}^{n+1}\right)\right]\Delta x_{i-\frac{1}{2}}\left(\frac{\partial k}{\partial x}\right)_{i+\frac{1}{2},j}^n}{\Delta x_{i+\frac{1}{2}} + \Delta x_{i-\frac{1}{2}} + \gamma\,\mathrm{sgn}\left(u_{i,j}^{n+1}\right)\left(\Delta x_{i+\frac{1}{2}} - \Delta x_{i-\frac{1}{2}}\right)}\end{aligned} \tag{37}$$

where

$$\left(\frac{\partial k}{\partial x}\right)_{i-\frac{1}{2},j}^n = \frac{k_{i,j}^n - k_{i-1,j}^n}{\Delta x_{i-\frac{1}{2}}} \tag{38}$$

$$\left(\frac{\partial k}{\partial x}\right)^n_{i+\frac{1}{2},j} = \frac{k^n_{i+1,j} - k^n_{i,j}}{\Delta x_{i+\frac{1}{2}}} \tag{39}$$

and γ is the weighting factor between the central difference and the upwind scheme. In the computation, γ of 1.0 is used which makes the advection terms discretized by the upwind scheme. Such scheme ensures the stable solution for the k equation under any conditions.

$$\begin{aligned} \nu\frac{\partial k}{\partial y} &= \left(\nu\frac{\partial k}{\partial y}\right)^n_{i,j} = \nu^{n+1}_{i,j}\left(\frac{\partial k}{\partial y}\right)^n_{i,j} \\ &= \nu^{n+1}_{i,j}\frac{\left[1+\gamma\,\mathrm{sgn}\left(\nu^{n+1}_{i,j}\right)\right]\Delta y_{j+\frac{1}{2}}\left(\frac{\partial k}{\partial x}\right)^n_{i,j-\frac{1}{2}} + \left[1-\gamma\,\mathrm{sgn}\left(\nu^{n+1}_{i,j}\right)\right]\Delta y_{j-\frac{1}{2}}\left(\frac{\partial k}{\partial y}\right)^n_{i,j+\frac{1}{2}}}{\Delta y_{j+\frac{1}{2}} + \Delta y_{j-\frac{1}{2}} + \gamma\,\mathrm{sgn}\left(\nu^{n+1}_{i,j}\right)\left(\Delta y_{j+\frac{1}{2}} - \Delta y_{j-\frac{1}{2}}\right)} \end{aligned} \tag{40}$$

where

$$\left(\frac{\partial k}{\partial y}\right)^n_{i,j-\frac{1}{2}} = \frac{k^n_{i,j} - k^n_{i,j-1}}{\Delta y_{j=\frac{1}{2}}} \tag{41}$$

$$\left(\frac{\partial k}{\partial y}\right)^n_{i,j+\frac{1}{2}} = \frac{k^n_{i,j+1} - k^n_{i,j}}{\Delta y_{j+\frac{1}{2}}} \tag{42}$$

The diffusion term

$$\frac{\partial}{\partial x_j}\left[\left(\frac{\nu_t}{\sigma_k}+\nu\right)\frac{\partial k}{\partial x_j}\right] = \frac{\partial}{\partial x}\left[\left(\frac{\nu_t}{\sigma_k}+\nu\right)\frac{\partial k}{\partial x}\right] + \frac{\partial}{\partial y}\left[\left(\frac{\nu_t}{\sigma_k}+\nu\right)\frac{\partial k}{\partial y}\right] \tag{43}$$

The first and second terms on the right hand side of the above equation is

approximated as

$$\left\{\frac{\partial}{\partial x}\left[\left(\frac{\nu_t}{\sigma_k}+\nu\right)\frac{\partial k}{\partial x}\right]\right\}_{i,j}^{n}=\frac{\left(\frac{\nu_t}{\sigma_k}+\nu\right)_{i+\frac{1}{2},j}^{n}\left(\frac{\partial k}{\partial x}\right)_{i+\frac{1}{2},j}^{n}-\left(\frac{\nu_t}{\sigma_k}+\nu\right)_{i-\frac{1}{2},j}^{n}\left(\frac{\partial k}{\partial x}\right)_{i-\frac{1}{2},j}^{n}}{\Delta x_i} \tag{44}$$

$$=\frac{1}{\Delta x_i}\left\{\left(\frac{\nu_t}{\sigma_k}+\nu\right)_{i+\frac{1}{2},j}^{n}\frac{k_{i+1,j}^{n}-k_{i,j}^{n}}{\Delta x_{i+\frac{1}{2}}}-\left(\frac{\nu_t}{\sigma_k}+\nu\right)_{i-\frac{1}{2},j}^{n}\frac{k_{i,j}^{n}-k_{i-1,j}^{n}}{\Delta x_{i-\frac{1}{2}}}\right\}$$

$$\left\{\frac{\partial}{\partial y}\left[\left(\frac{\nu_t}{\sigma_k}+\nu\right)\frac{\partial k}{\partial y}\right]\right\}_{i,j}^{n}=\frac{\left(\frac{\nu_t}{\sigma_k}+\nu\right)_{i,j+\frac{1}{2}}^{n}\left(\frac{\partial k}{\partial y}\right)_{i,j+\frac{1}{2}}^{n}-\left(\frac{\nu_t}{\sigma_k}+\nu\right)_{i,j-\frac{1}{2}}^{n}\left(\frac{\partial k}{\partial y}\right)_{i,j-\frac{1}{2}}^{n}}{\Delta y_j} \tag{45}$$

$$=\frac{1}{\Delta y_j}\left\{\left(\frac{\nu_t}{\sigma_k}+\nu\right)_{i,j+\frac{1}{2}}^{n}\frac{k_{i,j+1}^{n}-k_{i,j}^{n}}{\Delta y_{j+\frac{1}{2}}}-\left(\frac{\nu_t}{\sigma_k}+\nu\right)_{i,j-\frac{1}{2}}^{n}\frac{k_{i,j}^{n}-k_{i,j-1}^{n}}{\Delta y_{j-\frac{1}{2}}}\right\}$$

The evaluation of $\left(\frac{\nu_t}{\sigma_k}+\nu\right)$ at the cell faces is done by using the linear interpolations as given by

$$\left(\frac{\nu_t}{\sigma_k}+\nu\right)_{i+\frac{1}{2},j}^{n}=\frac{\Delta x_i\left(\frac{\nu_t}{\sigma_k}+\nu\right)_{i+1,j}^{n}+\Delta x_{i+1}\left(\frac{\nu_t}{\sigma_k}+\nu\right)_{i,j}^{n}}{\Delta x_i+\Delta x_{i+1}} \tag{46}$$

The product term

$$\left\langle u_i' u_j' \right\rangle \frac{\partial \langle u_i \rangle}{\partial x_j} = \frac{1}{2}\left[\left\{ \left\langle u_i' u_j' \right\rangle \frac{\partial \langle u_i \rangle}{\partial x_j} \right\}^{n} + \left\{ \left\langle u_i' u_j' \right\rangle \frac{\partial \langle u_i \rangle}{\partial x_j} \right\}^{n+1} \right]$$

$$= \frac{1}{2}\left\{ \begin{array}{l} \left[\left\langle u'u' \right\rangle \frac{\partial u}{\partial x} + \left\langle u'v' \right\rangle \frac{\partial u}{\partial y} + \left\langle v'u' \right\rangle \frac{\partial v}{\partial x} + \left\langle v'v' \right\rangle \frac{\partial v}{\partial x} \right]_{i,j}^{n} \\ + \left[\left\langle u'u' \right\rangle \frac{\partial u}{\partial x} + \left\langle u'v' \right\rangle \frac{\partial u}{\partial y} + \left\langle v'u' \right\rangle \frac{\partial v}{\partial x} + \left\langle v'v' \right\rangle \frac{\partial v}{\partial x} \right]_{i,j}^{n+1} \end{array} \right\} \quad (47)$$

The correlations of velocity fluctuations are determined by the nonlinear algebraic Reynolds stress model with the given k, ε and strain rates of the mean flow. The evaluations of spatial derivatives of velocities are referred to Equations (10-15) in the Appendix A.

Numerical method for structural dynamics

The Newmark integration method

Under the assumption of the linear acceleration, average acceleration from t to $t+\Delta t$ is expressed as

$$\{\ddot{x}\}_{avg} = \frac{1}{2}\left(\{\ddot{x}(t)\} + \{\ddot{x}(t+\Delta t)\}\right) \quad (48)$$

Thus the velocity and the displacement vectors at $t+\Delta t$ can be expressed as

$$\{\dot{x}(t+\Delta t)\} = \{\dot{x}(t)\} + \Delta t\{\ddot{x}\}_{avg} = \{\dot{x}(t)\} + \frac{\Delta t}{2}\left(\{\ddot{x}(t)\} + \{\ddot{x}(t+\Delta t)\}\right) \quad (49)$$

$$\{x(t+\Delta t)\} = \{x(t)\} + \Delta t\{\dot{x}\}_{avg} = \{x(t)\} + \frac{\Delta t}{2}(\{\dot{x}(t)\} + \{\dot{x}(t+\Delta t)\})$$
$$= \{x(t)\} + \frac{\Delta t}{2}\left(\{\dot{x}(t)\} + \{\dot{x}(t)\} + \frac{\Delta t}{2}(\{\ddot{x}(t)\} + \{\ddot{x}(t+\Delta t)\})\right) \quad (50)$$
$$= \{x(t)\} + \Delta t\{\dot{x}(t)\} + \frac{(\Delta t)^2}{4}[\{\ddot{x}(t)\} + \{\ddot{x}(t+\Delta t)\}]$$

The general Newmark integration may be expressed as

$$\{\dot{x}(t+\Delta t)\} = \{\dot{x}(t)\} + \Delta t[(1-\delta)\{\ddot{x}(t)\} + \delta\{\ddot{x}(t+\Delta t)\}] \quad (51)$$

$$\{x(t+\Delta t)\} = \{x(t)\} + \Delta t\{\dot{x}(t)\} + (\Delta t)^2\left[\left(\frac{1}{2}-\alpha\right)\{\ddot{x}(t)\} + \alpha\{\ddot{x}(t+\Delta t)\}\right] \quad (52)$$

where α and δ are parameters that can be determined to obtain integration accuracy and stability. Note that the equations above recover the average acceleration method for α=1/4 and δ=1/2. For α=1/6 and δ=1/2, the method is called the linear acceleration method.

The general form of linear equation of motion for multi-degree-of-freedom system can be expressed by

$$[M]\{\ddot{x}(t)\} + [C]\{\dot{x}(t)\} + [K]\{x(t)\} = \{F(t)\} \quad (53)$$

where $[M], [C], [K]$ and $\{F\}$ denote mass matrix, structural damping matrix, stiffness matrix and forcing vector, respectively.

Substituting and collecting appropriate terms yields

$$\begin{aligned}(a_0[M]+a_1[C]+[K])\{x(t+\Delta t)\} \\ =\{F(t+\Delta t)\}+[M](a_0\{x(t)\}+a_2\{\dot{x}(t)\}+a_2\{\ddot{x}(t)\}) \\ +[C](a_1\{x(t)\}+a_4\{\dot{x}(t)\}+a_5\{\ddot{x}(t)\})\end{aligned} \tag{54}$$

where $a_0=\frac{1}{\alpha\Delta t^2}$, $a_1=\frac{\delta}{\alpha\Delta t}$, $a_2=\frac{1}{\alpha\Delta t}$, $a_3=\frac{1}{2\alpha}-1$, $a_4=\frac{\delta}{\alpha}-1$ and $a_5=\frac{\Delta t}{2}\left(\frac{\delta}{\alpha}-2\right)$.

Therefore, the displacement at $t+\Delta t$ can be determined from

$$[\overline{K}]\{x(t+\Delta t)\}=\{\overline{F}\} \tag{55}$$

where

$$[\overline{K}]=a_0[M]+a_1[C]+[K] \tag{56}$$

$$\begin{aligned}\{\overline{F}\}=\{F(t+\Delta t)\}+[M](a_0\{x(t)\}+a_2\{\dot{x}(t)\}+a_2\{\ddot{x}(t)\}) \\ +[C](a_1\{x(t)\}+a_4\{\dot{x}(t)\}+a_5\{\ddot{x}(t)\})\end{aligned} \tag{57}$$

Then the acceleration and velocity at $t+\Delta t$ can be obtained from

$$\{\ddot{x}(t+\Delta t)\}=a_0[\{x(t+\Delta t)\}-\{x(t)\}]-a_2\{\dot{x}(t)\}-a_3\{\ddot{x}(t)\} \tag{58}$$

$$\{\dot{x}(t+\Delta t)\}=\{\dot{x}(t)\}+a_6\{\ddot{x}(t)\}+a_7\{\ddot{x}(t+\Delta t)\} \tag{59}$$

It is known that the average acceleration method (i.e., $\alpha=1/4$ and $\delta=1/2$) is unconditionally stable and the linear acceleration method (i.e., $\alpha=1/6$ and $\delta=1/2$) becomes unstable when $\Delta t/T \geq 0.55$. T is the total time length of the integration.

B. Numerical modeling of the box-drop and experimental data

Snapshots of the freefalling rigid body and wave generation in the near field region described in Chapter 5 are shown here. The graphic images of numerical results are scaled such that the size and initial location of the rigid body are exactly the same as those in the digital images from the experiments. Transparency of the scaled plots is changed to 60% and the plots are overlapped on the experiment images so that free surface and moving boundary locations may be compared directly. The free surfaces and moving rigid boundaries of numerical model are shown in thick solid lines. Time increments of consecutive snapshots shown in figures are 0.08 second. Numbers in the vertical and horizontal axes represent length in meters.

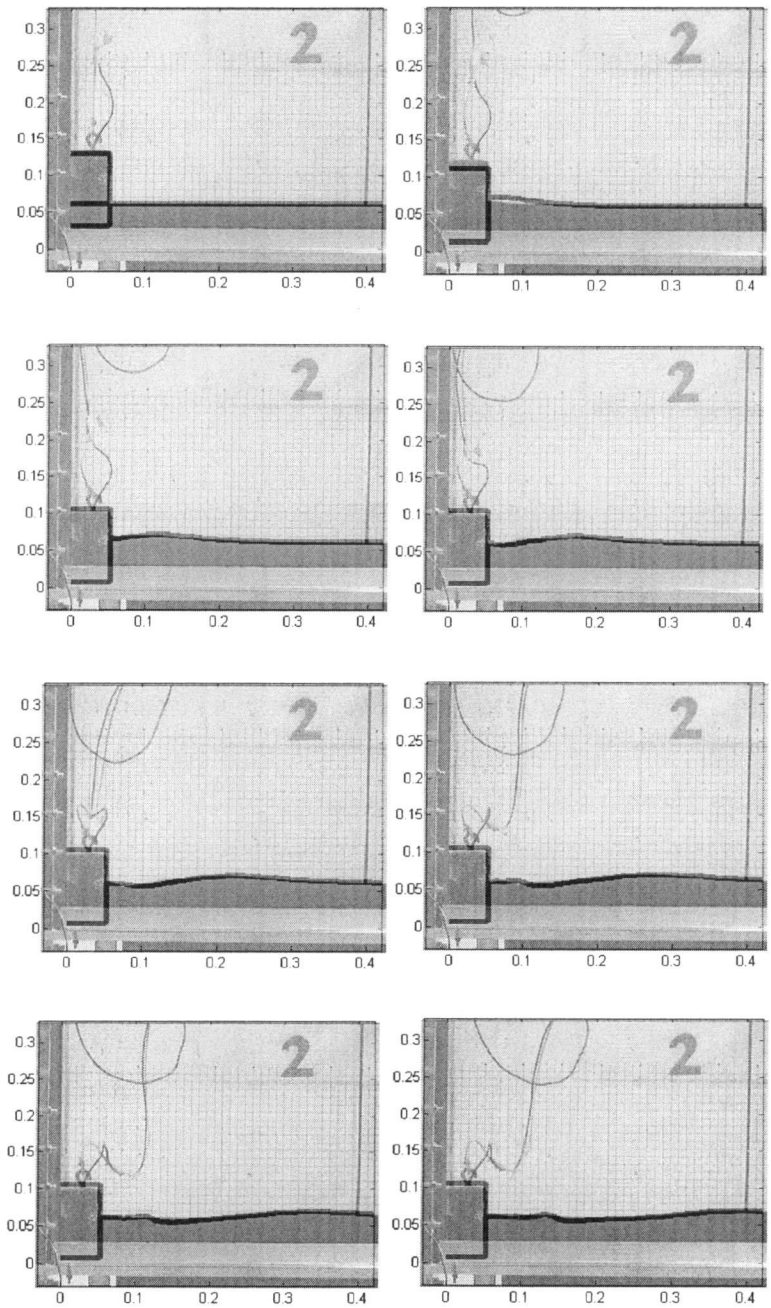

Fig 1. Snapshots of rigid body drop and wave generation, Test L5H6M3

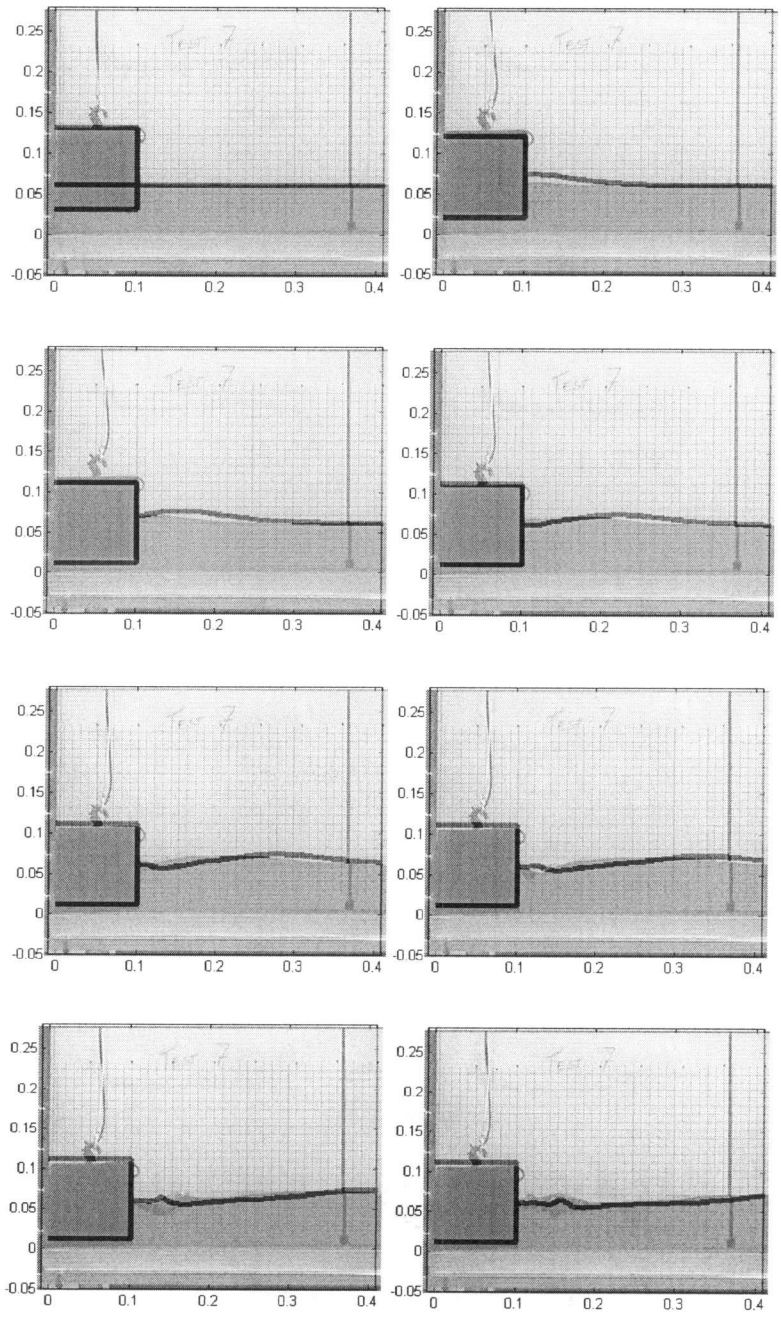

Fig 2. Snapshots of rigid body drop and wave generation, Test L10H6M3

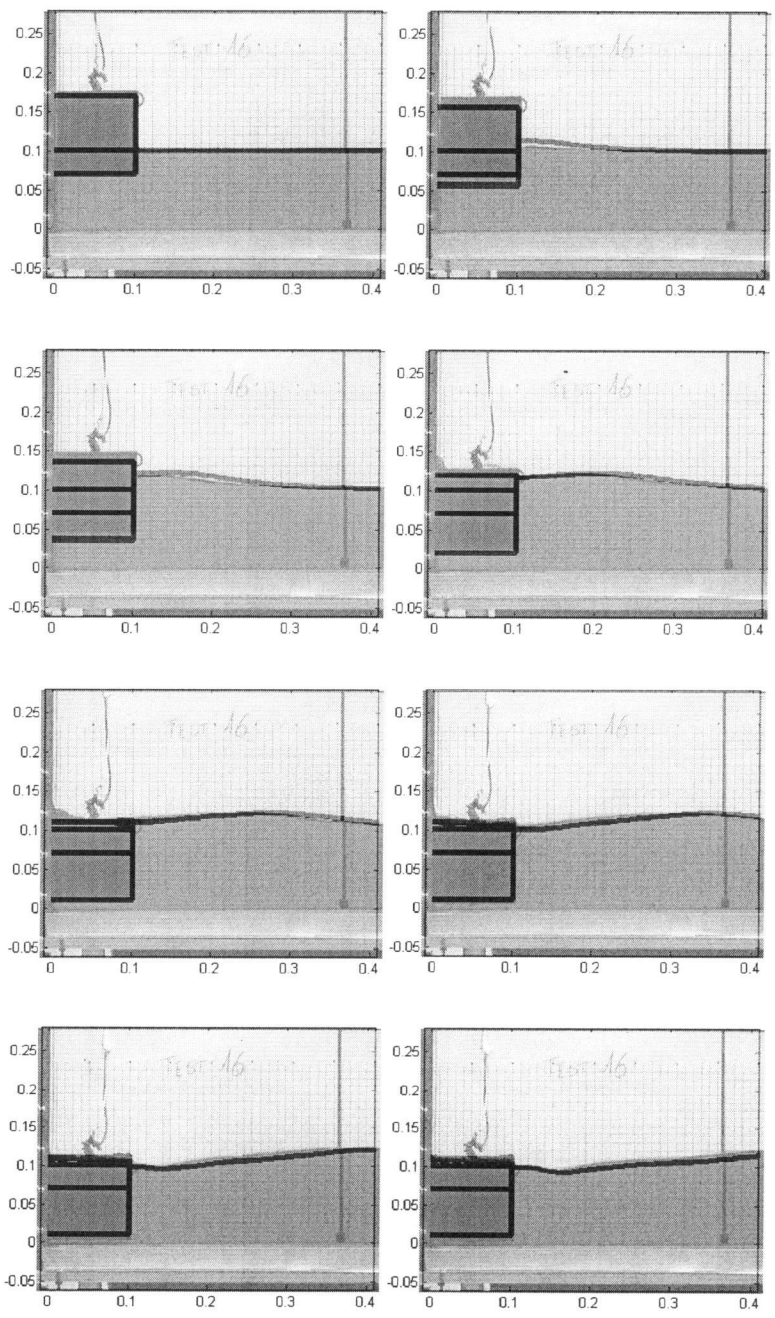

Fig 3. Snapshots of rigid body drop and wave generation, Test L10H10M3

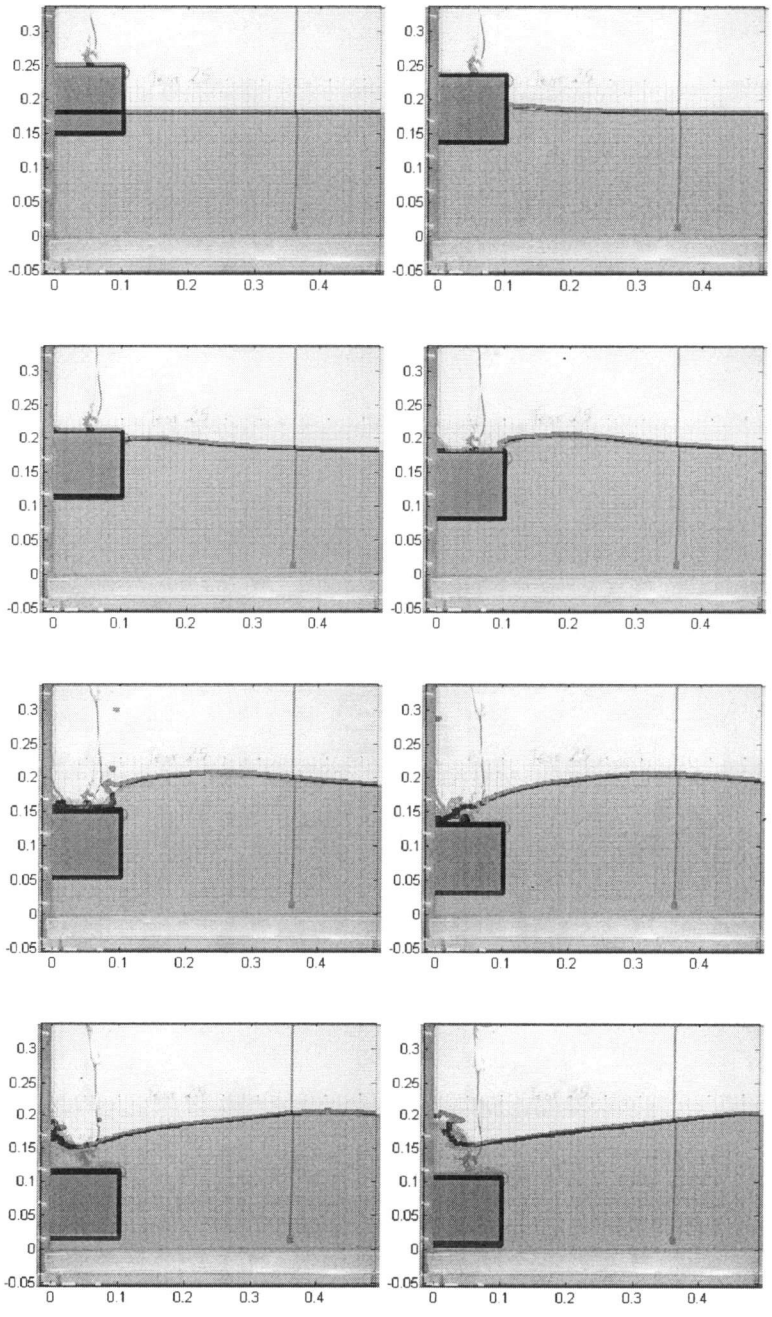

Fig 4. Snapshots of rigid body drop and wave generation, Test L10H18M3

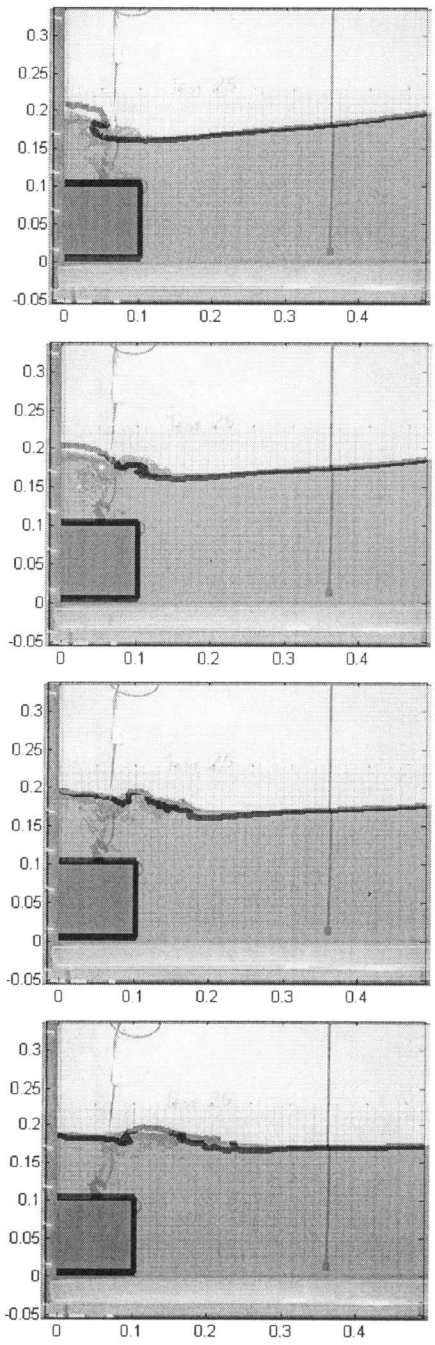

Fig 4. Snapshots of rigid body drop and wave generation, Test L10H18M3 (continued)

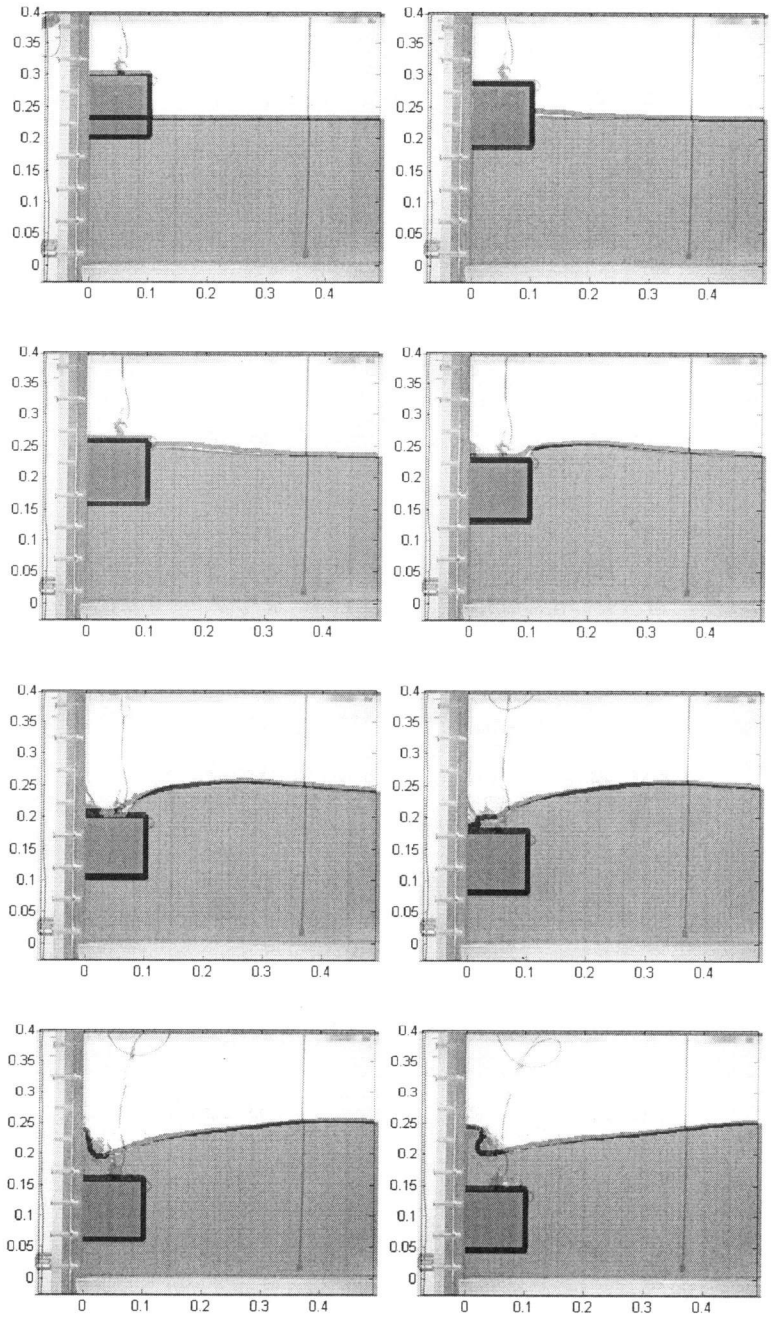

Fig 5. Snapshots of rigid body drop and wave generation, Test L10H23M3

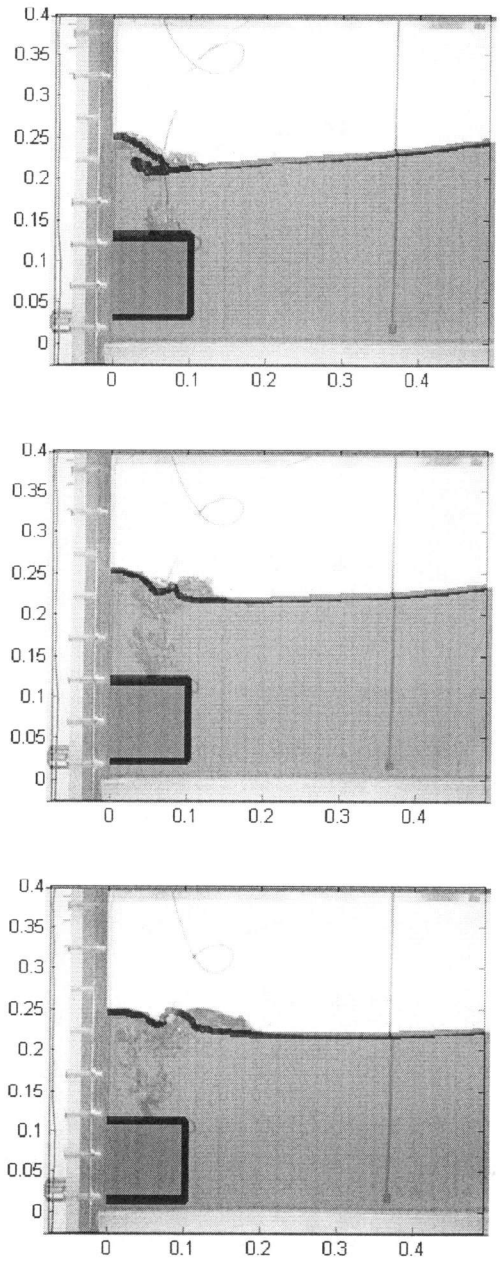

Fig 5. Snapshots of rigid body drop and wave generation, Test L10H23M3 (continued)

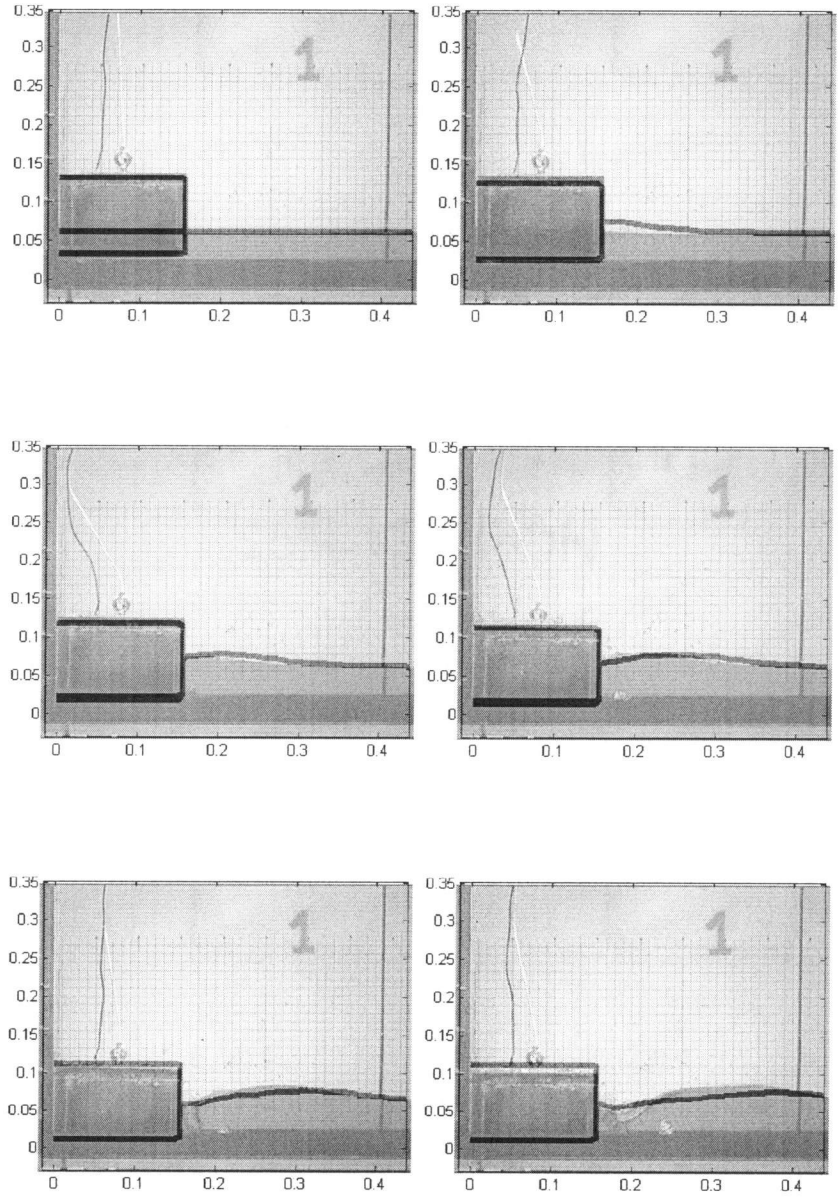

Fig 6. Snapshots of rigid body drop and wave generation, Test L15H6M3

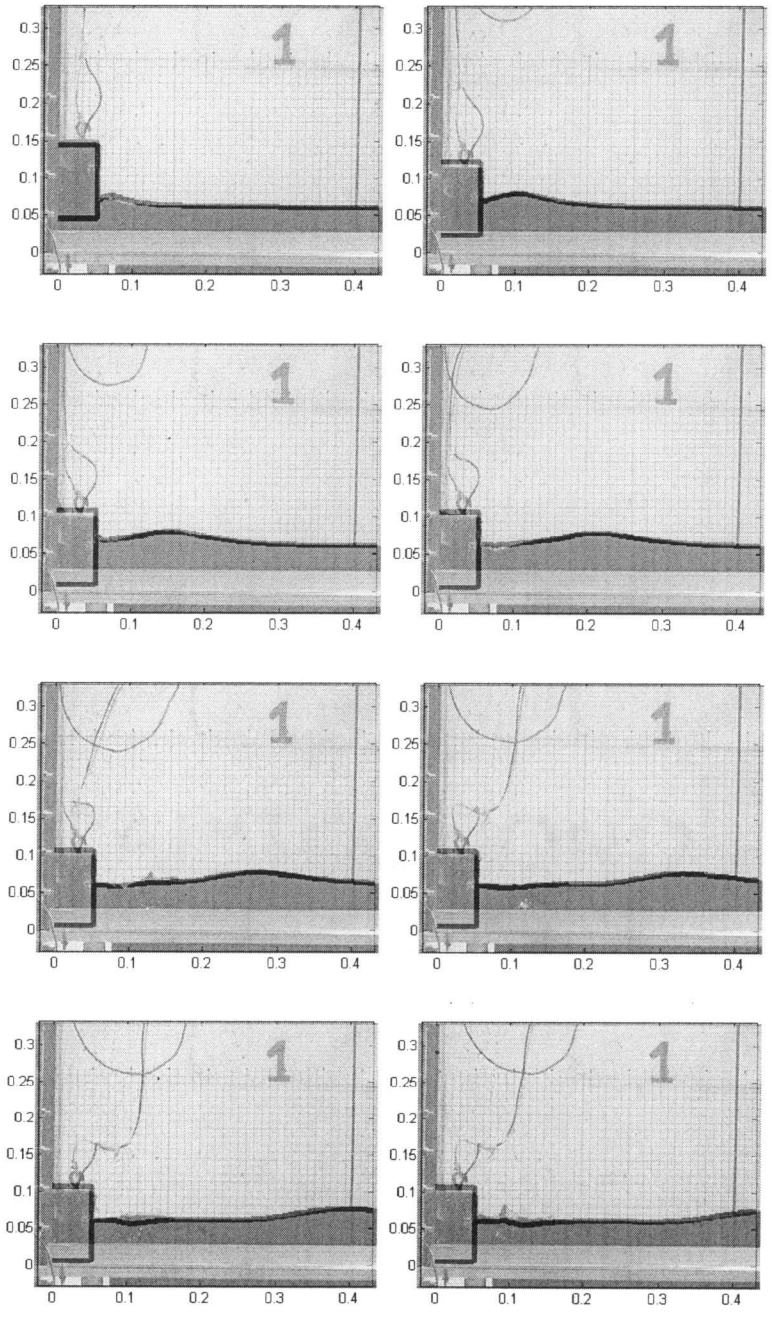

Fig 7. Snapshots of rigid body drop and wave generation, Test L5H6PM0

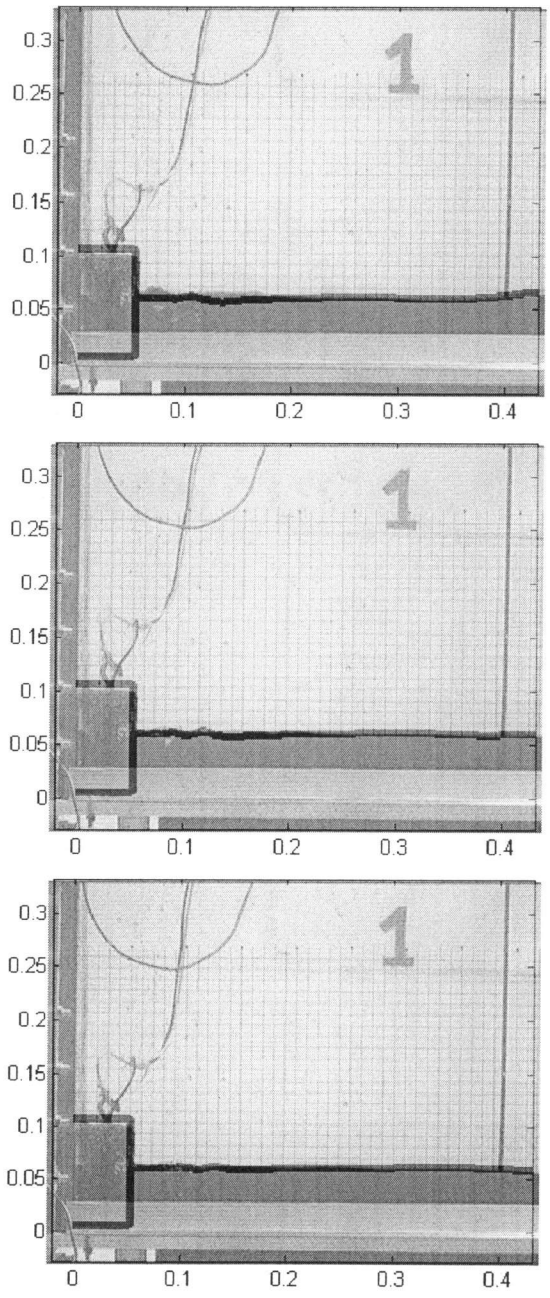

Fig 7. Snapshots of rigid body drop and wave generation, Test L5H6PM0 (continued)

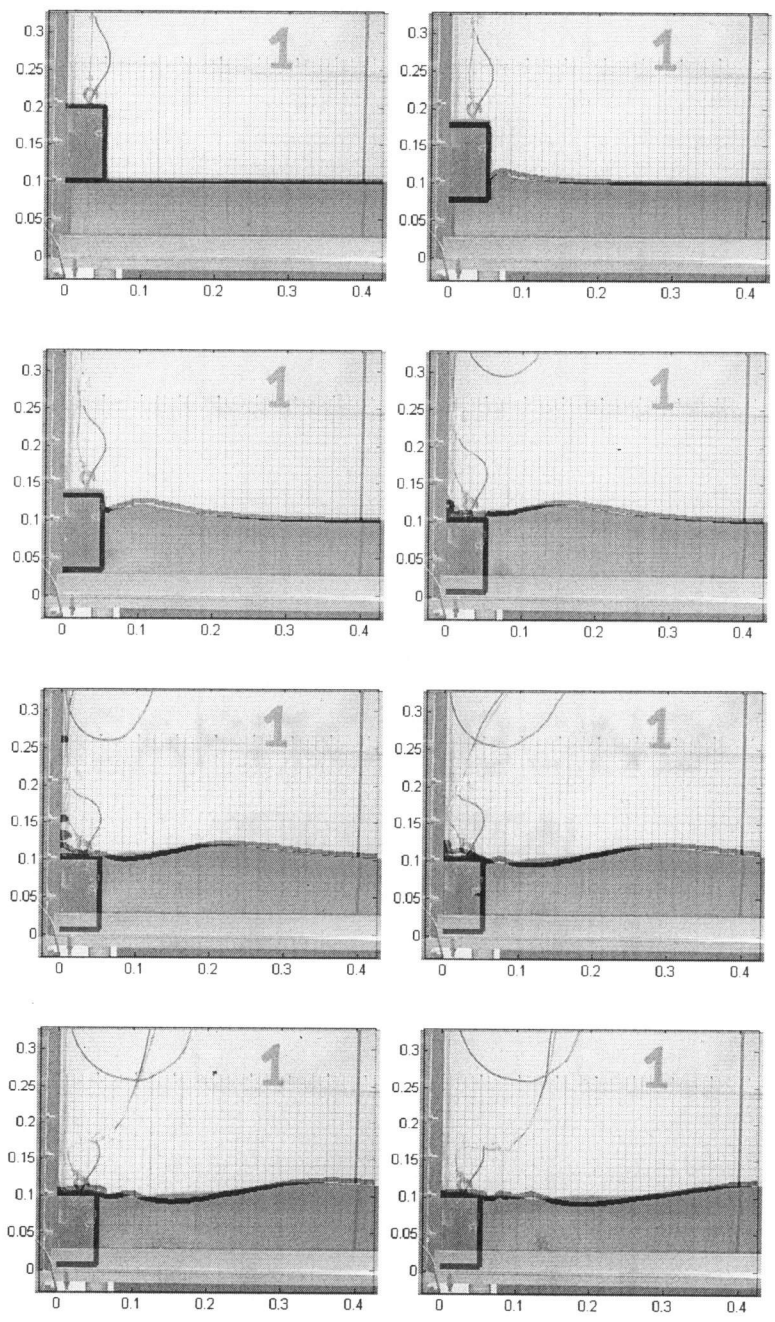

Fig 8. Snapshots of rigid body drop and wave generation, Test L5H10PM0

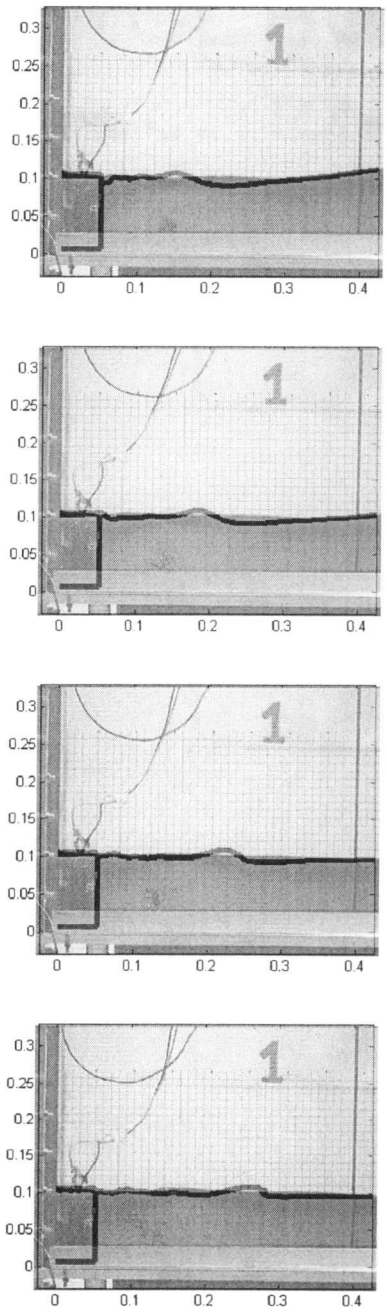

Fig 8. Snapshots of rigid body drop and wave generation, Test L5H10PM0 (continued)

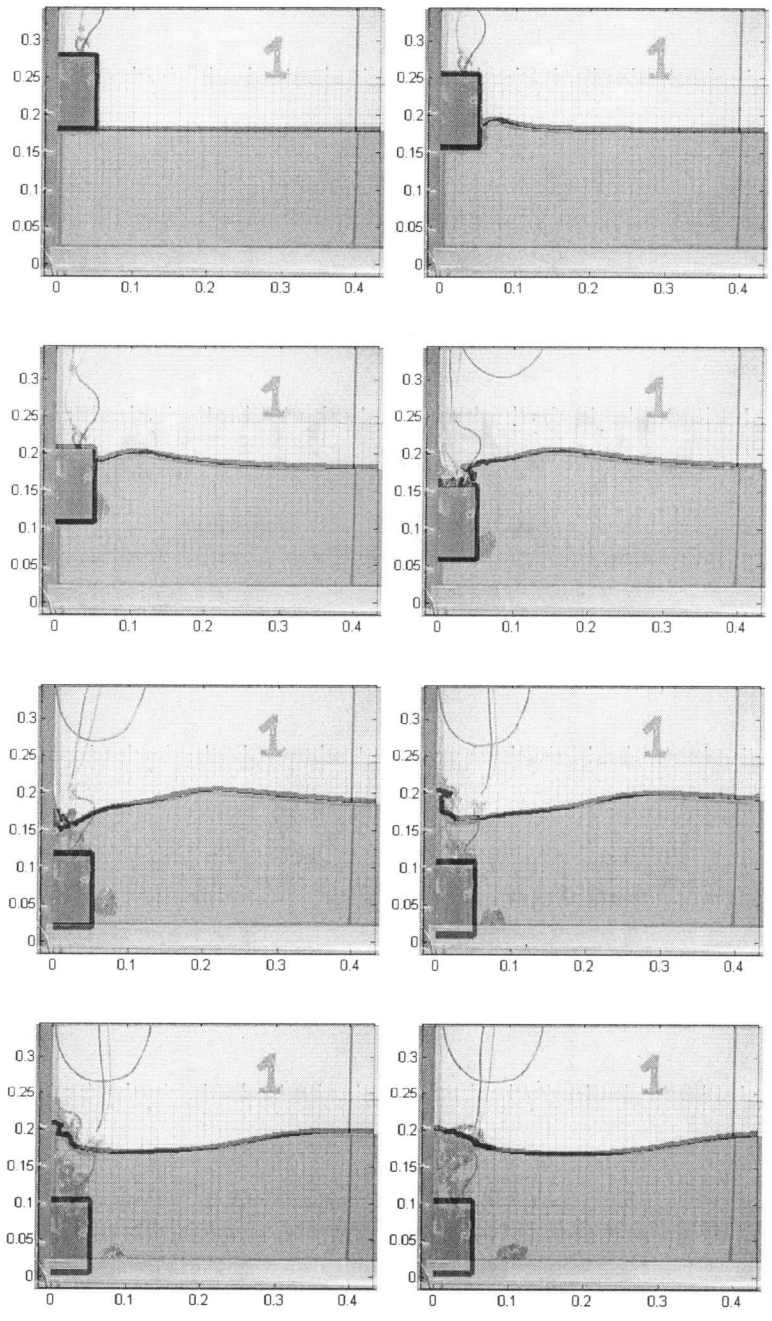

Fig 9. Snapshots of rigid body drop and wave generation, Test L5H18PM0

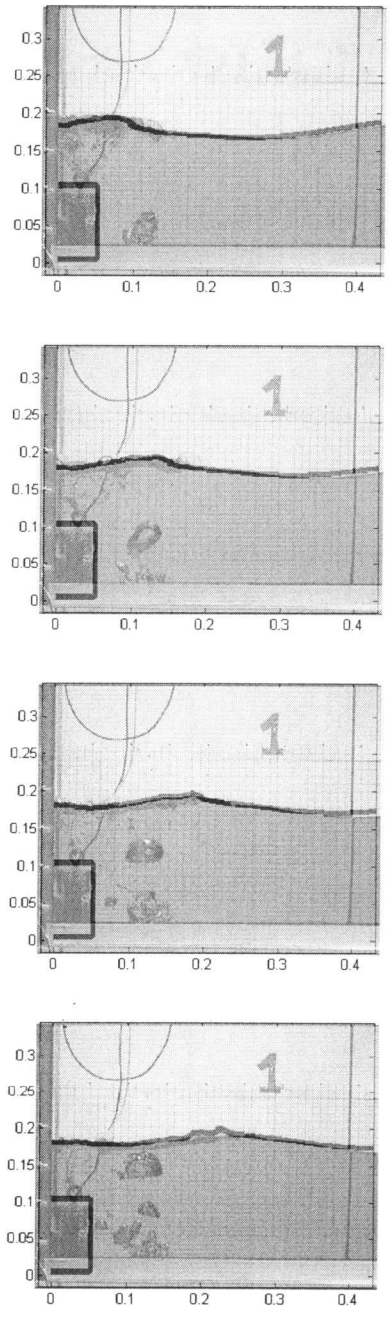

Fig 9. Snapshots of rigid body drop and wave generation, Test L5H18PM0 (continued)

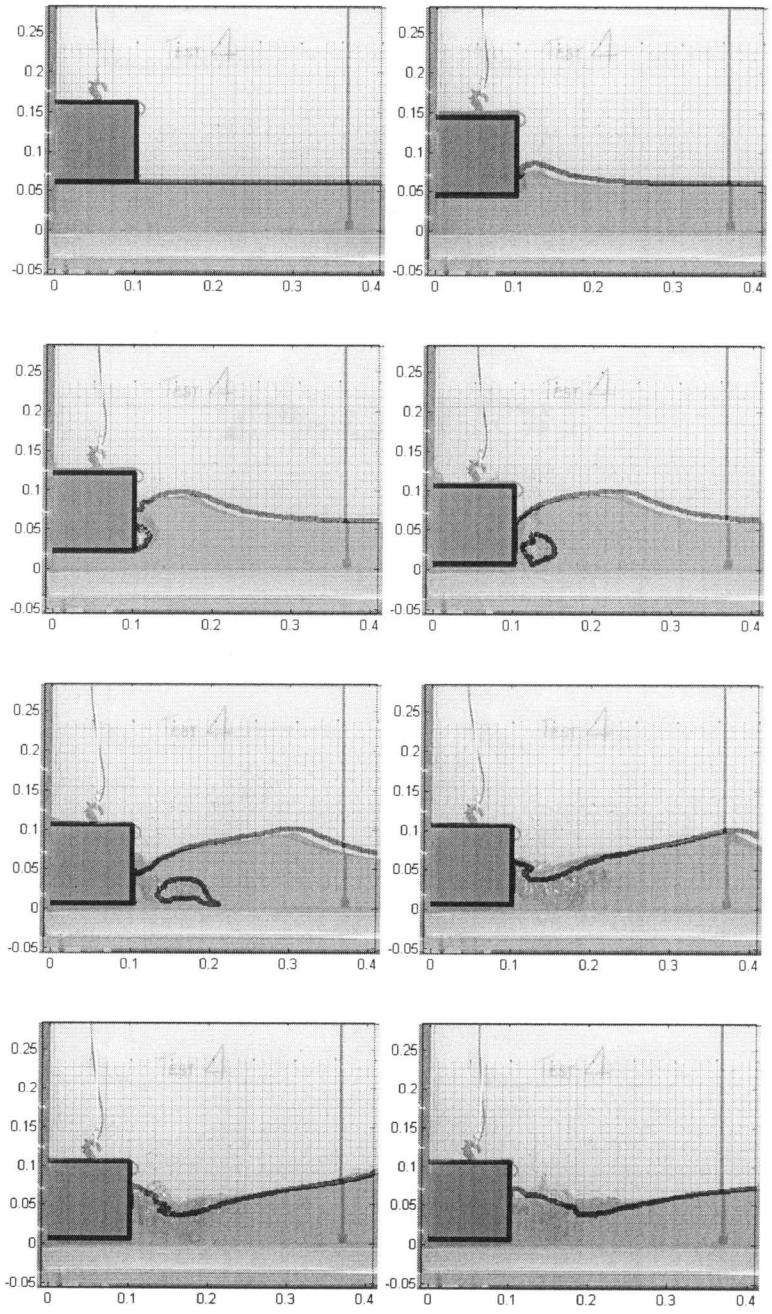

Fig 10. Snapshots of rigid body drop and wave generation, Test L10H6PM0

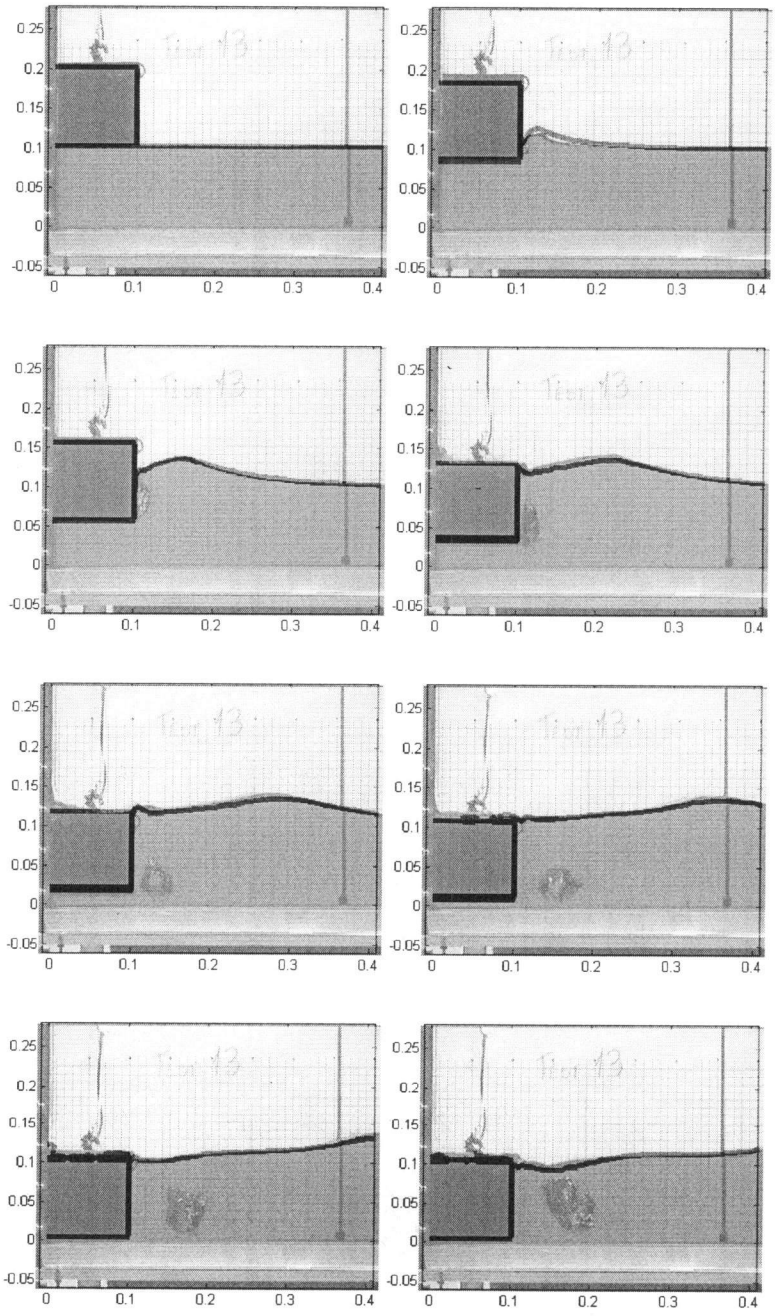

Fig 11. Snapshots of rigid body drop and wave generation, Test L10H10PM0

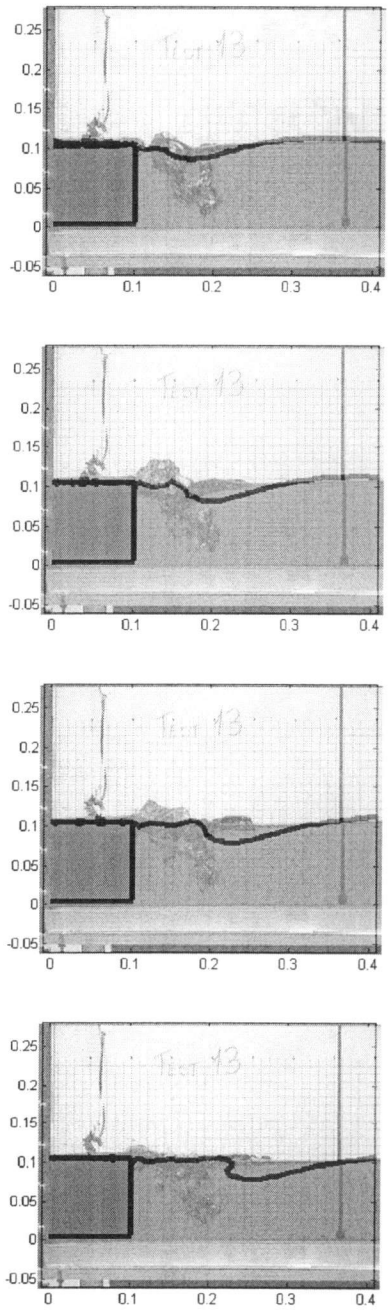

Fig 11. Snapshots of rigid body drop and wave generation, Test L10H10PM0 (continued)

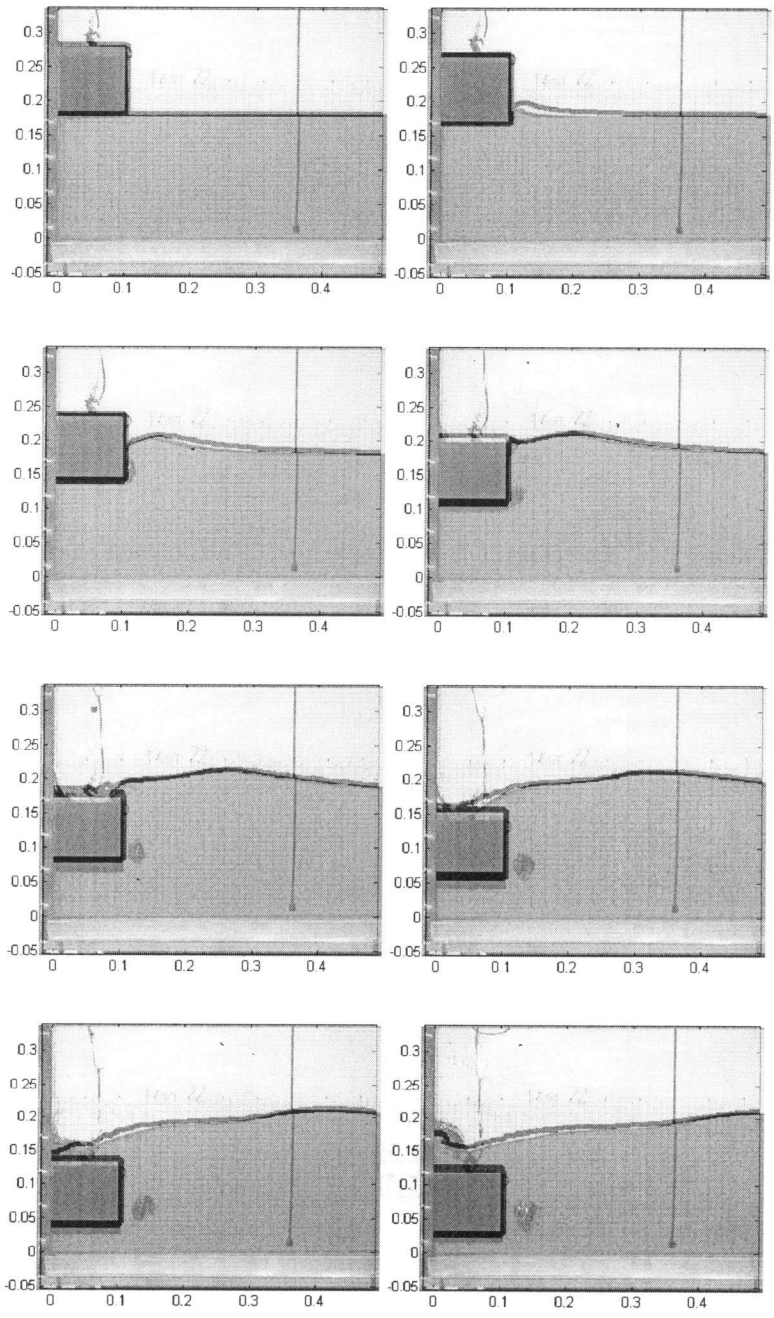

Fig 12. Snapshots of rigid body drop and wave generation, Test L10H18PM0

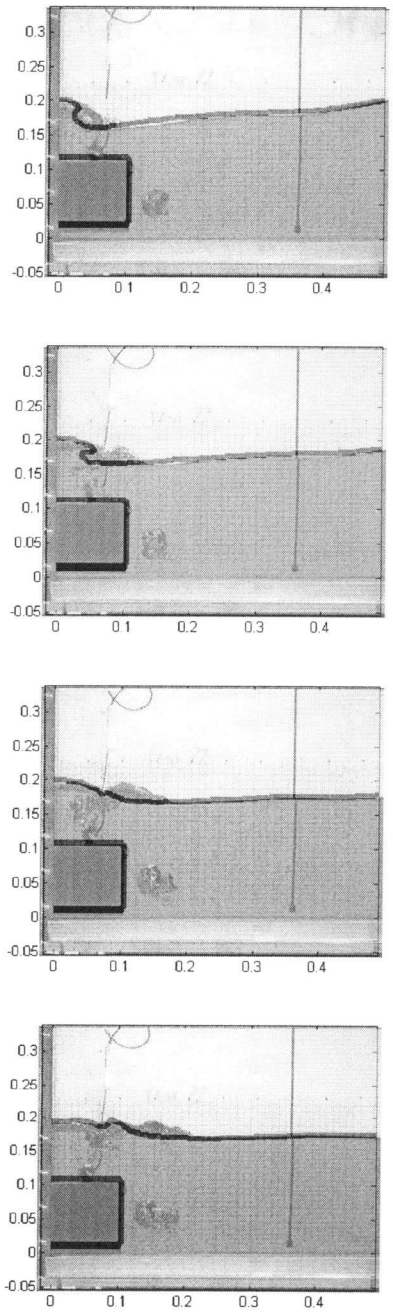

Fig 12. Snapshots of rigid body drop and wave generation, Test L10H18PM0 (continued)

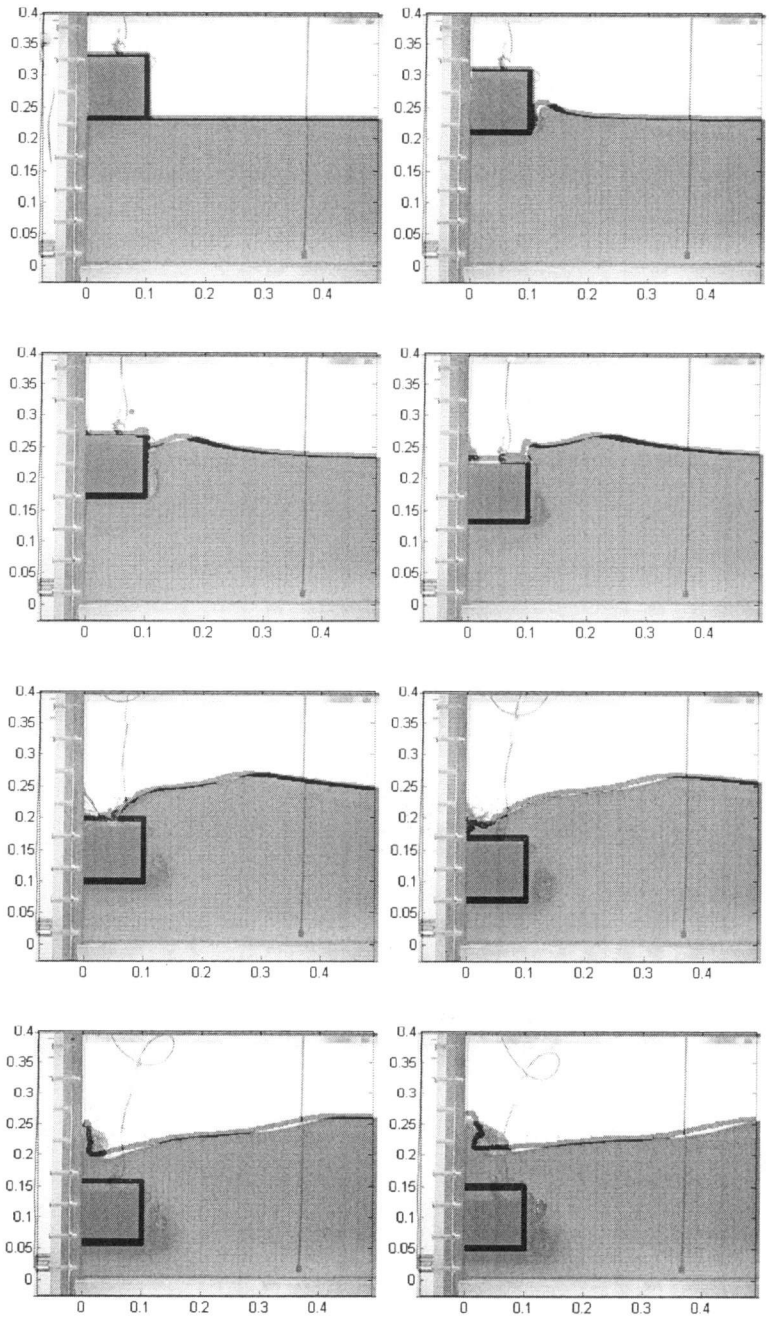

Fig 13. Snapshots of rigid body drop and wave generation, Test L10H23PM0

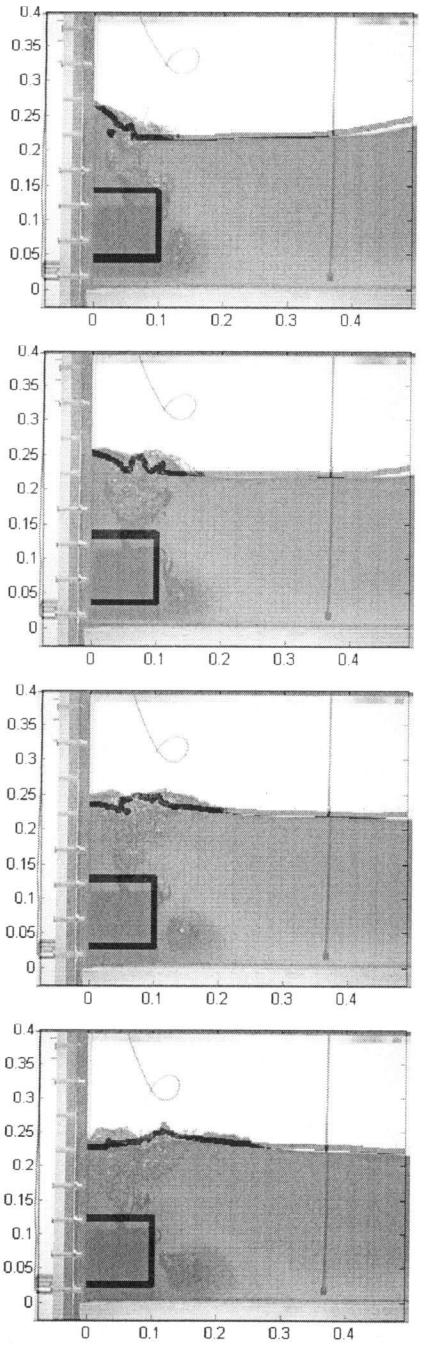

Fig 13. Snapshots of rigid body drop and wave generation, Test L10H23PM0 (continued)

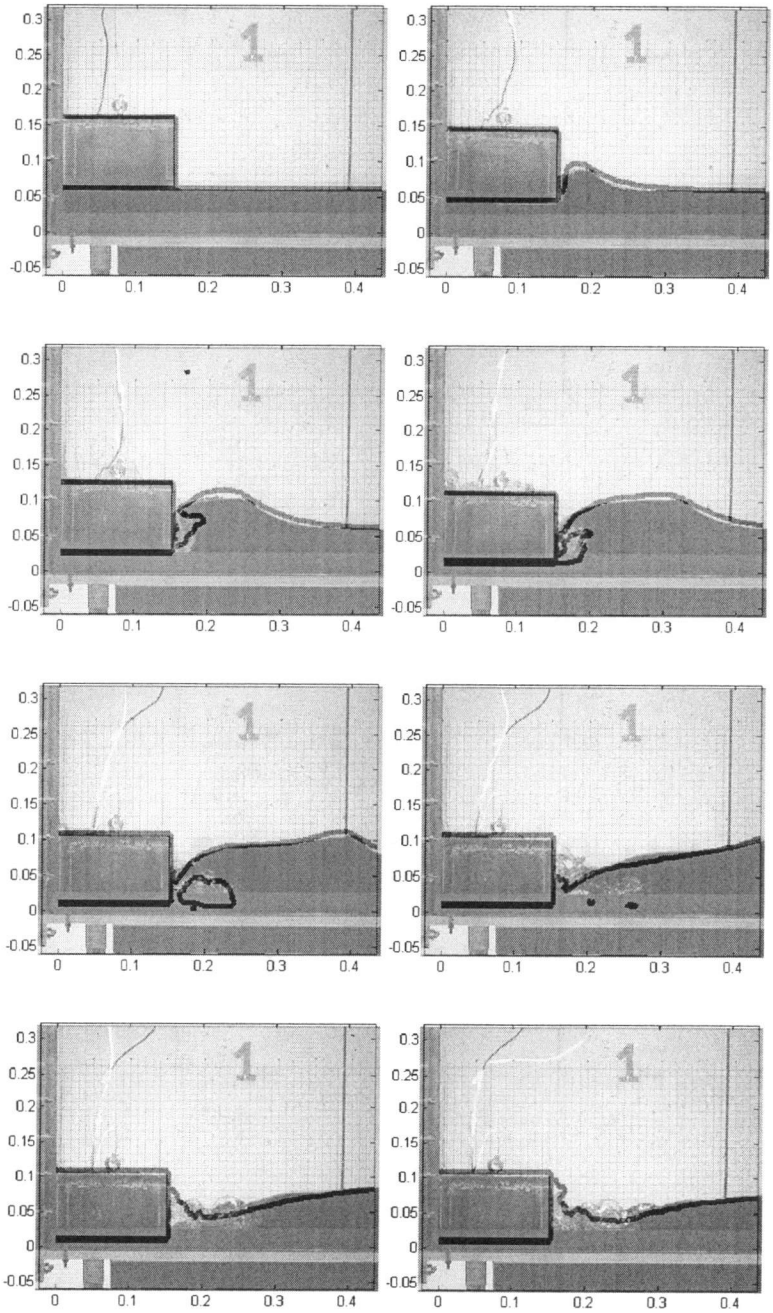

Fig 14. Snapshots of rigid body drop and wave generation, Test L15H6PM0

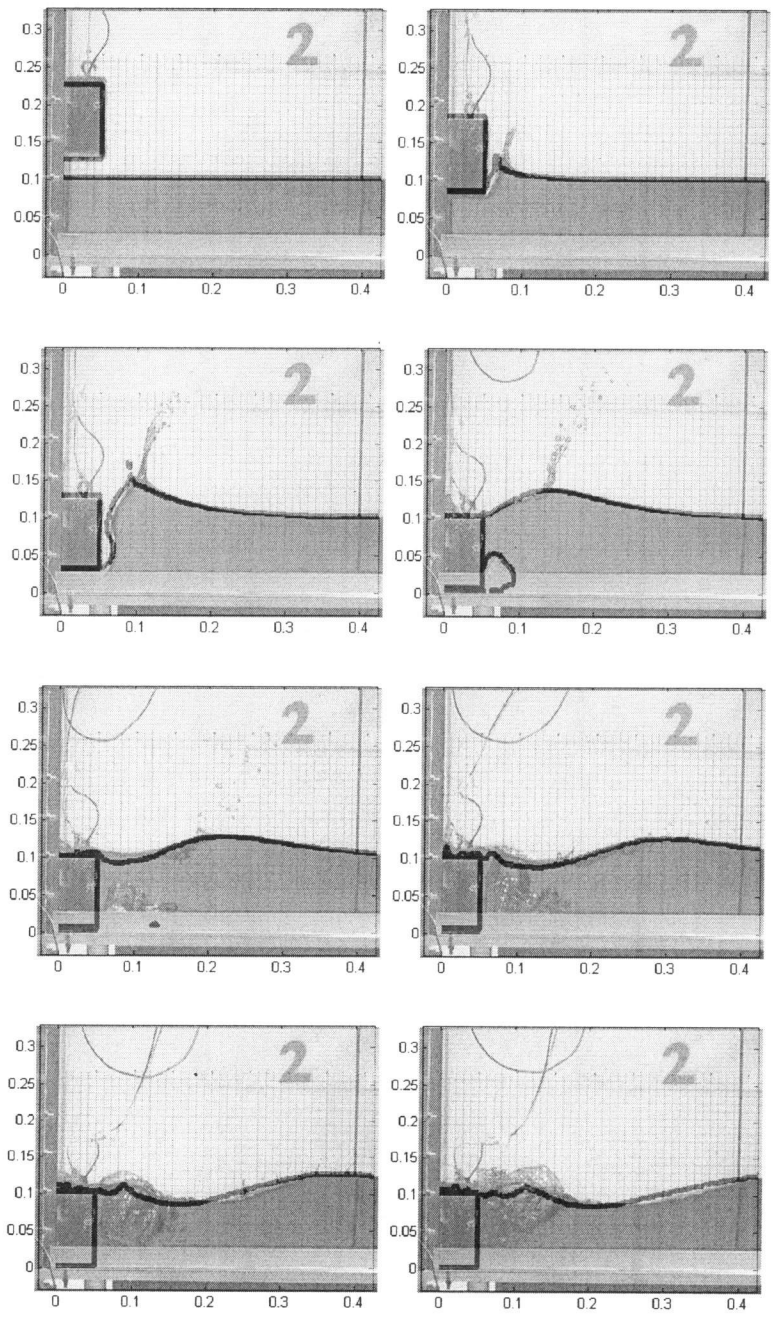

Fig 15. Snapshots of rigid body drop and wave generation, Test L5H10P3

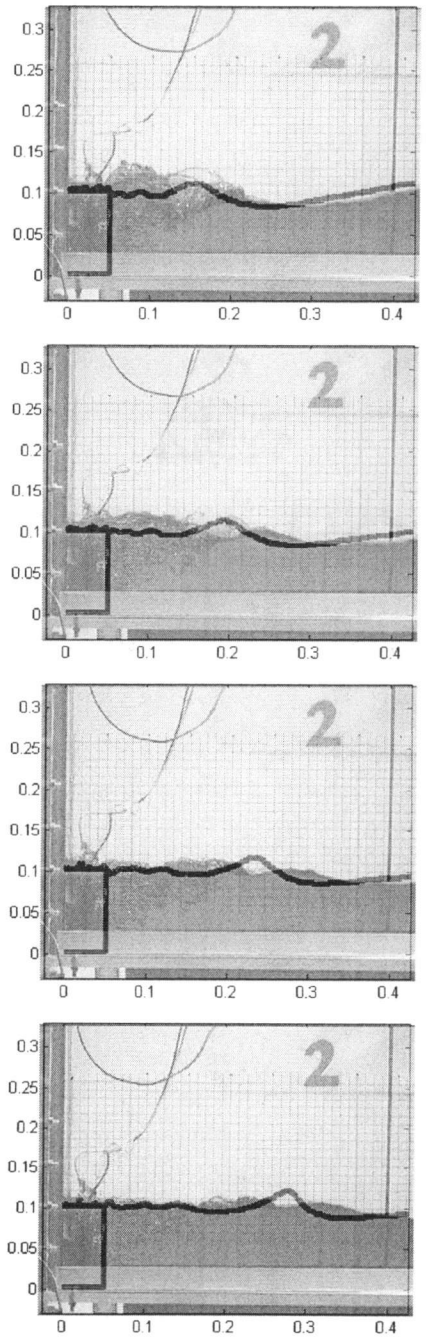

Fig 15. Snapshots of rigid body drop and wave generation, Test L5H10P3 (continued)

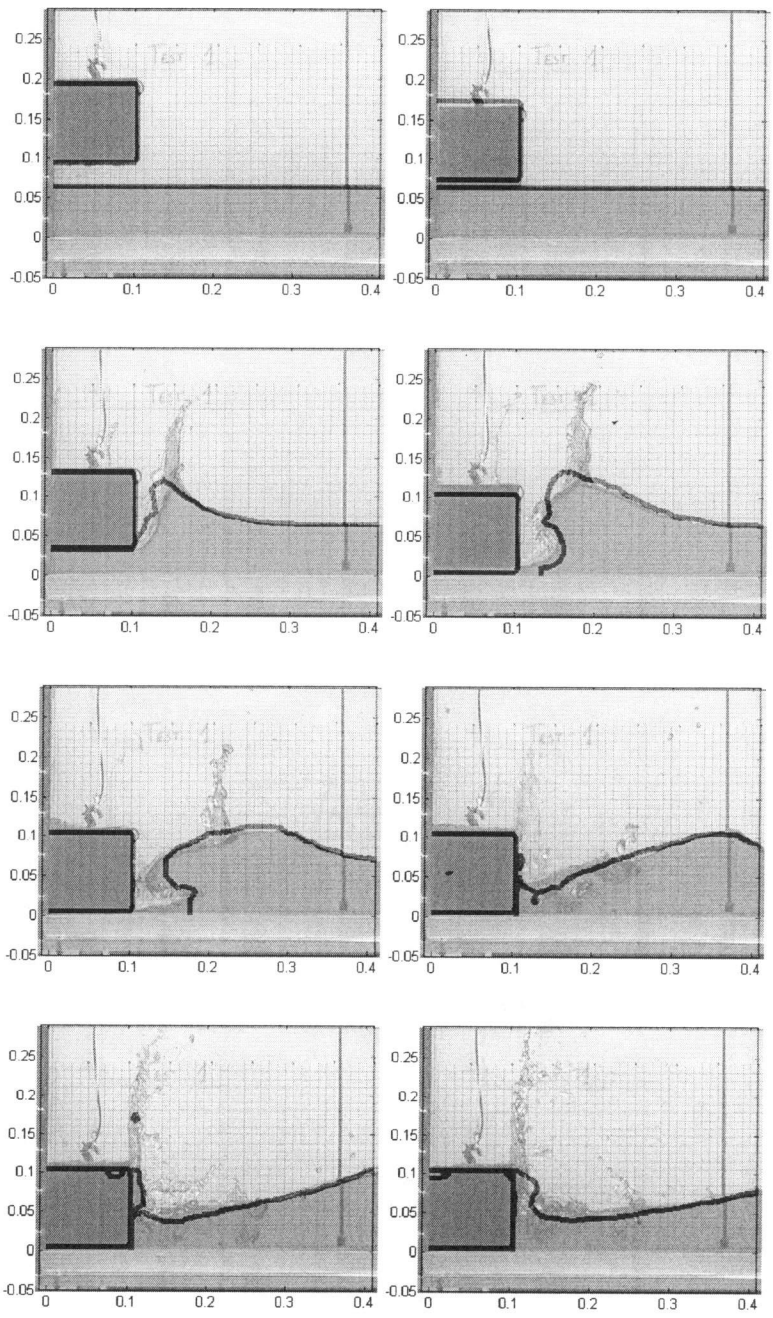

Fig 16. Snapshots of rigid body drop and wave generation, Test L10H6P3

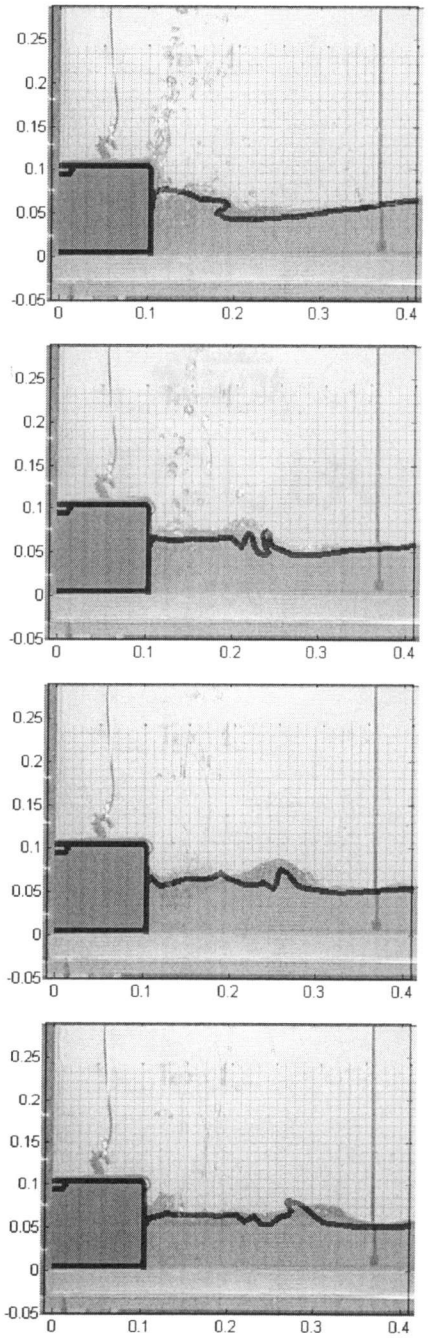

Fig 16. Snapshots of rigid body drop and wave generation, Test L10H6P3 (continued)

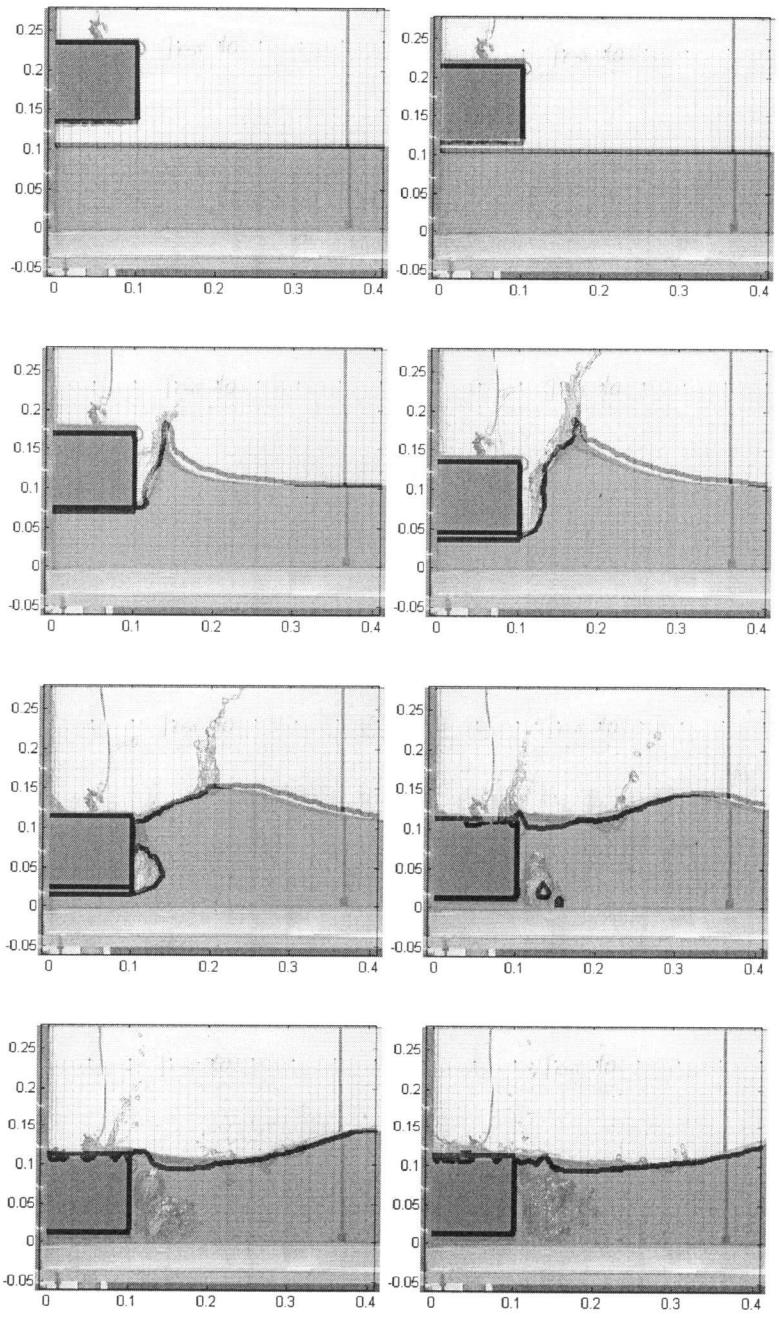

Fig 17. Snapshots of rigid body drop and wave generation, Test L10H10P3

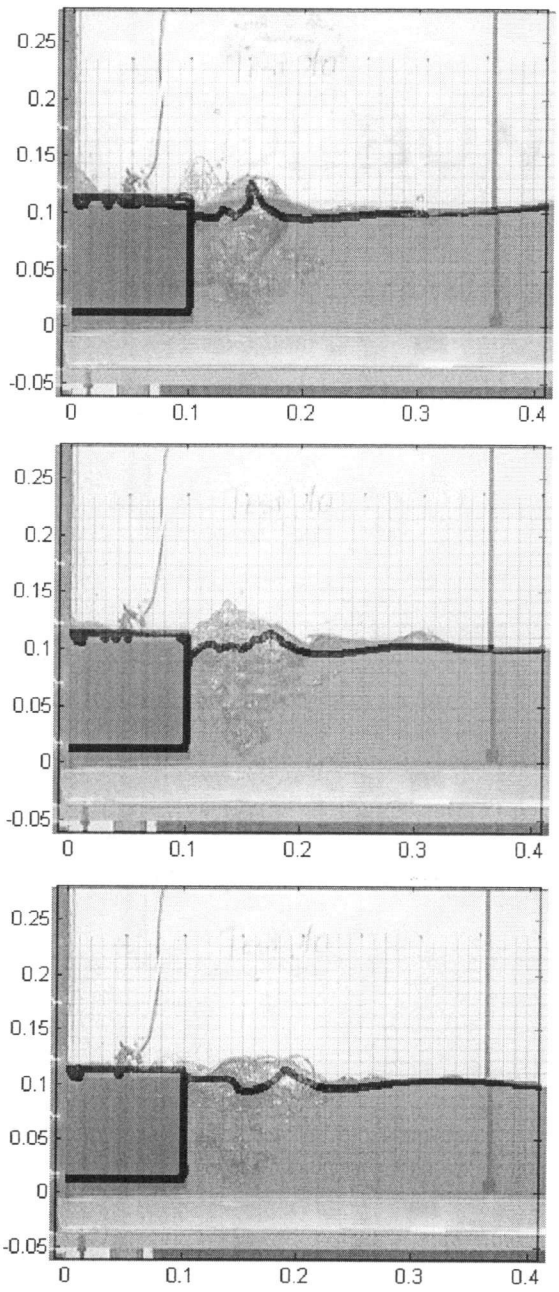

Fig 17. Snapshots of rigid body drop and wave generation, Test L10H10P3 (continued)

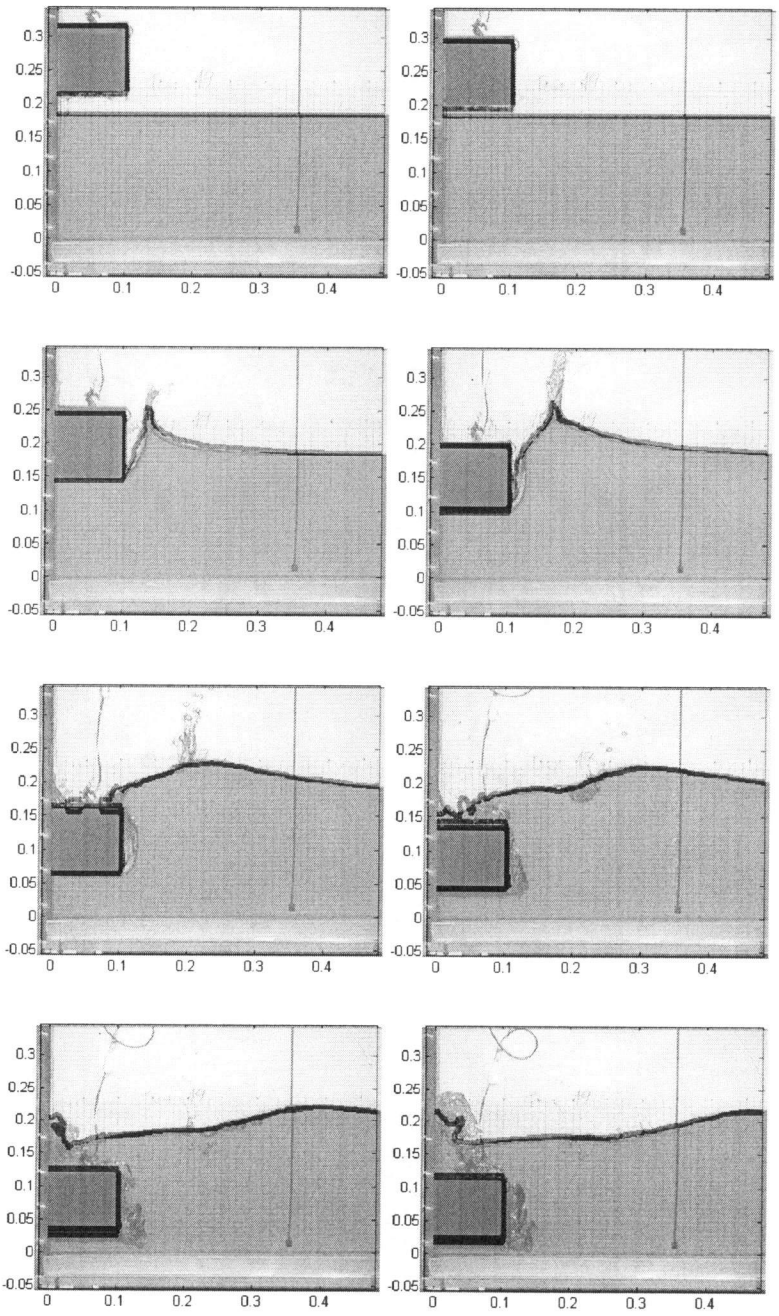

Fig 18. Snapshots of rigid body drop and wave generation, Test L10H18P3

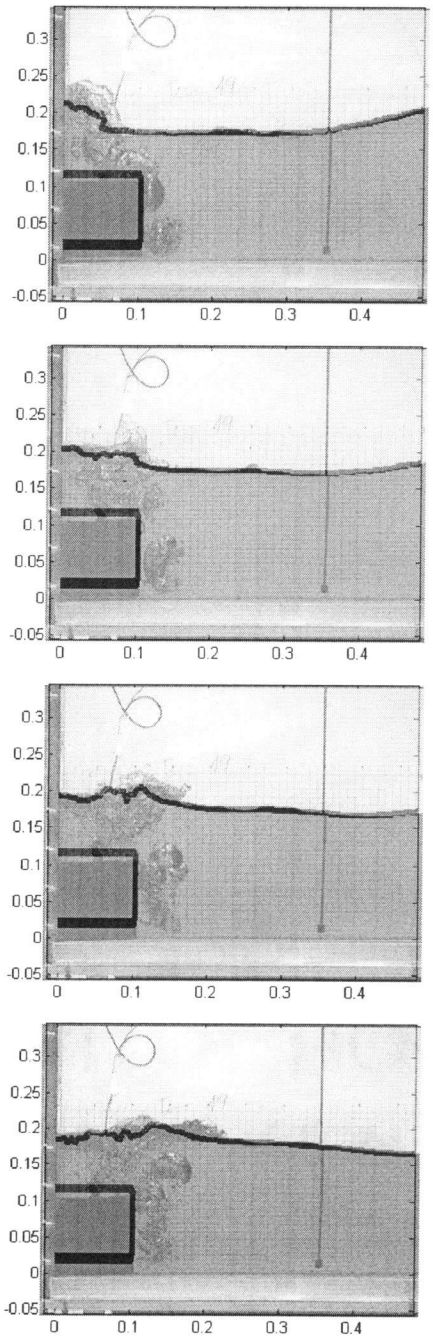

Fig 18. Snapshots of rigid body drop and wave generation, Test L10H18P3 (continued)

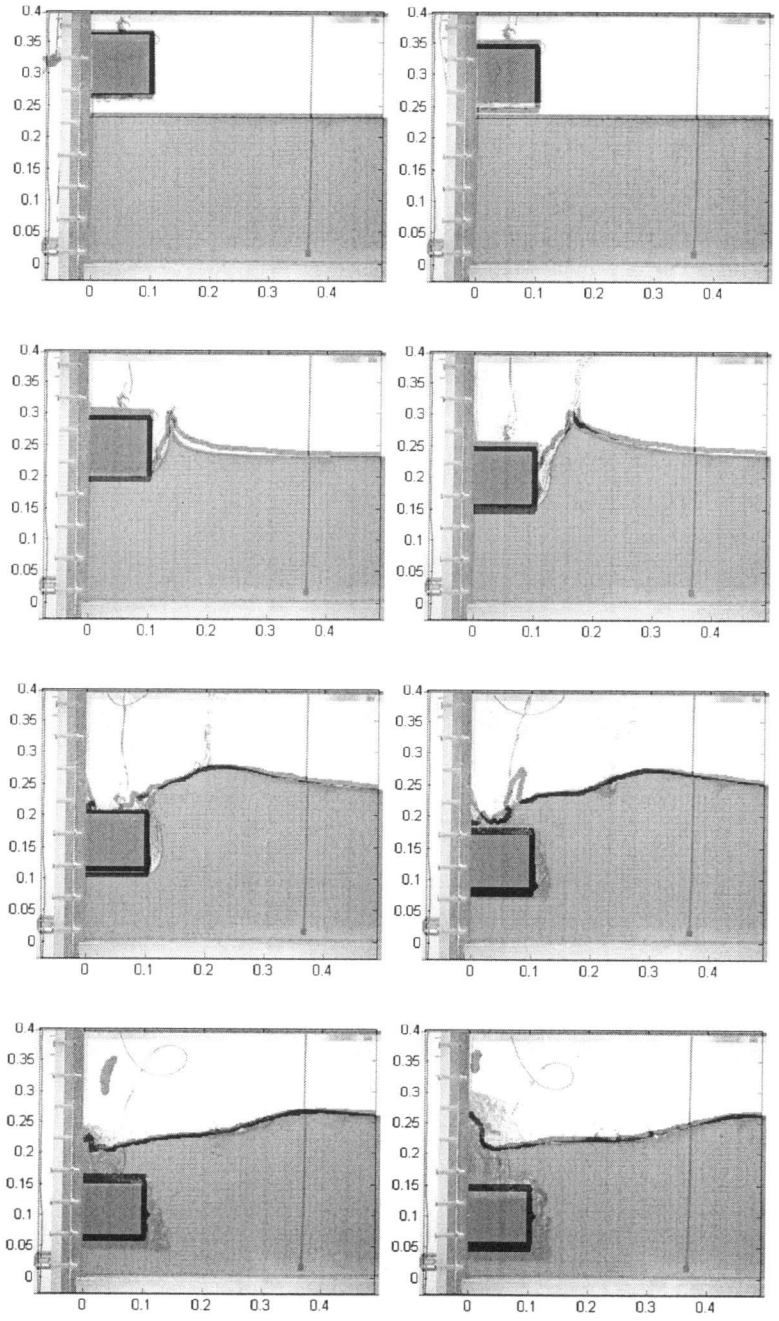

Fig 19. Snapshots of rigid body drop and wave generation, Test L10H23P3

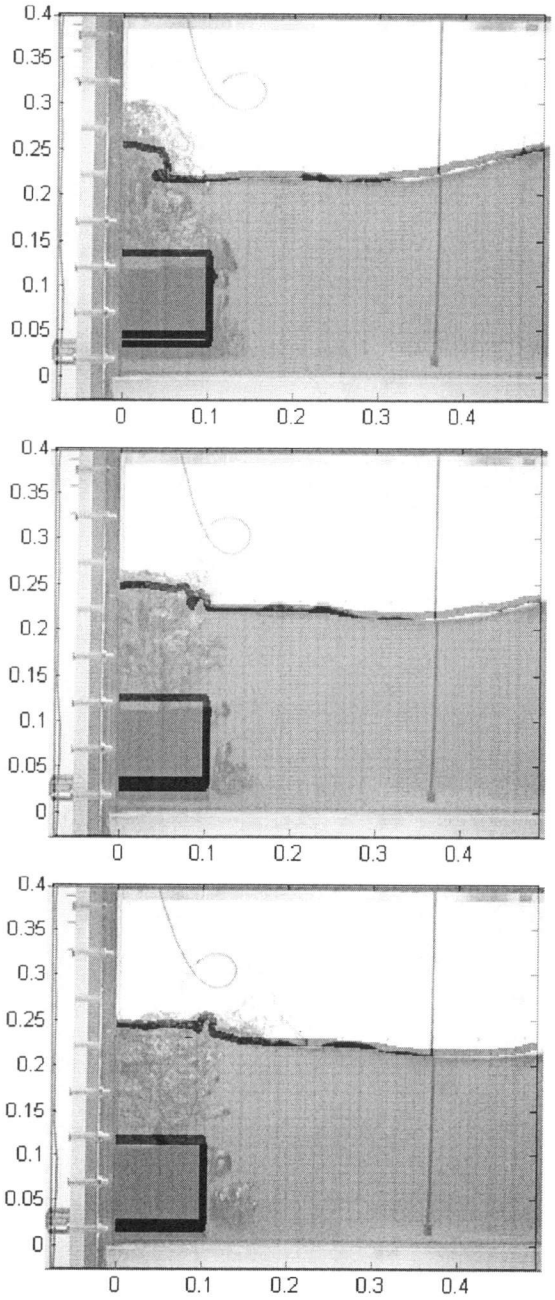

Fig 19. Snapshots of rigid body drop and wave generation, Test L10H23P3 (continued)

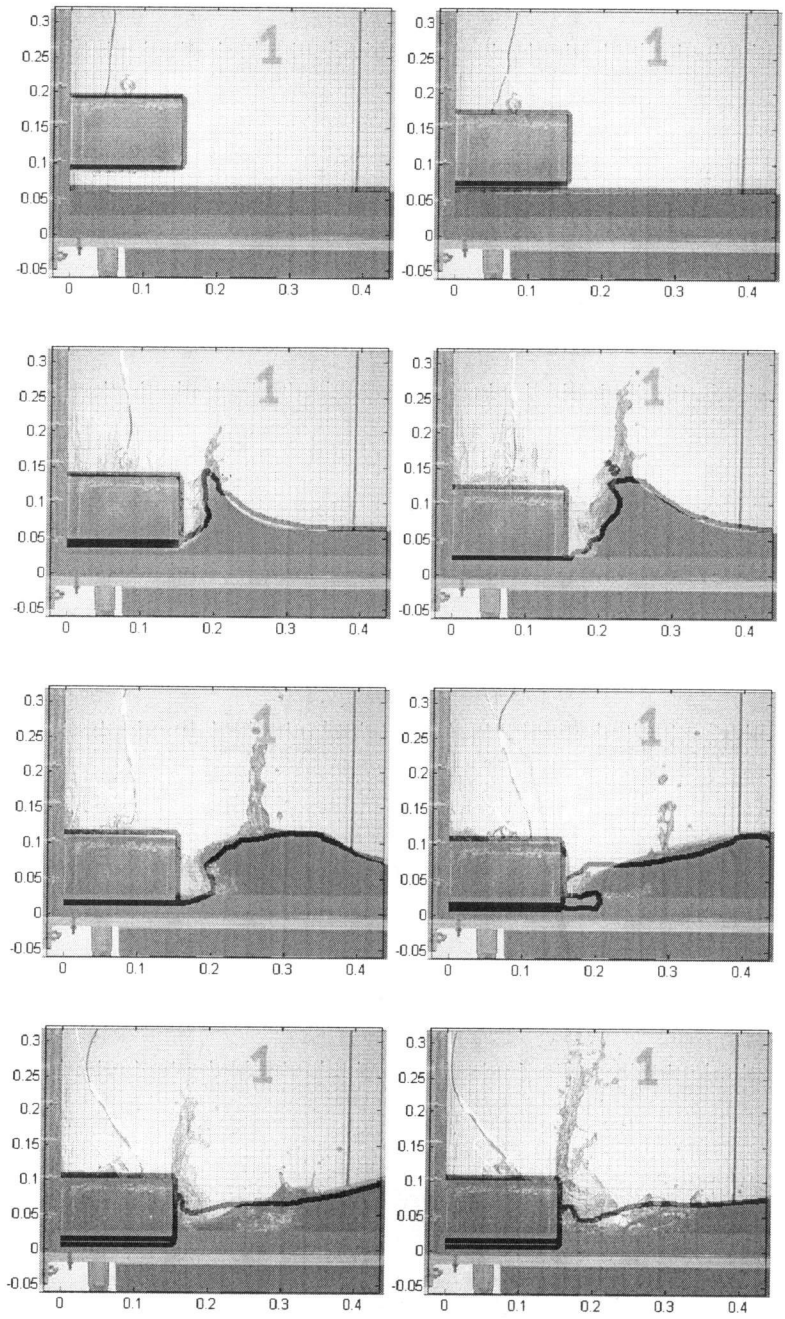

Fig 20. Snapshots of rigid body drop and wave generation, Test L15H6P3